POLITECNICO DI MILANO

School of Industrial and Information Engineering
Master of science in Materials Engineering and Nanotechnology

Electrical Transport Properties Investigation of Sp-Carbon Linear Atomic Chains-based Molecular Crystals

Supervisor:
Prof. Carlo S. Casari

Co-supervisors:
- **Prof. Mario Caironi**
- **Dr. Alberto Scaccabarozzi**
- **Dr. Sonia Peggiani**

Master Thesis of:
Mohamed T. Soliman
Mat. number: 874875

Academic Year: 2017 - 2018

بسم الله الرحمن الرحيم
إهداء الى والداي الأعزاء

Acknowledgment

Abstract

Carbon-based structures have grabbed much attention in the last decades. Moreover, they have been spread in many technological areas like nanoelectronics, high strength materials, laser technology and optical materials. Diamond and graphite are well known since ancient times as all carbon materials with a variety of applications. However, the missing third carbon allotrope is the one-dimension sp-carbon linear chain (carbyne), where, due to stability issues, its existence is questionable. Nonetheless, structures based on sp-carbon chains have been synthesized and investigated. While the theoretical work in the field of sp-carbon atomic chains is at advanced stages, many experimental investigations are not present yet. Sp-carbon atomic chains-based structures are very appealing due to their properties of tunability and the possibility that they can be integrated into different systems opening multiple windows for technological applications. One of the most interesting properties predicted for the chains is the electrical conductivity, very few works have been done in this area up to now due to the difficulty of the electrical characterization process of these systems. Indeed, the main motivation of this work is to investigate the electrical properties of sp-carbon chain-based molecules. In this work, four molecules were characterized and insightful information about their electrical properties was obtained. The characterization was done on the molecules in their crystalline form. The crystalline films of the molecules were obtained using drop casting and spin coating techniques and after, the electrical conductivity of these films was measured. Moreover, field effect transistors were successfully fabricated and tested using two of these molecules and data about the charge mobility of these molecules was revealed. Indeed, organic field effect transistors' field is a widely growing field, so it offers options for cheap and flexible electronics and it is an important tool for investigating the charge transport in organic semiconductors where their transport mechanisms are still ambiguous. Furthermore, Raman characterization of the molecules was done and it was used for stability checking. The vibrational properties of the molecules revealed by Raman helped in the interpretation of the results. Moreover, UV-Vis spectroscopy was used to investigate the electronic properties of the molecules which again helped in the interpretation of the results. Finally, optical microscope along with scanning electron microscope images were used for characterizing the formed crystals for a complete characterization picture. This work provides a new way of investigating the conduction properties of sp-carbon chains. It introduces a new class of materials to the family of organic semiconductors which shall help in a better understanding of their transport mechanisms. Finally, it opens a new area for improving the field of field effect transistors.

Sommario

Le strutture a base di carbonio hanno attirato molta attenzione negli ultimi decenni. Infatti, si sono diffuse in molte aree tecnologiche come la nanoelettronica, i materiali ad alta resistenza, la tecnologia laser e i materiali per ottica. Diamante e grafite sono noti fin dall'antichità come materiali composti totalmente di carbonio con una varietà di applicazioni. Tuttavia, la terza forma allotropica mancante del carbonio è la catena lineare carbonio-sp a una dimensione (carbyne), per cui, a causa di problemi di stabilità, la sua esistenza rimane in qualche modo discutibile. Nonostante ciò, le strutture basate su catene di carbonio-sp sono state sintetizzate e investigate. Mentre il lavoro teorico sul campo delle catene atomiche carbonio-sp è in fase avanzata, non sono invece presenti numerevoli indagini sperimentali. Le strutture basate su catene atomiche carbonio-sp sono molto allettanti grazie alla loro flessibilità sulle proprietà e alla loro possibilità di essere integrate con diversi sistemi aprendo ulteriori vie per applicazioni tecnologiche. Una delle proprietà più interessanti previste per le catene carbonio-sp è la conduttività elettrica, ma in questa area sono stati eseguiti pochissimi lavori finora a causa della difficoltà del processo di caratterizzazione elettrica di questi sistemi. Difatti, la motivazione principale di questo lavoro è l'indagine delle proprietà elettriche delle catene di carbonio-sp. In questo lavoro, sono state caratterizzate quattro diverse molecole da cui sono state ottenute informazioni importanti sulle loro proprietà elettriche. La caratterizzazione è stata effettuata sulle molecole nella loro forma cristallina. I film cristallini delle molecole sono stati ottenuti utilizzando tecniche di "drop casting" e "spin coating" e successivamente la conducibilità elettrica di questi film è stata misurata. Inoltre, transistor a effetto di campo sono stati fabbricati e testati con successo, utilizzando due di queste molecule, da cui sono state rivelate informazioni sulla mobilità di carica di queste molecole. Infatti, il campo dei transistor organici ad effetto di campo è un settore in grande espansione in quanto offre possibilità di una elettronica economica e flessibile ed è uno strumento importante per lo studio del trasporto di carica nei semiconduttori organici dove i loro meccanismi di trasporto sono ancora ambigui. Inoltre, la spettroscopia Raman delle molecole è stata eseguita per valutare la stabilità. Le proprietà vibrazionali delle molecole rivelate da Raman hanno aiutato nell'interpretazione dei risultati. Inoltre, la spettroscopia UV-Vis è stata utilizzata per studiare le proprietà elettroniche delle molecole che hanno anche'esse aiutato nell'interpretazione dei risultati. Infine, il microscopio ottico insieme alle immagini del microscopio elettronico a scansione sono stati utilizzati per caratterizzare i cristalli formati per avere un quadro complete di caratterizzazione. Questo lavoro fornisce un nuovo modo di studiare le proprietà di conduzione delle catene di carbonio sp. Introduce una nuova classe di materiali alla famiglia dei semiconduttori organici che contribuirà ad una migliore comprensione dei loro meccanismi di trasporto. Infine, apre una nuova area per il miglioramento nel campo dei transistor a effetto di campo.

Table of Contents

Introduction

Since the industrial revolution in the 20th century, the acceleration of the technological applications demanded a similar acceleration in material science in order to keep up with the exponentially growing need for new material properties. Nonetheless, carbon-based materials have offered solutions to many technological problems in the last century. Since 1959 when Richard Feynman gave his historical talk "there's plenty of room at the bottom" carbon nanostructures have been taking milestone steps in the field of nanoscience and technology. From fullerenes to carbon nanotubes to graphene and the research in the area of carbon nanomaterials has been vastly growing. The ability of the carbon atom to hybridize in different forms is the main reason for the wide range of properties that carbon structures possess. Diamond and graphite have been known since ancient times as all carbon structures. However, the existence of the missing third allotrope, one-dimension sp-carbon atomic chain (carbyne), was questionable.

Carbyne is the ultimate one-dimensional carbon structure with a chain of carbon atoms in sp hybridization form. The bonds between the atoms in the chain determine the type of the chain. Two possible types of carbyne can be formed, cumulene and polyyne. Cumulene is a chain of carbon atoms connected with a sequence of equal double bonds while polyyne is a chain connected with a sequence of alternation of single and triple bonds. Cumulene is predicted to be metallic while polyyne to be a semiconductor but the infinite chain was never realized. Nonetheless, finite chains were synthesized and characterized using various techniques where they offer an interesting properties tunability feature which makes them appealing systems for technological applications and basic science.

One of the most appealing properties which are predicted for the chains is their electrical conductivity, for which it was predicted that up to two quanta of conductance could be achieved with a single chain. However, the experimental work in this area is far behind, in fact only a few groups were able to report conductivity measurements for the chains. Nonetheless, the reported values were far from the theoretically predicted ones where the reason behind that is still ambiguous. The reason for the low number of experimental works with respect to the theoretical work in this area is the difficulty of performing electrical transport experiments on these systems. Stability of the chains is the main drawback in this area as it makes it difficult to prepare systems with controlled dimensions and to assure that there will be no structural change during the measurements. Trying to close the gap between the theoretical and experimental work by providing new ways for experimentally investigating the electrical transport properties of these materials is the main motivation for this work. Specifically, four similar molecules based on sp-carbon chains were investigated in terms of their electrical conductivity in order to have a deeper understanding of the electrical transport in these systems where a comparative study can be made.

In details the main objectives of this work were: i) to measure the electrical conductivity of the four molecular crystals; ii) test the molecular crystals as a transistor active medium in field effect transistor configuration; iii) perform a comparative study between the four molecules to relate the difference in performance to the difference in structure; iv) check the stability of the molecules during the measurement process.

The setup used for the electrical characterization was the deposition of the molecules on the Fraunhofer substrate which is a pre-purchased substrate explicitly designed for electrical characterization of organic field effect transistors. The deposition was done using two main techniques, spin coating and drop casting. The deposited film was characterized using image analysis of optical microscope and scanning electron microscope images. The stability check of the deposited films was done using Raman spectroscopy before and after the measurements. Moreover, UV-Vis spectroscopy was used to obtain information about the electronic properties of the molecules which is important for results interpretation. The using of the molecules as a field effect transistor active medium was to serve more than one purpose. First, the field effect transistor's measurements are a powerful tool for studying charge mobility in semiconductors. Moreover, sp-carbon

chains-based systems where never used in this area before, especially the cumulenic type structures. Finally, the organic field effect transistors field is a rapidly growing field as it offers new opportunities for technology, where cheap and flexible electronics can be manufactured and for low voltage operating devices. Indeed, invading this field with a new class of materials was an appealing idea that is believed to open a new window for improvement as well as it provides an excellent opportunity for a better understanding of the transport mechanisms in sp-carbon chains-based materials specifically and organic semiconductors generally.

The molecules which were characterized in this work are 1,2-diphenylacetylene (DPA) and 1,4-diphenylbutadiyne (DPB), which are polyynic type molecules and PH3 and PH5 which are cumulenic type molecules. The cumulenic type molecules were dissolved in dichloromethane solvent while the polyynic type molecules where dissolved in hexane solvent.

The structure of this thesis is summarized in the following.

Chapter 1: A general introduction to sp-carbon and the carbon atom chains is provided. First, their structure and predicted properties are discussed. Then, the difficulties in the field of sp-carbon chains concerning synthesis and stability issues of these systems are highlighted where different solutions techniques are reported. Finally, theoretical studies and experimental results involving sp-carbon linear structures in different applications are discussed with a focus on works related to electrical conductivity.

Chapter 2: Transport properties in organic semiconductors are discussed starting with the electronic properties of organics then the physics behind electrical transport and charge carriers' behaviors in semiconductors were reviewed finally the general features of the organic field effect transistors were explained.

Chapter 3: Substrates properties and molecular systems are introduced. Then the preparation techniques and the tools used are discussed.

Chapter 4: Results obtained in this work are deeply analyzed and compared.

Chapter 5: Conclusions and future perspectives

1 Sp-carbon atomic wires

In the last three decades, carbon and its nanostructures have been playing an exponentially growing role in both science and technology. The discovery of fullerenes to nanotubes to graphene derived Andreas Hirsch in 2010 to call this period "the era of carbon allotropes" [1]. Out of all carbon allotropes, we can consider sp-carbon linear ideal chain (Carbyne) as the missing allotrope. It is the most elusive, and the stability is on edge. However, it held a special interest in the past and still are in the present. Current achievements, however, open multiple windows for interesting scientific and technological applications in the future.
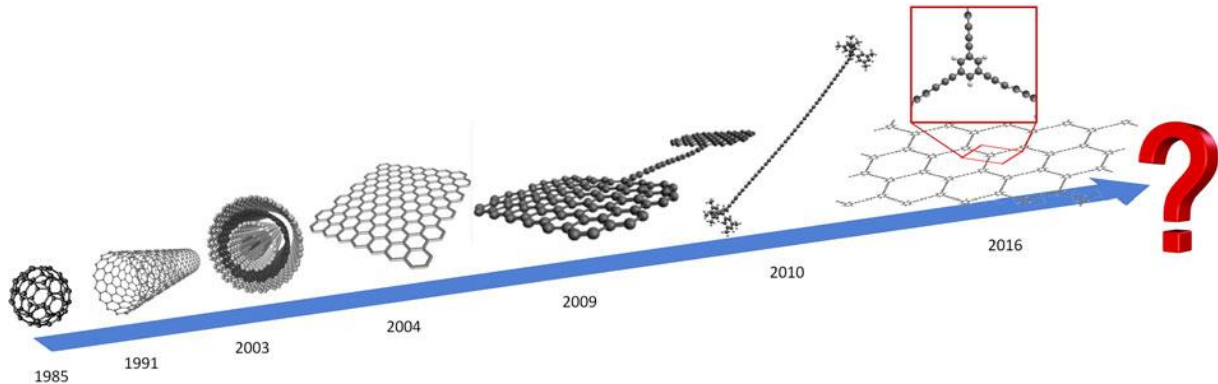
Fig. 1.1 Carbon nanostructures' evolution showing the growing importance of carbon for nanotechnology in the last three decades [2].

1.1 Hybridization and the missing sp-carbon based allotrope

Carbon is one of the essential elements in nature. Thanks to the variety of forms and the wide range of properties its structures possess, scientists and engineers have been using carbon structures in all kinds of applications and technologies. This importance is thanks to the possibility of the carbon atom to hybridize in three different forms. Giving rise to a wide variety of structures with different properties when moving from one form of hybridization to another and when mixing more than one form of hybridization.

Isolated carbon atom before hybridization has a total of six electrons. Two electrons are in 1s core orbital, and they are not included in the hybridization prosses or in the chemical reactions in general. Four electrons are in the outer shell divided into two subshells. The first subshell only includes the 2s orbital which contains two electrons. The second subshell includes three degenerate orbitals, $2p_x$, $2p_y$, and $2p_z$. Only one 2p orbital is fully occupied with two electrons. However, it is energetically favorable for the electrons, first, to occupy different orbitals which decrease the Coulombic repulsion between electrons as they have the same charge, second, to possess the same spin direction to decrease their exchange interaction energy. Because of that, carbon atom's outer two sub-shells (2s, 2p) tend to hybridize together giving rise to what so-called sp orbitals. Since the 2p sub-shell is composed of three degenerate orbitals, this hybridization can occur in three different ways sp^3, sp^2, and sp.

1.1.1 Sp^3 and sp^2- hybridization

When all the three 2p orbitals together with the 2s orbital hybridize, they give rise to four degenerate sp^3 hybrid orbitals. The four orbitals distribution in space which achieves the minimum energy for them gives rise to tetrahedral distribution with the four orbitals equally spaced in the three dimensions as in Fig. 1.2. With one electron per orbital, the four sp^3 orbitals form four covalent bonds in total. The bonds which are formed out of the hybridized orbitals are called sigma bonds. The carbon allotrope composed of all sp^3 hybridized carbon atoms is diamond. Diamond is an insulator highly crystalline solid. It can be found rarely in nature due to the need for high temperature and pressure for its formation. However, it possesses many different appealing properties, like its high value for jewelry and its exceptional hardness. Recently research is going on

transforming diamond from insulator to semiconductor (through doping), in order to use it in high demanding electronics.

When two out of the three 2p orbitals hybridize together with the 2s orbital, they give rise to three degenerate sp^2 orbitals. The three hybridized orbitals achieve their minimum energy by distributing in a trigonal planar geometry as in Fig. 1.2. The three hybridized orbitals form three covalent sigma bonds and the third 2p unhybridized orbital with slightly higher energy form one π-bond. The carbon allotrope composed of all sp^2 hybridized carbon atoms is graphite. Graphite is a 3D solid composed out of 2D layers stacking on top of each other. The 2D layers are composed of carbon atoms covalently bonded together. Each carbon atom is connected to three carbon atoms forming a 2D network of honey-comb shape. These 2D layers are connected through π-stacking. Graphite is a conductor thanks to the highly delocalized π-electrons. In 2004 Geim and Novoselov successfully separated as single layer out of graphite. This work was one of the most significant achievements in the modern science era. In fact, in 2010 Geim and Novoselov received Nobel prize in physics for their work on graphene. They were able to exfoliate one atomic layer which is the ultimate 2D allotrope of carbon (graphene). Graphene possesses a set of peculiar properties indeed. Being the ultimate 2D material, started a big debate since and before graphene, 2D crystals argued to be impossible to exist due to stability problems and graphene existence put this argue under investigation. From the electronic point of view, graphene has a unique band structure with the famous Dirac cone (the electrons dispersion relation at certain points in the reciprocal space is linear at the Fermi level, which results in massless electrons at those points).

Before graphene, in 1985 Kroto et al. discovered the buckminsterfullerene C_{60} which is a structure consisting of hexagons and pentagons, a mixture of sp^2 and sp^3 carbon [3]. Six years later there was the discovery of the single wall carbon nanotube (SWCNT). Then the multi-wall carbon nanotube (MWCNT) discovery followed. Work is still active in searching for novel carbon structures based on different hybridization states.
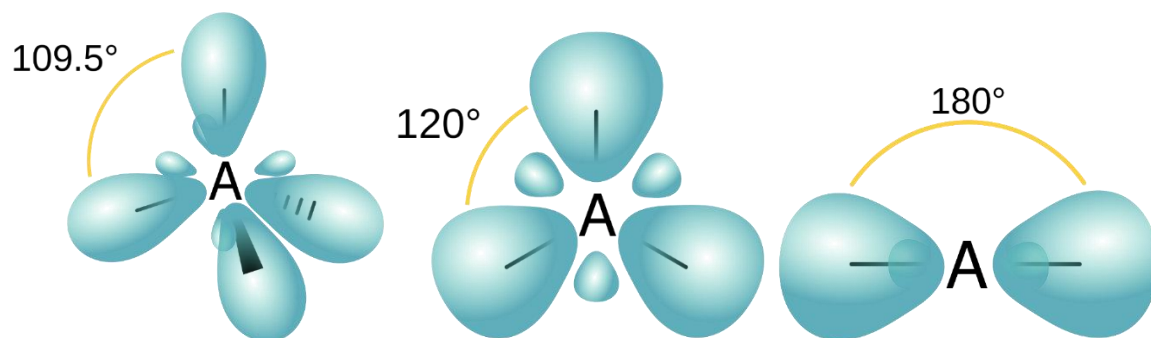
Fig. 1.2 sp hybridized orbitals for the three forms of hybridization. sp3 (left), sp2 (middle), and sp (right)

1.1.2   Sp - hybridization

When only one out of the three 2p orbitals hybridizes with the 2s orbital, they give rise to two degenerate sp orbitals. Again, the minimum energy is achieved when the hybridized orbitals possess the geometry which separates them as far as possible. In this case, the hybridized orbitals take the linear geometry, giving rise to linear structures. While the hybridized sp orbitals occupied with one electron each result in two covalent sigma bonds one on each side of the carbon atom, the remaining two 2p orbitals which are as well occupied with one electron each, form two π-bonds. The two π-bonds can be on one side of the carbon atom like in the case of the HCN molecule (H-C≡N). They also can be one on each side like in the case of CO_2 (O=C=O).
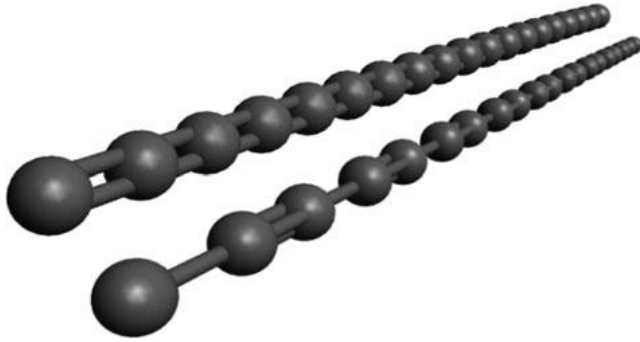
Fig. 1.3 Carbyne with its two configurations. cumulene (top left), and polyyne (bottom right).

The carbon allotrope out of all sp hybridized carbon is Carbyne. Carbyne is the ultimate 1D carbon structure. It is an infinite sequence of carbon atoms forming a one-dimensional chain. The bonds between the carbon atoms define the type of the chain. A sequence of double bonds between carbon atoms results in an equally spaced array of carbon atoms forming the chain, and in this case, the chain is called cumulene (=C=C=C=C=C=)(Fig. 1.3). An alternation of a single-triple sequence of bonds results in an array of carbon atoms in which there is an alternation in the bond length between them. In this case, the chain is called polyyne (-C≡C-C≡C-C≡C-C≡C-). The bond length alternation (BLA) is what defines the type of the chain. If it is zero, then the chain is cumulene, and if it is different from zero, then the chain is polyyne. The single CC bond length is around 1.5 A in diamond, while the triple bond length is around 1.2 A in HCN. However, in the case of polyyne, the single CC bond is slightly shorter than normal, while the triple bond is slightly longer. This is due to the tendency of the π-electrons to delocalize, resulting in adding extra bonding character to the single bond while decreasing the bonding character of the triple bond. This delocalization of the π-electrons makes the chains highly reactive. The chain reactivity increases by increasing the chain length due to the increase in the π-conjugation. This high reactivity leads to the chains to cross-link, and the carbon atoms relax to a more stable form of hybridization when the chains come close or interact with the environment. This issue of instability was the main argument against the existence of carbyne.

1.2   Infinite sp-carbon chains

Despite the doubt against the existence of carbyne, scientists have been developing models studying its properties. This is in fact, due to its appealing predicted properties and its outstanding characteristics. Starting from the effective surface of the wires it was predicted to be more than 13,000 m^2/g [4]which is at least four times more than the value predicted for graphene. Another valuable property is the stiffness which the sp carbon atomic wires were predicted to be the champion out of all other forms of materials, with the highest Young modulus up to 32 TPa and specific stiffness around 10^9 Nm/Kg [5]. Thanks to the high phonon frequencies and the long mean free path of the phonons leading to ballistic thermal transport reaching the micron scale, sp carbon atomic wires indeed predicted to have significantly large thermal conductivity values. These values are ranging from 80 to 200 KW/mK at room temperature, which is again much higher than their cousins' graphene and carbon nanotubes [6].

1.2.1   Electronic properties

The Carbyne electronic properties can be revealed studying this simple solid-state model. Cumulene is a one-dimensional crystal with one atom per unit cell. While polyyne is a one-dimensional crystal but with two atoms per unit cell. Analyzing the two configurations, cumulene appears to be metallic with a half-filled valence band with one electron for each 2p orbital. On the other hand, in the case of polyyne, a case of two sublattices results in two electrons for each 2p orbital, and a fully occupied valence band leading to a semiconductor behavior.
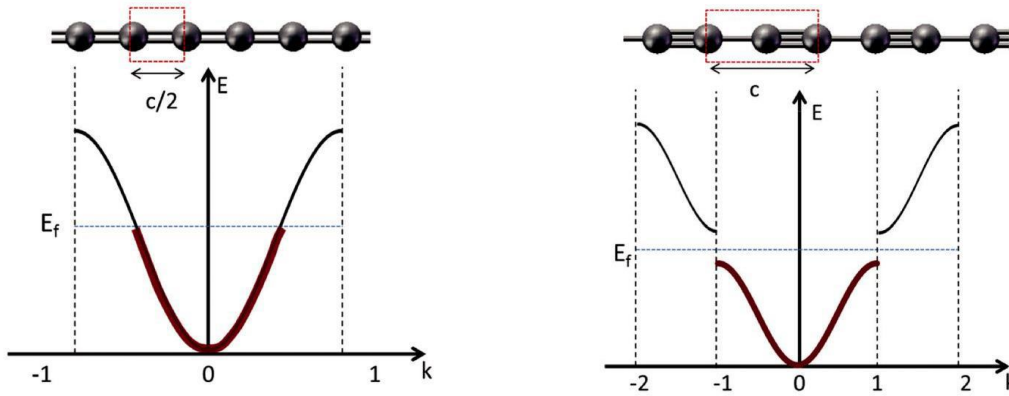
Fig. 1.4 The one-dimensional unit cell for cumulene (left) and polyyne (right). the dotted red rectangle represents the unit cell in real space, while the graph represents the unit cell of the one-dimension block band in the reciprocal space showing the energy dispersion relation and the Fermi level [7]

From Fig. 1.4 we can notice that in the case of cumulene, the Fermi energy is at half of the valence band which makes the system metallic. While in the case of polyyne the Fermi energy is in the energy gap that has been opened when the Fermi surface touched the edges of the Brillouin zone, which makes the system a semiconductor/insulator.

One-dimension systems are susceptible to what is called Peierls distortion. Peierls theorem states that "a one-dimensional equally spaced chain with one electron per ion is unstable". Thus, cumulene configuration is expected to be subjected to the Peierls distortion and pass to polyyne configuration.

As shown in Fig. 1.5, quantum calculations for the energy surface as a function of the BLA in the infinite chain shows two equivalent minima, corresponding to two stable polyynic configurations, and a local maximum exactly at BLA equal to zero, corresponding to the cumulenic configuration, which is in agreement with Peierls theorem.
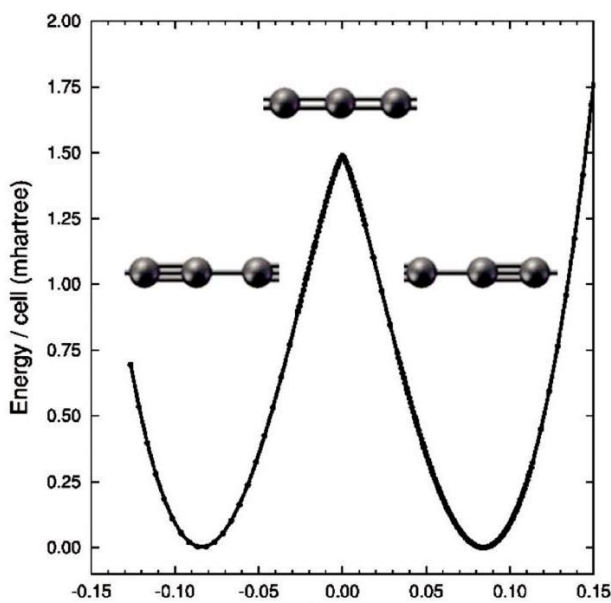
Fig. 1.5 potential energy surface of the wires as a function of BLA.

Although for the infinite chain there is a specific BLA value corresponding the minimum energy (Fig. 1.1) for which the structure is stapled, however, calculating the energy gap dependence on the BLA is insightful. DFT calculations have been done on the infinite chain assuming different BLA values.
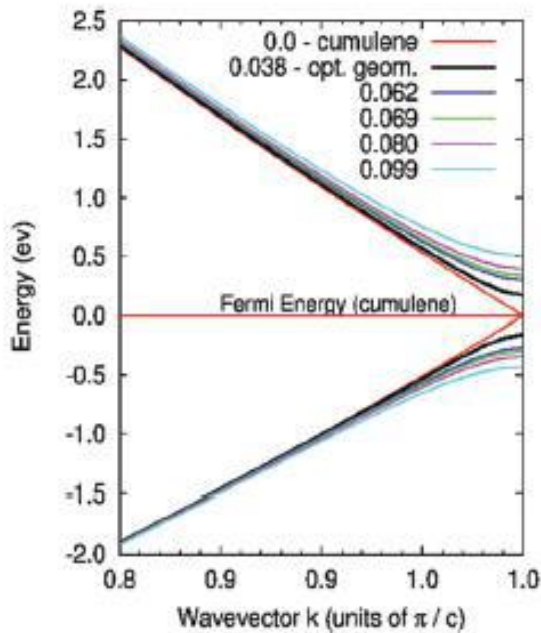
Fig. 1.6 Band structure of the infinite chain possessing different BLA values. [8]

From Fig. 1.6 we can notice how the energy gap is proportional to the BLA values. The gap increases with increasing BLA. As we will see later, this model is very useful in describing many of the properties of the finite chains as well, if the right value of the BLA was adapted. BLA turned out to be a very useful parameter when it comes to carbon atomic wires. Many properties are dependent on its value. Energy gap as was demonstrated, reactivity, π-conjugation, and even charge transfer, optical properties, all these and more can be tuned by changing the BLA value. The BLA is indeed a direct measure of the π-electrons delocalization. All those parameters vary with varying the degree of the π-electrons delocalization.

1.2.2 Vibrational properties
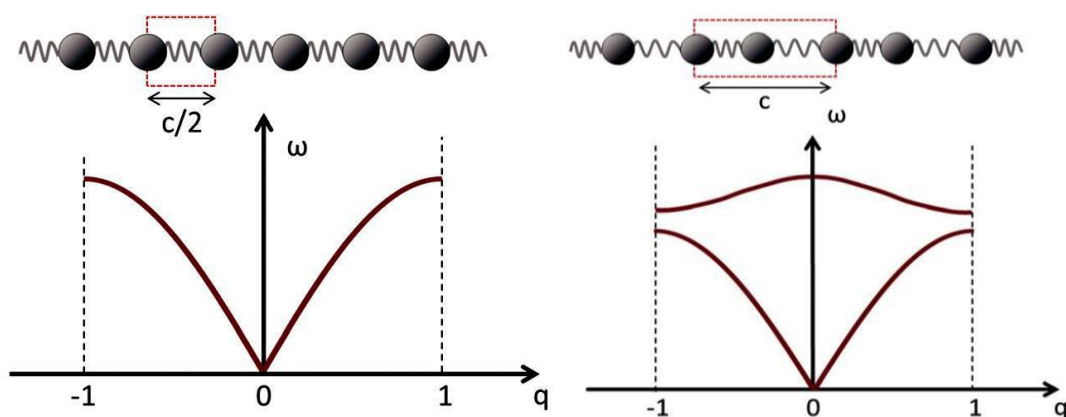
Fig. 1.7 Phonon dispersion relation for two Carbyne configurations. Cumulene (left), and polyyne (right) [7].

Due to the high polarizability of the π-electrons cloud, systems with π-conjugation possess a strong electron-phonon interaction, which makes their vibrational properties very important. A simple solid-state model has been adopted to study the vibrational properties of Carbyne.

In Fig. 1.7 the phonon dispersion relation is represented for cumulene and polyyne. As cumulene is a one-dimensional crystal with one atom per unit cell, cumulene only has three acoustic phonons, two transversal and one longitudinal. As the number of optical phonons equals 3N-3, where N is the number of atoms per unit cell, cumulene does not have any optical phonons. Polyyne, on the other hand, is a one-dimensional crystal as well, but with two atoms per unit cell. Thus, its phonon dispersion relation is composed of three acoustic phonons, two transversal and one longitudinal, in addition to three optical phonons, two transversal and one longitudinal as well.
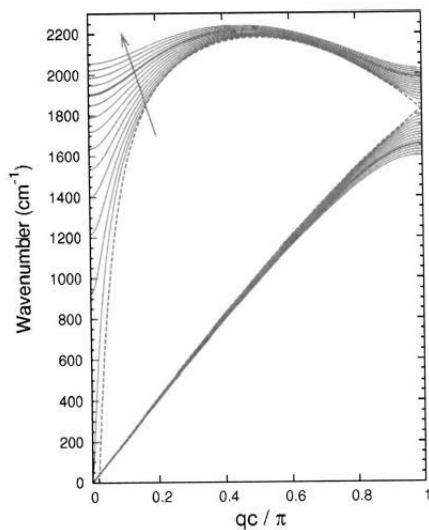
Fig. 1.8 Longitudinal acoustic (LA), and longitudinal optic (LO) phonons dispersion relation for different BLA values. BLA increases with the arrow [9].

In Fig. 1.8 one can see the clear dependent of the longitudinal optical phonons on the BLA value. The overbending of the phonon dispersion relation can be attributed to the interactions beyond the nearest neighbor approximation. The delocalized π-electrons are responsible for the long-range phonon interactions in such systems. Since the BLA is a measure of the delocalization of the π-electrons, then it is clear why the long-range phonon interactions increase with increasing the BLA.

1.3 Finite sp-carbon chains

Finite sp-carbon chains have preserved some of the infinite chain properties. On the other hand, some other properties get strongly affected by parameters that did not play a role in the infinite chain picture. The effect of the end groups and the length of the chain are the main parameters that control the chain properties in this case. Indeed, Yang and Kertesz demonstrated the limit that the Peierls distortion starts to lose its effect, and the effect of the end group starts to appear instead. Through computational efforts, they set 52 carbon atoms as the transition limit [10].

1.3.1 Effect of end-groups

The effect of the end-groups of the wire on its properties can be strongly detected in the BLA values variations with different end-groups. In the case of the wires terminated with -CH group, for instance, the BLA takes high values. This is because the last C-H bond of the chain forces a pure single bond character to one side of the last carbon atom in the chain, which accordingly forces the next bond to be purely triple bond and force the alternation of a single triple. While in the case of the wires terminated with $-CH_2$, the end group, in this case,

forces the next bond to be a double and so on. The BLA values, in this case, tend to be very small (less than 0.05 A). However, never yet zero, and in this case and regardless that the BLA value is not zero, we can still call the system a structure with a cumulenic character, while the previous one can be called that it has the polyynic character.

Another example of the effect of the end-groups is when chains terminated with sp^2 carbon domains were synthesized. Indeed, the presence of sp^2 termination led to a decrease in the BLA values. However, it is not the size of the sp^2 domain that was the main element; in fact, it was the nature of the sp^2-sp bond that mostly affects the BLA values. Different use of end groups was proposed by Tykwinski and his group when they managed to synthesize relatively short sp-carbon chains terminated with two phenyl groups on each side. In such a way, a double bond was forced on the wire [11] [12]. Indeed, this technique was successful in inducing the cumulenic character, achieving very low BLA values and relatively low band gap. Two of those systems are the main investigated molecules in this thesis.

1.3.2 Effect of the chain length

The effect of the chain length is rather straight forward. With increasing the chain length, the BLA values decrease. This is indeed expectable, since with increasing the length of the chain the π-conjugation increases as well. However, this is the general trend, but the parity of the number of carbon atoms in the chain plays a role as well. An odd number of carbon atoms in the chain decreases the BLA values as it helps in forcing the double bond character in cumulenic like chains. Although with increasing the number of carbon atoms in the chain the BLA values decrease, however, it will never be zero. As the chain length reaches the infinite chain limit, the effect of Peierls distortion will keep the BLA at the value predicted by the solid-state model for infinite chains.
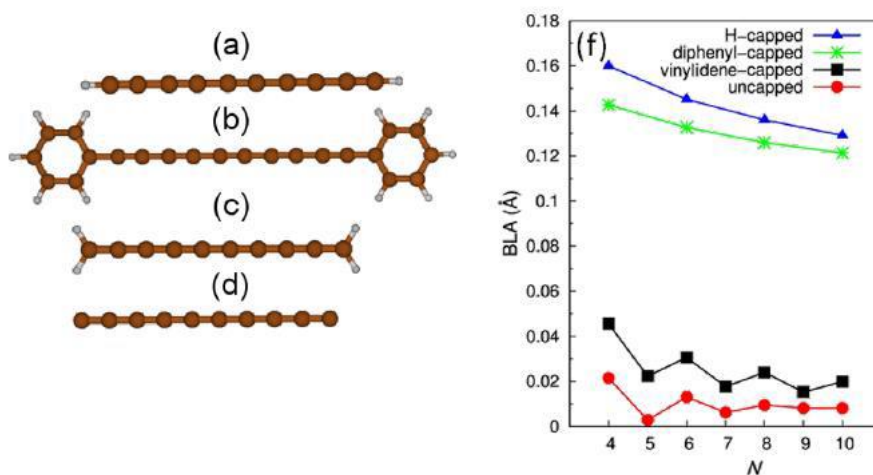
Fig. 1.9 (a-d) carbon atomic chains with different terminations hydrogen-capped (a), phenyl-capped (b), vinylidene-capped (c) and uncapped (d). (e) Bond length against the bond index for different terminated chains, (f) BLA as a function of the number of atoms in the chain for different terminated chains. The data are obtained using DFT calculations. [13]

An excellent example to summarize what has been said is in Fig. 1.9, where using DFT calculations, bond length, and BLA values have been calculated for different chains with different terminations. From the second panel, the trend of the BLA against the number of atoms in the chain is clear as it decreases with increasing the number of atoms. From the same panel, we also notice how an end-group which forces a double bond tend to decrease the BLA values of the chains to the cumulenic regime, as in the case of the vinylidene-capped chain. The difference between the cumulenic regime and the polyynic regime is also noticeable in that graph.

We conclude that, by proper choice of the end-group and the chain length, we can achieve a wide range of properties' tunability which is very appealing for both fundamental science and technological applications.

1.3.3 Synthesis

When it comes to chains synthesis, things are tricky due to the high reactivity of sp-carbon. There are mainly two ways of chain production: chemical methods and physical methods. One example of chemical methods is polymerization. In Fig. 1.10 we can find different physical techniques for carbon chains production. Arc discharge in liquid is a technique where two graphite electrodes come close, and a high voltage is applied between them creating an arc discharge where different carbon forms get produced including sp-carbon chains. Another technique is pulsed laser ablation in liquid, where a graphite target (or carbon-rich target) get radiated with nanosecond pulses of laser. Sp-carbon chains get produced as well along with other carbon forms. The common property between those techniques is the presence of a confining medium (liquid in this case and in the other techniques inert gas is used). This confining medium forces the carbon atoms to aggregate out of equilibrium which induces the sp-hybridization and the production of the chains.
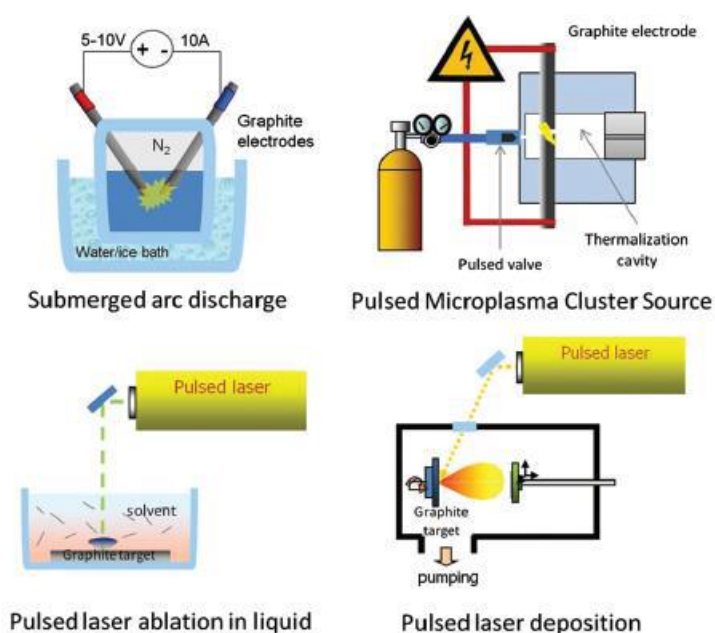
Fig. 1.10 different physical techniques for carbon chains production [7]

1.3.4 Stability issues' solutions

The major difficulty for both chemical and physical synthesis techniques are, in fact, the bottom-up fabrication of longer and longer molecules approaching the infinite limit. Indeed, the biggest challenge was the high reactivity of the sp-carbon in the chain and its tendency to crosslink transforming into more stable sp^2-hybridization carbon form. Therefore, any attempt to induce stability should focus on the elimination of the crosslinking effect. A successful try was done by growing long sp-carbon chain inside the core of a double wall Carbon Nanotube (DWCNT) [14]. This work has shown the possibility of producing long chains if the interaction with the environment has been avoided. Another way to prevent the crosslinking is by using an ionic liquid with a low concentration of the wires. The low concentration prevents wires interaction with each other and therefore crosslinking [15]. However, stability in ambient atmosphere is mandatory for technological applications. Interaction with metals found to be a stabilizing factor. A mixture of the wires with silver nanoparticles found to induce stability in both solution and solid state. It was found that hydrogen terminated chains maintain their structure for several months when mixed with silver nanoparticles. The mixture was to perform Surface Enhanced Raman Spectroscopy (SERS) measurements. However, it was found that the mixture maintained almost the same sp-carbon signal for several months as shown in Fig. 1.11 (a). The

measurements were done in solution and after the mixture was dried to form a film of hydrogen capped polyyne chains and silver nanoparticles [16].

A very important technique was proposed by Tykwinski and Chalifouz, to use large end groups which can induce a kind of steric hindrance preventing the wires coming close (Fig. 1.11 (c)). This technique indeed was a very successful way that led to the production of very long chains (up to 44), very close to the infinite wire limit [17]. Cataldo et al. have shown that systems composed of sp^2-carbon structure combined with sp-carbon chain are significantly stable in ambient conditions [18] (Fig. 1.11 (b)).
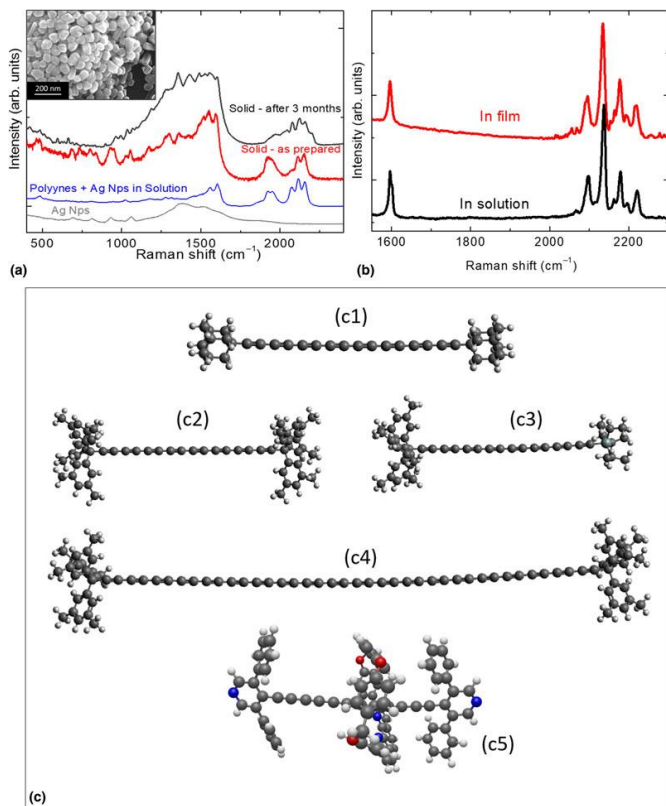
Fig. 1.11 Different techniques to induce stability. (a) scanning electron microscope (SEM) image of silver nanoparticles mixed with hydrogen capped polyyne chains and the Raman signal of sp carbon along several months. (b) Raman signal for phenyl terminated chains showing stability in solution and ambient atmosphere. (c) different chains terminated with bulk groups to induce steric hindrance and prevent crosslinking [2].

1.4   Characterization techniques

In the last decade, attention has been grabbed to sp-carbon chains as a critical member of the family of carbon structures and as a class of materials itself.

This attention has been strengthened by the preparation and characterization of different chains with different lengths and end groups. Nevertheless, and even though the theoretical work is at advanced states, however, the experimental work is still at its early stages. This is in fact due to the difficulties previously mentioned regarding the stability issues. This makes the characterization of sp-carbon chains extremely difficult. Moreover, the identification of sp-carbon within other carbon hybridized structures is far from trivial. Here Raman and UV-Vis spectroscopy play a key role in the realization of sp carbon as well as differentiating between cumulenic and polyynic chains.

1.4.1   Raman spectroscopy

Raman spectroscopy is a nondestructive technique (when done correctly) probing the vibrational properties of the material. It is highly sensitive to crystallinity and local order. It is used for crystals, nanocrystals, and molecules in solution and solid state.

It relies on Raman scattering (inelastic scattering) of monochromatic light, usually from a laser in the visible, near infrared, or near ultraviolet range. The laser light interacts with the material vibrations (phonons), resulting in the energy of the photons that are scattered increase or decrease. The change in energy gives information about the vibrational modes in the system.
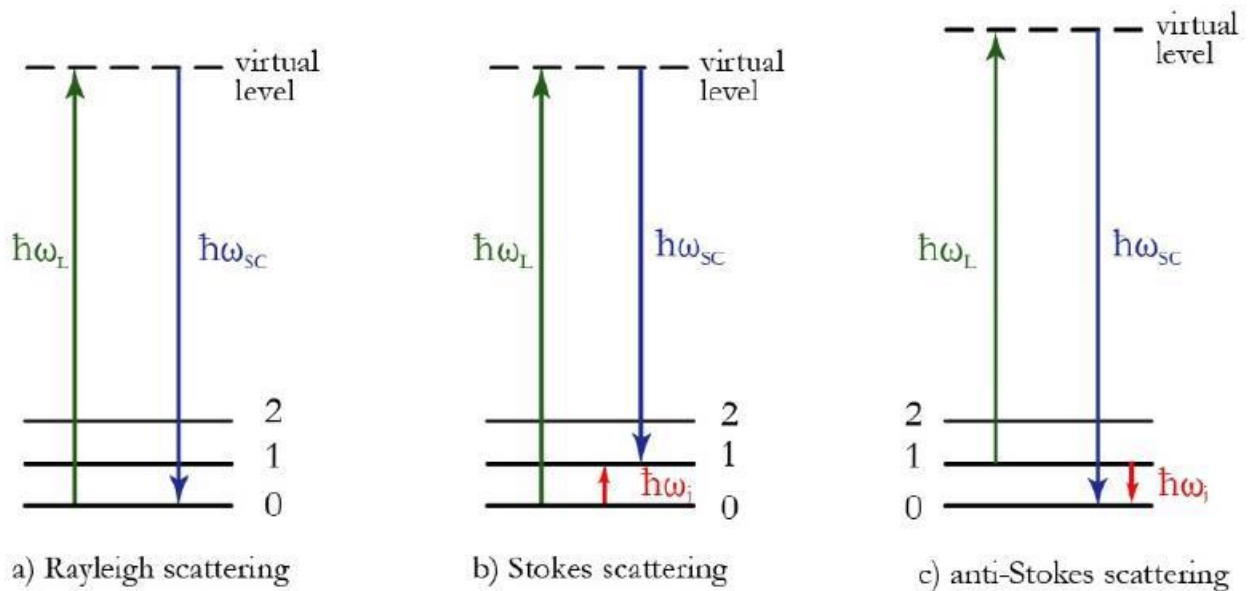
Fig. 1.12 schematic drawing of the three scattering photons.

When the material gets radiated with a photon of frequency ω_L and an electron absorbs the photon and get excited to a virtual state, two main decaying processes occur (the absorption and the decaying processes are instantaneous and not real). A decaying process which is responsible for the elastic scattering of the photon (Rayleigh scattering), on which the electron gets excited from the ground state and decays to the ground state emitting a photon with the same frequency ω_L. However, there is the possibility of an inelastic scattering (Raman scattering). When the electron decays to a vibrational state different from the ground vibrational state, a photon gets emitted with a frequency equal $\omega_L - \omega_i$ where ω_i is the frequency of the phonon which was created in the process, in this case, we have the Stokes scattering. When the electron gets excited from a vibrational state different from the vibrational ground state but decays to the ground state, a photon with a frequency equal $\omega_L + \omega_i$ is emitted, and in this case, a phonon gets annihilated in the process, and we have the anti-stokes scattering. This electron-phonon interaction is responsible for the phenomenon of Raman scattering.

However, according to quantum theory and adapting the harmonic approximation model, two main selection rules results. First, only phonons at the center of the Brillouin zone are Raman active (vibrations which cause anisotropic polarizability). Second, a second order excitation is forbidden under the harmonic approximation and has a very low probability if the harmonic approximation was relaxed.

Raman techniques, however, have always been a critical characterization tool when it comes to carbon-based materials. This is because of the symmetry of carbon structures (the tetrahedral for sp^3-carbon, the trigonal planar for sp^2-carbon and the linear for sp-carbon), that allows for the presence of Raman active normal modes.
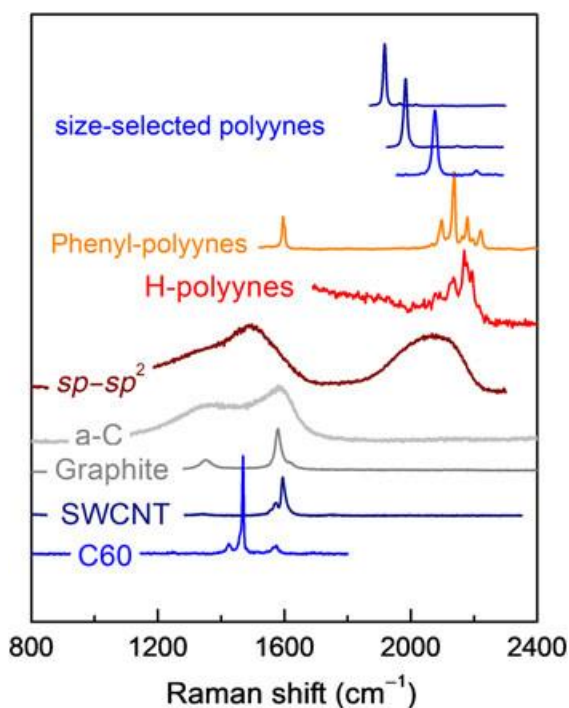
Fig. 1.13 Different Raman signals for different carbon structures. We can notice the absence of the overlap between the signals [2].

Another reason which makes Raman spectroscopy a powerful tool when characterizing carbon structures is the different Raman fingerprint signals for different carbon structures (see Fig. 1.13). The absence of overlap between the different structures' signals is in fact, due to the sensitivity of Raman spectroscopy to the hybridization state of the carbon atoms, and the chemical environment surrounding the bonds.

As shown in Fig. 1.13, sp^2-carbon Raman fingerprint is within 1300-1600 cm^{-1} region, while for sp-carbon it lays in the region 1800-2300 cm^{-1}. Uncovered by any other signals from any different carbon systems. However, adopting the infinite sp-carbon chains model, only polyyne can show a Raman signal. That is because polyyne has optical phonons while cumulene has only acoustic phonons which according to the previously mentioned Raman selection rule, their frequency is very low and practically cannot be seen. This is true only for the case of the infinite wires when the BLA value is precisely zero. However, Francesco Innocenti et al. have shown that finite cumulene chains could be detected using Raman spectroscopy. Using DFT calculations, they have shown that the longitudinal mode which is responsible for Raman signal of polyyne chains resulting from the BLA oscillation, get almost suppressed for cumulene chains. However, other longitudinal modes still can be observed for cumulene chains [19]. These longitudinal modes can be detected thanks to the chain end-group effect.

The main vibrational mode which is responsible for the chains Raman signal is what is called the effective conjugation coordinate (ECC) mode. It is an out of phase CC stretching mode, and its origin is the BLA oscillation. This mode shows a significant dependence on the BLA values. In order to understand this dependence, one should understand the effect of the π-conjugation on the vibrational frequency of the chain. Indeed, for increased π-electrons delocalization, a decrease in the bond energy follows. Which results in a red-shift in the vibrational frequency of the bond. In Fig. 1.14 the Raman spectrum of phenyl-capped polyyne chains with different lengths is reported. The detailed analyses of the sp-carbon area in the spectrum (upper panel) with the comparison to the DFT calculated spectrum for different chain lengths (lower panel) is reported. We can notice the red-shift of the sp-carbon beak going for longer chain lengths. Another important information is the relative intensity of the peaks corresponding to different chain lengths, giving information about the relative concentration for each length.
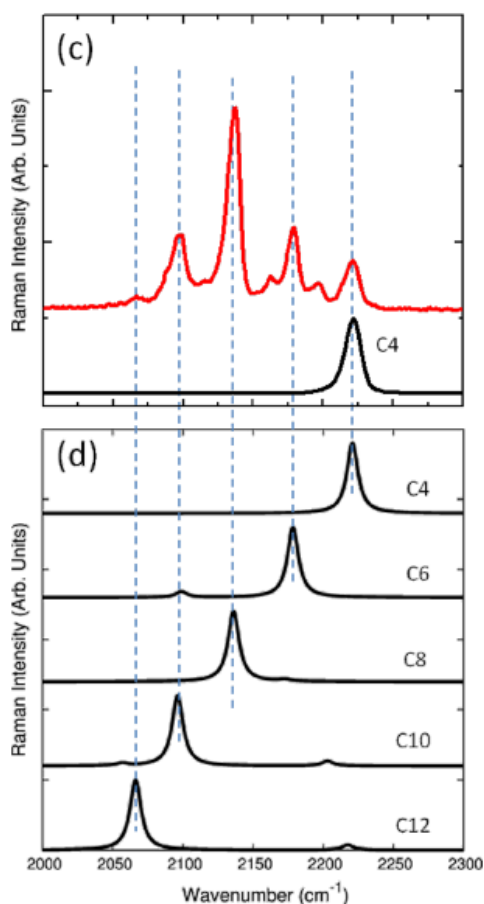
Fig. 1.14 Raman spectrum for phenyl capped polyyne chains with different lengths. (a) the spectrum of the chain in solution with solvent spectrum bellow for comparison, the arrow shows the beak from the phenyl termination while the dotted square shows the signal from the sp-carbon chains. (b) the spectrum of the solid state in comparison with the molecules in the solution. (c, d) detailed analyses of the sp-carbon area in the spectrum (c) with the aid of DFT calculated spectrum for different chain lengths [13].

As was demonstrated Raman spectroscopy is indeed a powerful tool in the characterization of sp-carbon chains and sp-carbon structures in general. With the aid of DFT calculations, information regarding the chain length and the concentration of the different chains can be gained. Another important information is the type of the chain, whether it is cumulenic or polyynic. As will be demonstrated along the thesis, many steps in the research work on carbon atomic wires are mainly dependent on Raman spectroscopy which again shows the importance of this technique as a characterization tool for sp-carbon, as it is for other carbon systems as well.

1.4.2   Ultraviolet-Visible (UV-Vis) absorption spectroscopy

UV-Vis absorption spectroscopy is a nondestructive technique probing the electronic transitions in the material. It is a widely used technique in the field of organic materials both in solution and in the solid state as well.

When light passes through the material, some of it gets absorbed, and some get scattered and transmitted. The absorption process takes place when an electron absorbs the incoming photon and gets excited to an available electronic state. The energy difference between the initial and the final state must be equal to the energy of the absorbed photon. The photon of least energy to get absorbed gives information about the first allowed electronic transition. The wavelength at which the maximum number of photons get absorbed gives information about the most probable electronic transition in the material.
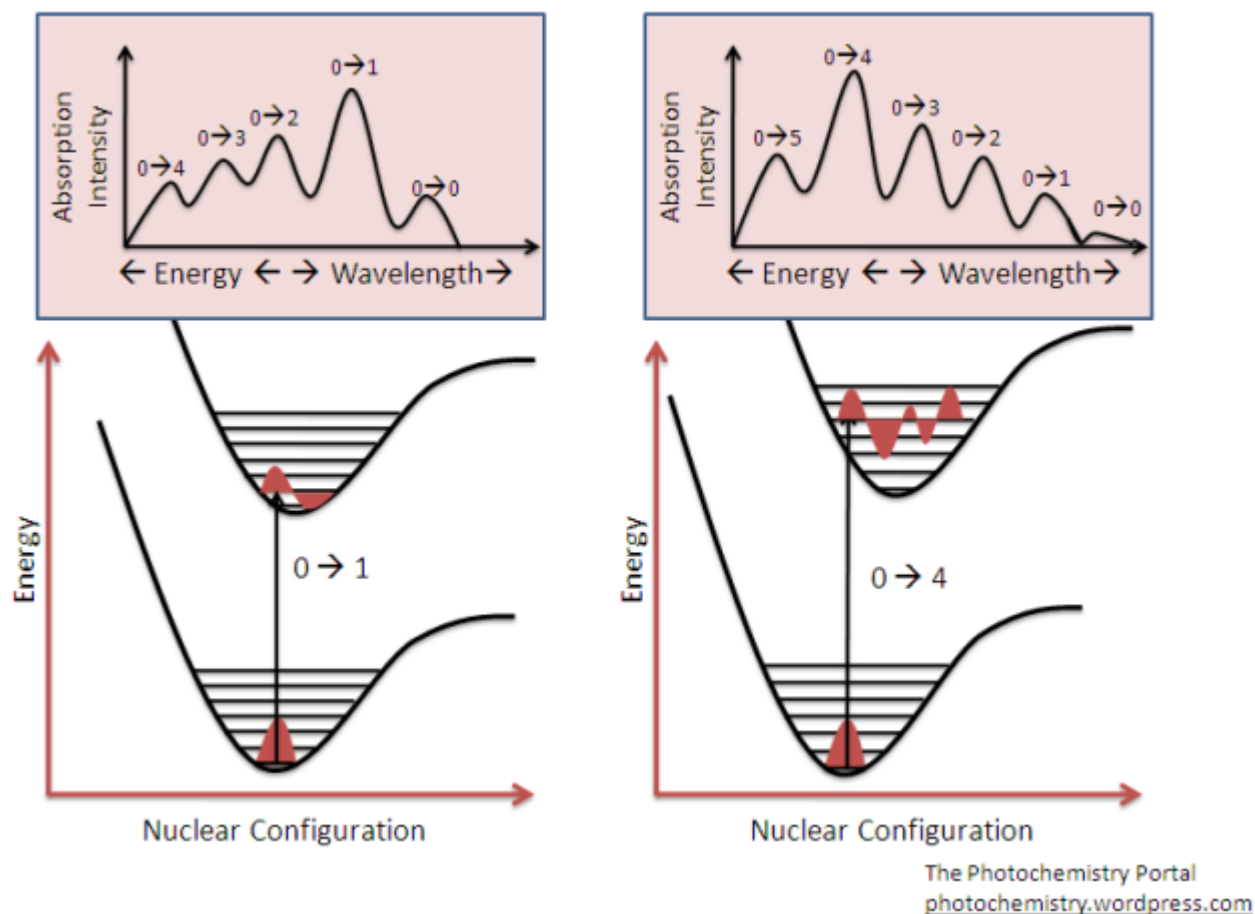
Fig. 1.15 Schematic qualitative diagram of the electronic ground state and the first excited state with vibrational states for each electronic state. On top, there is the absorption spectrum corresponding to those electronic transitions. The arrow indicates the most probable transition. The numbers indicate the vibrational energy levels for each electronic level [20].

In Fig. 1.15 we can see a schematic qualitative diagram for a diatomic molecule. The diagram describes the ground and the first excited electronic states. Each electronic state encloses different vibrational states. Following the harmonic approximation, the vibrational states are equally spaced. The two diagrams represent two different molecules. In the first diagram, the overlap between the ground and the excited states is higher than that of the second molecule. This degree of overlapping is an indication of the degree of the molecular geometry deformation upon electronic excitation. The arrow indicates the most probable excitation process, which is direct excitation. The absorption spectrum on top reflects the different excitation processes. The lowest energy absorbed photon corresponds to the lowest energy excitation process. The highest intensity peak in the absorption diagram corresponds to the most probable excitation process. The difference between one peak and the one that follows corresponds to the difference between the vibrational energy levels. It is worth mentioning that the first allowed transition usually is the transition between the highest occupied molecular orbital (HOMO) and the lowest unoccupied molecular orbital (LUMO), however, in organic materials this is not always the case. Two main pieces of information can be deduced from the UV-Vis spectrum: first, the optical band gap of the material. Second the difference between the vibrational energy levels of the material.

When it comes to sp-carbon atomic chains, UV-Vis spectroscopy is an extremely powerful tool in characterizing and identifying different types of chains.

15

[n]	[n]tBuPh λ_{max} / nm (E_g / eV)	[n]Mes λ_{max} / nm (E_g / eV)
[3]	424 (2.92)	—
[5]	500 (2.48)	460 (2.70)
[7]	564 (2.20)	560 (2.21)
[9]	664 (1.87)	666 (1.86)
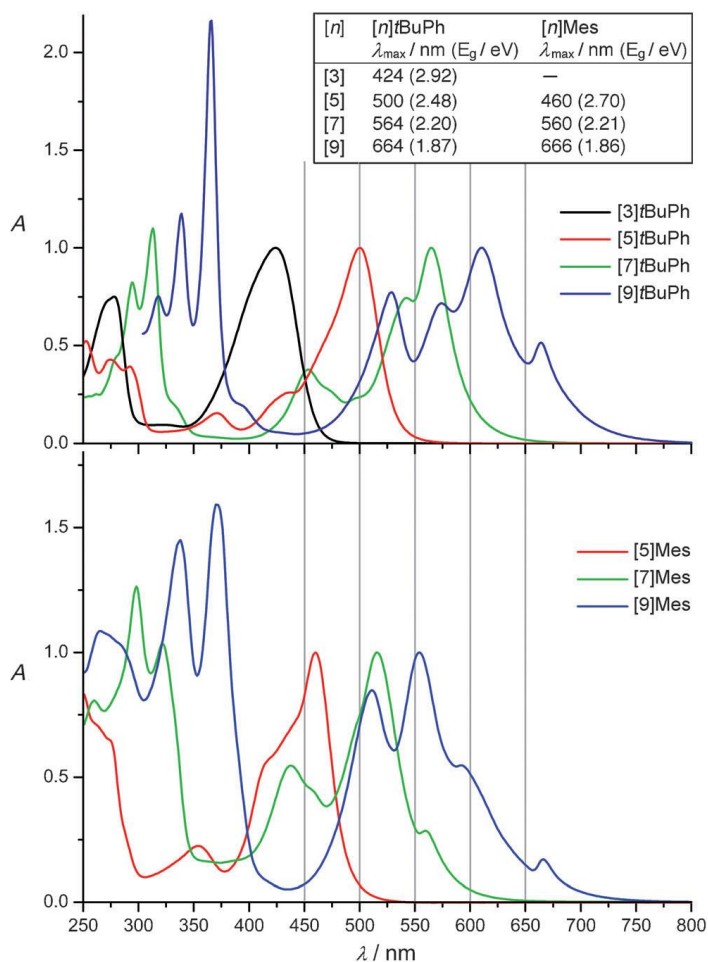
Fig. 1.16 UV-Vis spectra for two types of cumulenic chains with different end-groups. For each type, the spectrum is taken for different chain lengths. The number in square brackets is the number of double bonds in the chain. The table indicates the lowest-energy absorption maximum and the corresponding energy value [21].

In Fig. 1.16 we can find the UV-Vis spectra for two different types of cumulenic chains with different end-groups for each type. Each spectrum shows the absorption of the cumulenic chains with different chain lengths. From the graph, we can deduce different trends and features for cumulenic chains. First, a characteristic feature is the presence of two separate main bands of absorption. This is, however, a characteristic feature for cumulenic chains, while for polyynic chains the red-shifted absorption band is absent. Second, going to higher chain length results in red-shift in the absorption spectrum, indicating a decrease in the optical band gap with the increase in the chain length. Another insight is that the increase in the chain length is accompanied by an increase in the spectrum complexity. The lowest-energy absorption maximum shows the decrease in the effect of the end-groups going to longer chains. The difference in the lowest-energy absorption maximum between the chains with the same length but different end-groups is decreasing going from shorter to longer chains.

The last example shows the rich information that can be deduced from UV-Vis spectroscopy when it comes to sp-carbon atomic chains research. That indeed indicate the significance of this technique for both the characterization of the wires and the differentiation between different wires species.

1.4.3   Electrical Transport characterization

Charge transport across the chains is significantly important for fundamental science and technological applications especially in the field of electronics. However, electrical transport characterization of the sp-carbon chains is far from trivial.

Too many parameters affect the results of an electrical transport experiment. The role of contacts, the atmosphere effect, the interaction with light and the temperature dependence, all that and more affect the results, making it difficult to conclude a generalized rule. Stability of the wires structure throughout the measurements is a big issue as well. Indeed, theoretical work is far advanced regarding transport properties than experimental results.

With the aid of first principle calculations N. D. Lang and Ph. Avouris demonstrated that the parity of the number of carbon atoms in sp-carbon chains affects the conductance of the chain significantly. However, they assured that the density of states at the Fermi level and the matching between the chains and the metal electrodes is the leading factor in the charge transport process [22]. The same authors performed calculations demonstrating the voltage drop across the wires in contact with metal electrodes (differential resistance). They were able to demonstrate that at zero voltage a charge transfer from the metal to the chain occurs; however, it creates a barrier causing bending in the wire. This bending leads to significant decrease in conductance [23]. Another work addressing the charge transfer between the wires and metal nanoparticles was done by A. Milani et al. showing that when the wires get in contact with silver nanoparticles, a charge transfer occurs leading to polyynic-cumulenic transition. This transition, however, is a function of the wire length. This was indeed confirmed experimentally through surface-enhanced Raman spectroscopy (SERS) measurements, which showed an agreement with the calculated value of charged wires [24]. Another interesting theoretical demonstration was done by Renato Batista dos Santos et al. showing that in graphene-wire-graphene configuration, an electric field parallel to the wire can induce semiconductor to metal transition. This transition is due to the control of the spin polarization inside the wire through the applied electric field [25]. The strong electron-phonon interaction and the high Debye temperature of the one-dimensional carbon structures induced C. H. Wong and his group to take a theoretical quest, hunting for high-temperature superconductivity in reduced dimensions carbon structures. Indeed, they demonstrated that different configurations of sp-carbon structures with specific geometrical parameters could show superconductivity up to a temperature window of around 100 K. However, the maximum temperature is different for each structure [26].

Moving from theoretical predictions to experimental work, Ovidiu Cretu et al. was the first group to report electrical current measurements of a single carbon atomic wire (see Fig. 1.17). The current, however, was lower than what was expected in theory and they attributed that to the strain on the wire which increases the BLA value [27]. Same work was done by A. La Torre et al. who were able to measure the conductance through the graphene-wire-graphene system. They managed to show the semiconductor behavior predicted for polyynic chains and the metallic behavior for the cumulenic chains. Moreover, they showed that, when the axial strain is relaxed on the chain, zero-point vibrations overcome the difference in the bond length between the single and the triple bonds, which induced a transition from a polyynic chain to a cumulenic chain, accompanied by semiconductor to metal transition as well [28]. L. T. Cai and his group and Ferdaous Ben Romdhane and his group demonstrated through electrical transport measurements that, in the case of a single chain or an assembly of molecules passed on sp-carbon chains the contacts play a crucial role in the overall conductivity of the system. The formal group performed their measurements on single chains connected to sp^2 and sp^3 carbon, showing that sp^2 type contacts increased the conductivity of the system with multiple order of magnitudes in comparison to sp^3 type contacts [29]. On the other hand, the latter group performed their measurements on an assembly of molecules passed on sp-carbon. They demonstrated that symmetric contacts and the match of the Fermi level's density of states of the molecules and the metal contacts increase the overall conductivity of the system [30].
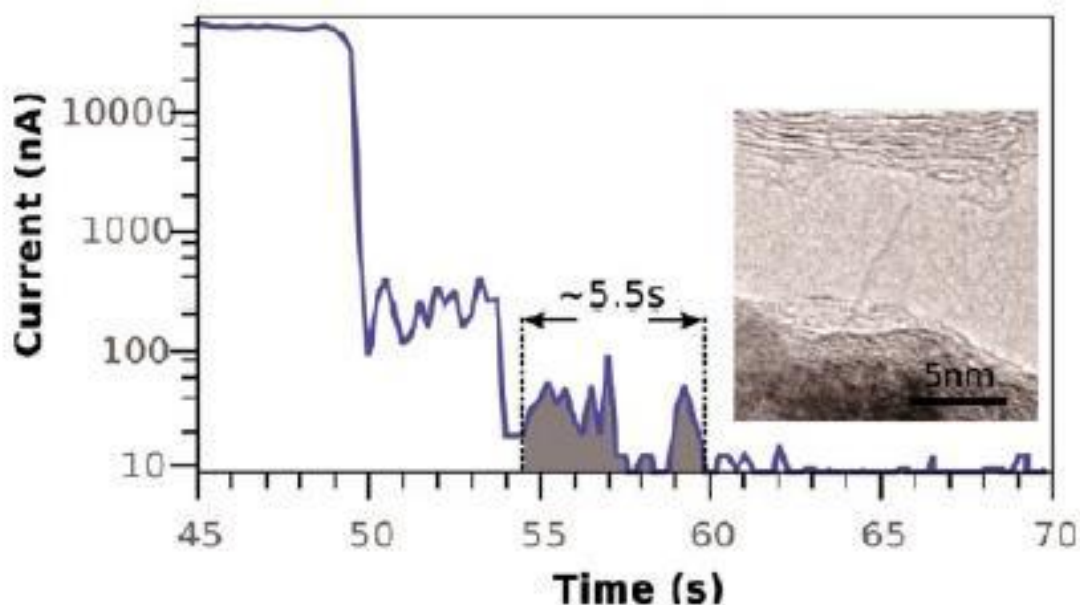
Fig. 1.17 Conductivity measurement of the in-situ prepared graphene-wire-graphene system as shown in the SEM image. The gray area is the current when the wire was connecting the two graphene ribbons [27].

From the previous discussion, we can conclude that electrical transport characterization of carbon atomic wires is of great difficulty. Few experimental works were done in this area in comparison to the theoretical ones. Huge diversity in the results reflecting the sensitivity to measurement's set up. Nevertheless, the significant change in conduction in response to external factors can be of great interest to the next generation electronics.

1.5 Potential perspectives

In the recent years and after the efforts in the field of sp carbon-based systems from chemical and physical synthesis techniques to characterization and understanding of the fundamental physicochemical properties, experience has been gained in dealing with these systems for optimizing their behavior towards possible future applications in science and nanotechnology.

The ability to tune the properties of the wire through changing the end-groups and the wire length is appealing. It opens many technological possibilities and makes the sp-carbon atomic chains a fertile field for prospective applications.

One good example is what has been proposed by Fanghao Hu et al. As demonstrated, a change in the chain length or the end-group can induce a shift in the sp Raman peak. By using this principle, they designed a whole family of carbon atomic wires as shown in Fig. 1.18, showing distinct Raman peaks and used this behavior in super-multiplexed optical imaging and barcoding [31].

In the theoretical work of N. D. Lang and Ph. Avouris they predicted conductance values for even number sp-carbon chains of around double the quanta of conductance. However, experimental results still far from this value. Sp-carbon chains also present itself as a simple system for studying superconductivity at low dimensionality as was proposed by C. H. Wong and his group. Indeed, this is another example showing the gap between the theoretical and experimental work in this field.
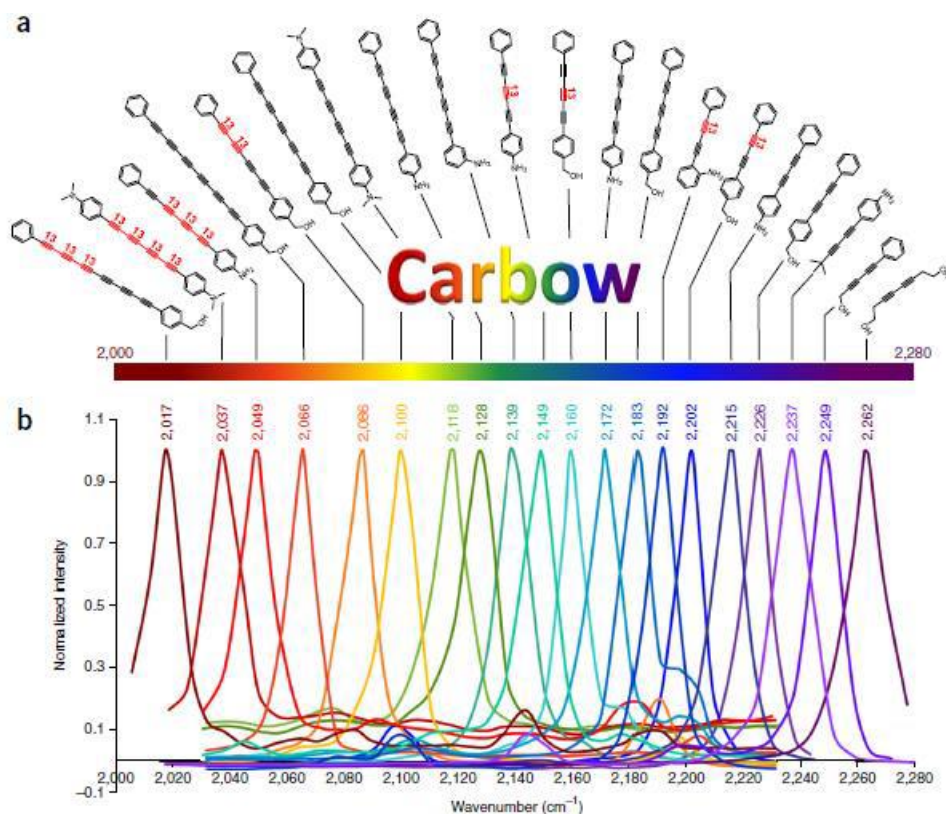
Fig. 1.18 Carbon rainbow, 20 different polyynic chains on top (a) with their sp-carbon Raman signal bellow (b) [31].

Another outstanding possibility for all carbon nanoelectronics is the graphene-wire-graphene systems. As mentioned in the previous section, it was found through computational methods supported by experimental measurements that a process of charge transfer occurs between the nanoparticles and the wires during SERS measurements on diphenyl-capped polyynic chains, which stabilize the wires and induce a transformation from polyynic state to cumulenic state. Such behavior was not observed for hydrogen-capped polyynic chains for example, which indicates that the charge transfer and the polyynic-cumulenic transition is a peculiar property of the sp2 end groups. Some of those systems have been already synthesized and showed very promising results. One example is what mentioned in the previous section and the possibility of strain induced semiconductor-metal transition. Another way to induce a semiconductor-metal transition is also possible using a parallel electric field as was mentioned in the previous section. However, this last result was theoretically predicted, and experimental validation is still needed.

Sp-carbon atomic wires can also be the building blocks for novel materials and complex nanostructures. A good example is the hyperiids systems, graphyne (GY) and graphdiyne (GDY), which are one of the appealing future structures of that kind. Those systems are a well-organized sp and sp2 carbon atoms ordered in crystalline form instead of individual chains, an extended 2D crystal formed of sp2 carbon hexagons which are interconnected by sp-carbon chains with different lengths. Although the theoretical investigation of these systems started back in 1987 as a modified form of graphene, however, they gathered more attention in the last decade due to their prospective applications in the view of their predicted peculiar electronic structure. Indeed, the extended crystal models of these systems are like their father graphene, sustaining the famous Dirac cones. Promisingly enough, primary bottom-up synthesis of such systems has been successful. In particular, the group of Haley has been extremely active in this area, synthesizing sub-fragments and 2D molecules of GDY of different dimensions and topology as shown in Fig. 1.19 [32].
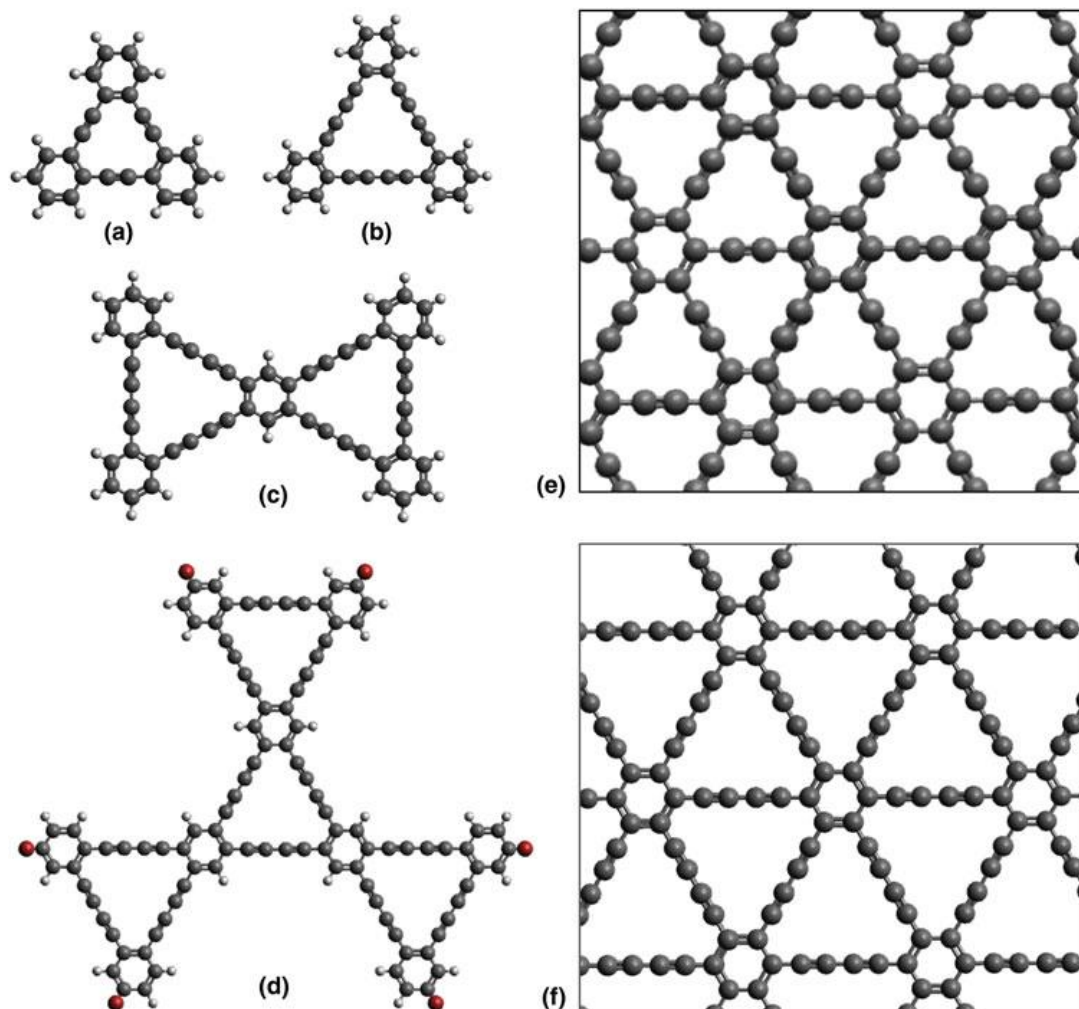
Fig. 1.19 Molecular fragments of graphyne (a) and graphdiyne (b, c, d) (left). Extended crystal models for graphyne (e) and graphdiyne (f) (right) [2].

As was demonstrated in this chapter carbon atomic wires' field is rapidly developing with too many opportunities for improvement and research. A lot of outstanding properties were theoretically predicted for the wires. However, much experimental work is still needed to close the gap between theory and experiment, which makes sp-carbon chains an exciting field for research and a very promising field for technological applications.

2 Electrical transport in organic semiconductors and organic field effect transistors

In a material containing mobile charges (conductor or semiconductor) when exposed to an electric field ($\mathbf{E}$) of external origin, an irreversible charge transport phenomenon (electric current I) occurs, which removes the crystal from its thermodynamic equilibrium. From a macroscopic point of view (adopted by the thermodynamics of irreversible processes) when the electrical field is small, we are within the linear response regime. In that case, the phenomenological Ohm's local law holds:

$$\boldsymbol{j} = \sigma \mathbf{E} \quad (2.1)$$

Where $\boldsymbol{j}$ is the charge current density vector (bold symbols are vectors). Its flux through a surface S is the current, represents the amount of charge per unit time, flowing through the surface:

$$I = \int_S \boldsymbol{j}.\boldsymbol{n} dS \quad (2.2)$$

where $\mathbf{n}$ is the unit vector pointing in the direction of the current.

When the electric field moves the crystal from its thermodynamic equilibrium, a net flux of charges is generated. This flux moves with a net velocity which is called the drift velocity ($\boldsymbol{v_d}$). This velocity is proportional to the electric field, and the proportionality constant is called the drift mobility (μ):

$$\boldsymbol{v_d} = \pm \mu \boldsymbol{E} \quad (2.3)$$

The drift mobility can be connected to the current density through its relation with conductivity (σ):

$$\sigma = en\mu \quad (2.4)$$

where e is the electron charge and n is the number of charge carrier.

2.1 Organic semiconductors electrical characteristics

However, organic semiconductors are formed of molecules or macromolecules connected with weak van der Waals forces, in the order of 10 kcal/mol. This weak force is comparable to the thermal energy at room temperature, kT, where k is the Boltzmann constant and T is the temperature in Kelvin. Unlike the case of inorganic semiconductors, which have strong covalent bonds ensuring lattice rigidity and periodicity, which is negligibly affected by lattice vibrations (phonons), organics cannot be considered as a rigid body anymore and the lattice vibrations lead to loss of periodicity. Giving this, we can represent the charge carriers in this medium as delocalized electronic wavefunctions that tend to be localized by the presence of some degree of disorder, leading to a density of states heavily localized. Indeed, the conventional description of valence and conduction bands is exchanged with the HOMO and the LUMO description respectively.

In Fig. 2.1 a simple illustration of the formation of the organic semiconductor electronic structure is shown. The first panel (a) shows the structure of the potential well resulting from the nucleus Coulombic potential in the hydrogen atom, where the electron occupies the lowest energy level 1s. The second panel (b) shows the structure of the potential well of a polyatomic molecule. In this case, when the atoms come close, their core levels remain localized on each atom while their outer most energy levels get merged to form a common molecular orbital (MO) where the valence electrons get shared by the whole molecule. In this case, the difference between the HOMO and the vacuum level (VL) is the gas phase ionization energy of the molecule while the difference between the LUMO and the VL is the molecule's electron affinity. Panel (c) illustrates the case when the molecules come close forming a molecular solid. Unlike the case of the molecular formation out of single atoms, the MOs of different molecules do not merge forming one orbital because the molecules are connected via van der Waal week forces. However, the HOMO and the LUMO stay localized on their

molecules with very narrow intermolecular bandwidths. The merge of the molecular potential wells, however, occurs close to the vacuum level well above the LUMO level. The merge of the potential wells' degree, in this case, is corresponding to the degree of overlap between the molecular orbitals which is proportional to the intermolecular distances. In panels (d and e) a schematic illustration of the HOMO and the LUMO of the molecular solid together with the ionization energy and the electron affinity. The ionization energy of the solid is slightly lower than that of the isolated molecule and the electron affinity is slightly higher. This difference is due to the multi-electronic electronic effects wherein the solid state, the electronic polarization of the surrounding molecules stabilizes the ionized one.
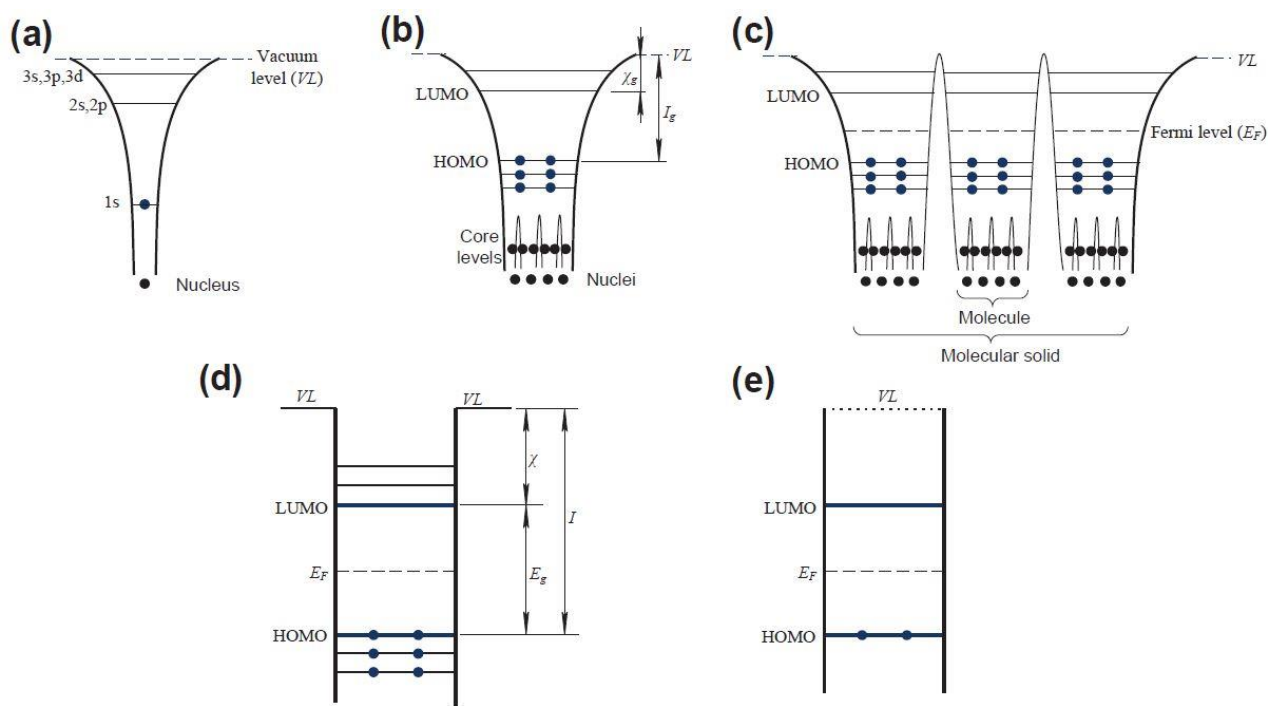
Fig. 2.1 Schematic illustration of the formation of the energy levels in molecular solids where (a) represents the hydrogen atom, (b) HOMO and LUMO of one molecule, (c) molecular solid, (d, e) simple illustration for the energy levels in the molecular solid [33].

Generally, organic semiconductors are intrinsic which means both electrons and holes contribute to the electrical conduction. However, as in the case of the inorganic semiconductor, we can still classify the organic semiconductors as p-type and n-type semiconductors. This classification is not related to the material itself, but it comes from an external origin. The organic semiconductor is p-type when most charge carriers contributing to the current are holes, while it is an n-type semiconductor if most carriers are electrons. The main factor which determines the type of charge carriers inside the organic semiconductor is the energy barrier that these charge carriers must overcome to enter or exit from the semiconductor, i.e., charge injection. This barrier is proportional to the energy levels' alignment between the electrodes and the semiconductor. Considering the case of metallic electrodes, if the Fermi energy level of the metal is closer to the HOMO of the semiconductor, then it is easier for the hole to get injected, therefore, most of the charge carriers, in this case, will be holes and we have a p-type organic semiconductor. On the other hand, if the Fermi level is closer to the LUMO than the HOMO, the case will be of an n-type organic semiconductor.

A good example of the role of contacts in the definition of the organic semiconductor type is shown in Fig. 2.2, where the energy levels of a gold electrode and pentacene, a highly studied organic semiconductor are represented. We can see that the gold Fermi level is deep in such a way that it is very close to the Pentacene HOMO which facilitates the injection of holes in this case. The difference between the Fermi level of the metal contacts and the semiconductor does not only define the type of the charge carriers, but it is one of the main

causes of the non-negligible contact resistance due to the injection barrier. However, the injection barrier is affected by many factors besides the energy level alignment at the metal-semiconductor interface. The dipolar interaction, for example, is of significant influence on modulating the injection barrier. Another example is the traps at the interface between the contacts and the semiconductor which have different effects on the contact resistance. If the traps act as intermediate states facilitating the electron or the hole transfer, they decrease the contact resistance. However, if they are deep traps localized at the interface, they can trap the charges from entering the semiconductor and, in this case, they increase the contact resistance.
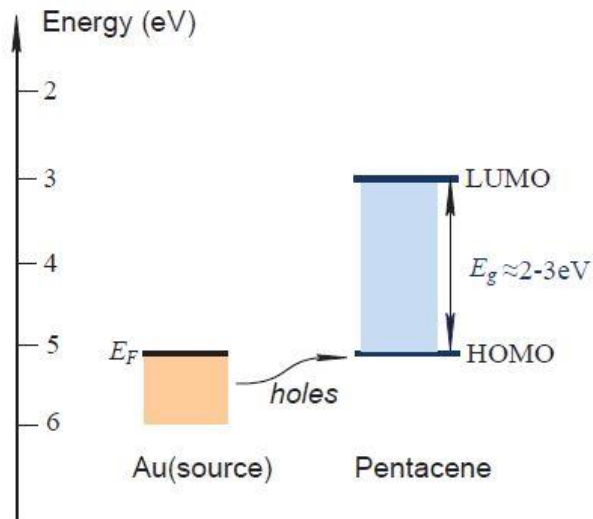
Fig. 2.2 Energy levels of a gold source and Pentacene as an example of an organic semiconductor showing the alignment of the Fermi level of the metal which facilitate hole injection [34].

2.2   Charge carriers in semiconductors (Polarons)

In 1927 Born and Oppenheimer formalized their approximation that the electrons in condensed matter follow their atoms movement while the atoms adjust their positions based on the average position of the electrons. Six years later Landau proceeded forward suggesting that a charge carrier added to an insulator, shall be self-trapped in a potential well which is created because of its presence. The carrier presence induced a shift in the equilibrium positions of the adjacent atoms coping with the new situation and creating a trapping potential well for the charge carrier as well (see Fig. 2.3). This self-trapped carrier movement is limited by the movement of the trapping atoms. Thus, it moves very slowly.
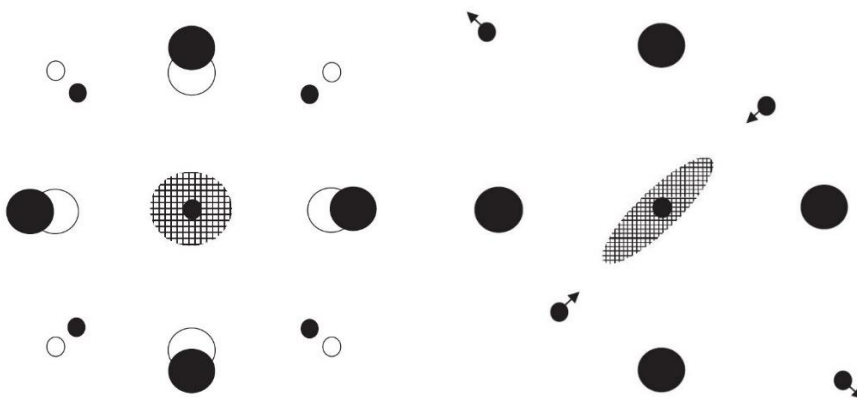
Fig. 2.3 Two examples of a polaron. The hashed area represents the charge carrier's cloud while the dark circles represent the atoms (on the left the atomic equilibrium position modification is represented by the white circles while on the right it is represented by the arrows). The two polarons represent two different polarization of the charge carrier cloud and the effect this polarization on the atomic equilibrium positions shifts [35].

2.2.1 Polaron formation and types

The term Polaron is often used to describe the charge carrier together with the atoms for which the carrier altered their equilibrium positions. However, this term is rather used in a more general sense to describe the charge carrier with the altered atomic motions in response to the carrier presence. The two previous situations led to classifying the polarons into two main types, a weak-coupling polaron and a strong-coupling polaron. The weak-coupling polaron condition describes a carrier which is not self-trapped while the strong-polaron condition describes a self-trapped carrier.

The weak-coupling situation occurs when the interaction between the carrier and the atoms is weak enough to be overcome with the characteristic phonon energy. However, the carrier's presence will still affect the vibrational frequencies of the atoms and correspondingly the atoms will affect the carrier motion changing its effective mass. Indeed, the weak-coupling polaron effective mass is slightly larger than that of the bare electronic carrier. On the other hand, the strong coupling polaron is formed when the carrier's binding energy is larger than the characteristic phonon energy, then the carrier will see the potential well it created as nearly static and we can call the carrier as self-trapped. In this case, the strong coupling polaron's effective mass is extremely larger than that of the bare electronic carrier.

The binding energy of a weak coupling polaron is mainly due to the carrier-induced softening. Carrier-induced softening is the decrease in the carrier's energy in response to the carrier's effect on the vibrational frequencies of the atoms. For the strong coupling polaron, the investigation of its self-trapping, when done under the adiabatic limit, shows that it is a nonlinear phenomenon. The adiabatic approach takes into account that the charge carrier shifts the equilibrium positions of the atoms and alter the stiffness constants that define the atoms' harmonic motions, but the atomic masses are infinite while the deformation stiffness constant remains finite. Thus, in the adiabatic limit, the atomic vibrations are suppressed. The nonlinearity comes from the dependence of the self-trapping potential on the wavefunction of the self-trapped carrier which is affected by the change in the self-trapping potential itself. Indeed, the nature of the interaction between the carrier and the surrounding atoms determine the state of the self-trapped carrier.

The extension of the self-trapped state generally depends on the carrier's electron-phonon interactions. Two types of interaction are present in this case, long-range electron-phonon interaction and short-range electron-phonon interaction. These interactions are responsible for the carrier induced shift of the atoms' vibrational frequencies and equilibrium positions and both effects change the coupled system's free energy. With just the long-range electron-phonon interaction the self-trapped carrier's radius in a typical polar solid where the long-range electron-phonon interactions are usually strong is of the order of few angstroms. In this case, we can call this a large polaron. On the other hand, the self-trapped carrier with only short-range electron-phonon interactions results in an infinitesimally small radius which in a real material will be confined to the smallest possible unit, an atom or a chemical bond. In this case, the polaron is called a small polaron.
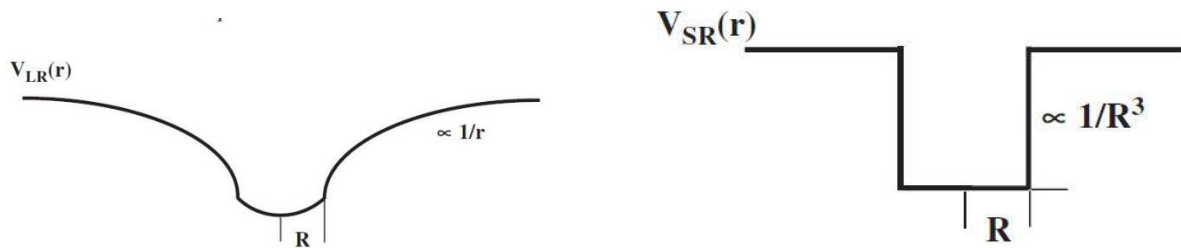
Fig. 2.4 Large and small polarons potential wells. (left) The large polaron's potential well resulting from the long-range electron-phonon interactions where the well depth is proportional to the inverse of the carrier's radius. (Right) The small polaron's potential well resulting from the short-range electron-phonon interactions where the well depth is proportional to the inverse of the cube of the carrier's radius [35].

In Fig. 2.4 the large and small polarons' potential wells are represented with the relation between the potential well depth and the charge carrier special extent radius. Generally, the larger the radius, the shallower the potential well; however, the time which the charge carrier spends on one site is an important factor determining the potential well depth. The longer the time the carrier spend on one site, the deeper the well gets and eventually a large polaron can collapse to a small polaron which happens in the case where both long and short electron-phonon interactions are present. We can think of the carrier and the surrounding medium as an object moving in a sand sea, the longer this object stays at one place, the deeper it gets in the sand which increases the difficulty of its motion. The shape and the size of this object play an important role in the depth of its immersion in the sand sea. The same way the radius of the charge carrier and the polarization state of this carrier play an important role in the shape and depth of the potential well this carrier creates. This analogy makes it easier to understand the role of defects and disorder in confining the charge carrier special extent. Defects in the material indeed can pin the charge carrier which gives the polaron enough time to collapse to the smallest possible unit while disorders can cause severe confinement to the carrier decreasing its radius. The effect of the type of electron-phonon interaction on the potential well shape and depth is pronounced. From the schematic graph, we can see that the long-range electron-phonon interaction changes the shape of the potential well to more smooth borders while the short-range electron-phonon interaction produces a very steep potential well. The depth of the potential well dependence on the carrier's radius is also different depending on the type of interaction. For the long-range electron-phonon interaction the potential well depth is proportional to the inverse of the charge carrier's radius while for the short-range electron-phonon interaction the well depth is proportional to the inverse of the cube of the carrier's radius [35]. This difference in the relation according to the difference in the type of interaction is another form of nonlinearity of the self-trapping process.

The large polaron's long radius allows it to extend over more than one structural unit. Therefore, it moves with a coherence length which is longer than the characteristic site to site separation. The large effective mass of that polaron along with its long coherence length allow it to move while weakly scattered by phonons. Indeed, the very large effective mass of the large polaron causes the polaron to move slowly but at the same time makes it difficult for weak dispersion phonons to cause any significant scattering. Thus, this kind of polarons gets scattered only by strong dispersion phonons and shows mobility which falls with increasing temperature. The mobility of this type of polarons is typically larger than 1 cm^2/Vs. The long coherence length of the large polaron satisfies the condition of the strong coupling polaron coherence motion. Strong-coupling polaron's motion is coherent if the carrier transfer energy between two adjacent sites is greater than the changes occur to the self-trapped energy in response to the classical movement of the atoms which itself enables the carrier transfer. Accordingly, the large polaron's motion is to be considered coherent.

An energy condition must be satisfied for the charge carrier in a small polaron to be confined to a single site. The small polaron is only stapled if the carrier transfer energy is much smaller than the self-trapping energy in such a way that the classical movement of the atom's modulation to the self-trapping potential is negligible to the confining potential. The condition for the small polaron's stability opposes the condition for the coherent strong coupling polaron's motion. Thus, the small polaron's motion is incoherent. Indeed, the small polaron motion is in the form of occasionally phonon-assisted hops with very low mobility typically much lower than 1 cm^2/Vs. In this type of polarons, the mobility increases with increasing temperature as the density of the phonons increase.
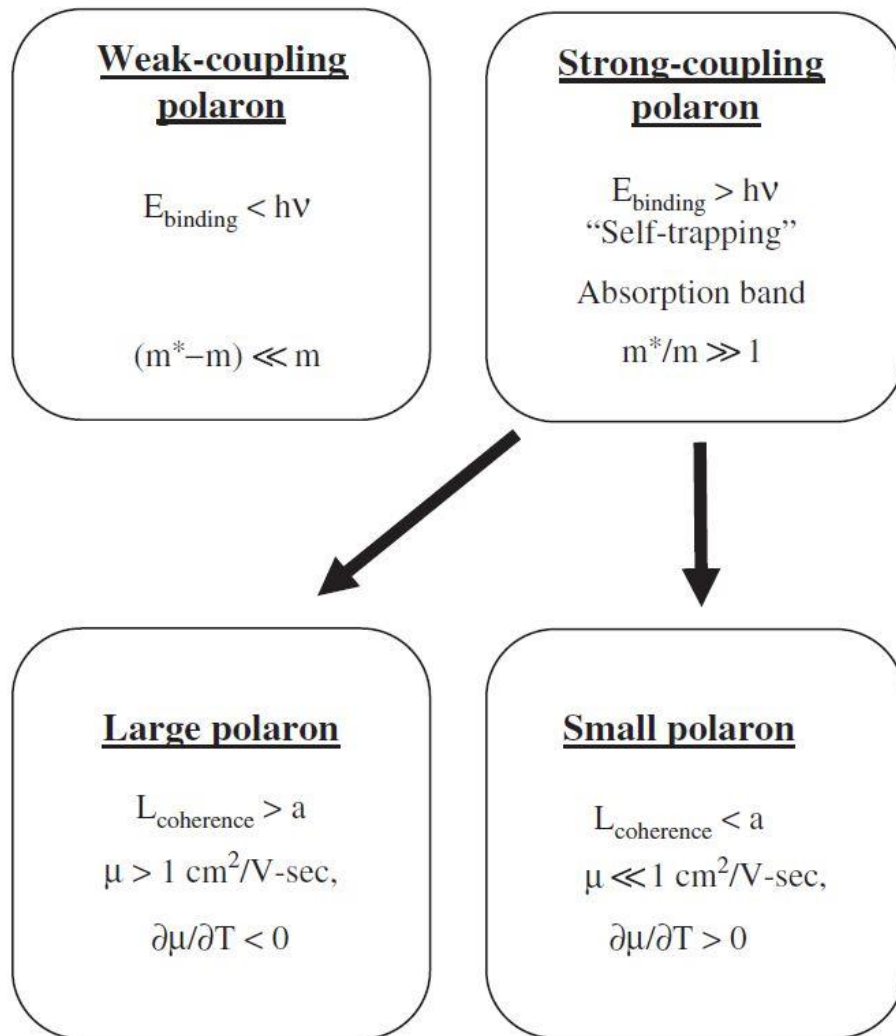
Fig. 2.5 The tree of polaron types. a is the site to site separation distance. [35]

Fig. 2.5 summaries what was demonstrated showing the three types of polarons with the condition of formation of each type. Three types of polarons can be distinguished depending on the interaction of the charge carrier with the surrounding medium. When the charge carrier modulates the vibrational frequencies of the surrounding atoms without changing their equilibrium positions, we have the weak-coupling polaron. This situation happens when the carrier only interacts weakly with the atoms via long-range electron-phonon interaction. When the interaction between the carrier and the atoms leads to a shift in the equilibrium position of the atoms along with their vibrational frequencies, we have the strong-coupling polaron. In this case, we call the carrier as self-trapped. According to the type of the electron-phonon interaction the strong-coupling polaron can be classified into two types of polarons. For relatively strong long-range electron-phonon interaction, the carrier's special extent will be longer than the site to site separation distance. In this case, the polaron type is large polaron and its carrier is delocalized over several structural units. When the short-range electron-phonon interaction is relatively strong, the charge carrier will collapse to the smallest possible structural unit and the polaron type, in this case, is small polaron.

2.2.2 Molecular Polarons

The molecular polaron is the polaron which its self-trapped charge carrier is confined to a single molecule. This situation happens in molecular solids when the small molecular orbitals overlap between the molecules results in narrow electronic energy bands which hinder the carriers intermolecular motion forcing its confinement on a single molecule.

Generally, three types of molecular orbitals can be envisioned according to the degree of the charge carrier confinement within the single molecule. If the carrier is delocalized over the whole molecule, then we have a polaron equivalent to the previously discussed weak coupling polaron. A smaller polaron can be envisioned if the charge carrier is confined to a subset of equivalent structural units such as a ring or a chain of atoms and in this case, this polaron can be equivalent to the strong coupling large polaron previously discussed. The smallest molecular polaron that is formed is when the carrier collapses to the smallest structural possible unit such as an atom or a chemical bond and this is equivalent to the strong coupling small polaron case.

A scaling analysis was proposed by Emin et al. [36] in order to identify the type of molecular polaron. This method is to find the adiabatic potential energy minima for a charge carrier in a deformable molecule in a medium with polar molecules.

$$E(L) = \frac{T_e}{L^2} - \frac{V_s}{L^d} - \frac{V_l}{L} \quad (2.5)$$

In equation (2.5), the adiabatic potential energy is represented as a function of a dimensionless scaling factor defining the polaronic charge carrier extent. Three terms contribute to the total energy of the system. The first term is the carrier kinetic energy term, the second corresponds to the short-range electron-phonon interaction potential energy term and the third is corresponding to the long-range electron-phonon interaction potential energy term and d is the dimensionality of the expansion of the charge carrier. The carrier's kinetic energy term drives the carrier to extend over the whole molecule while the electron-phonon interactions terms induce carrier confinement. In this context, the short-range electron-phonon interaction describes the interaction between the carrier and the motion of the atoms of the same molecule. On the other hand, the long-range electron-phonon interaction describes the dependence of the carrier potential energy on the movements of the polar molecules of the surrounding medium and it is called the Frohlich electron-phonon interaction [36].

The solution for the previous equation is represented in Fig. 2.6 as a function of the scaling factor L. As expected, by varying the magnitude of the three terms we get three different solutions where the minimum for each solution is different from the other. Each minimum in each solution is corresponding to one of the envisioned types of molecular polarons. For very high carrier's kinetic energy the electron-phonon interactions terms become negligible and we get a solution corresponding to free energy which is decreasing with increasing L. This solution is represented by the curve (a) where the minimum is indeed at the maximum possible L (L_m). When the long-range electron-phonon interaction is strong enough to balance the kinetic energy term we get a solution with a minimum which is in between the two extreme sides, in the middle between the delocalization over the whole molecule and the collapse to a single structural unit. This solution corresponds to a polaron which its charge carrier is occupying a subset of equivalent structural units within the molecule and is represented by the curve (b). When the carrier's kinetic energy is relatively low, the electron-phonon interactions terms dominate over the kinetic energy term in equation (2.5). The solution, in this case, is free energy which decreases with decreasing L. Thus, the minimum is at the smallest possible L (L_c) which is corresponding to a polaron's carrier that is collapsed to the smallest possible structural unit. This solution is represented by the curve (c).
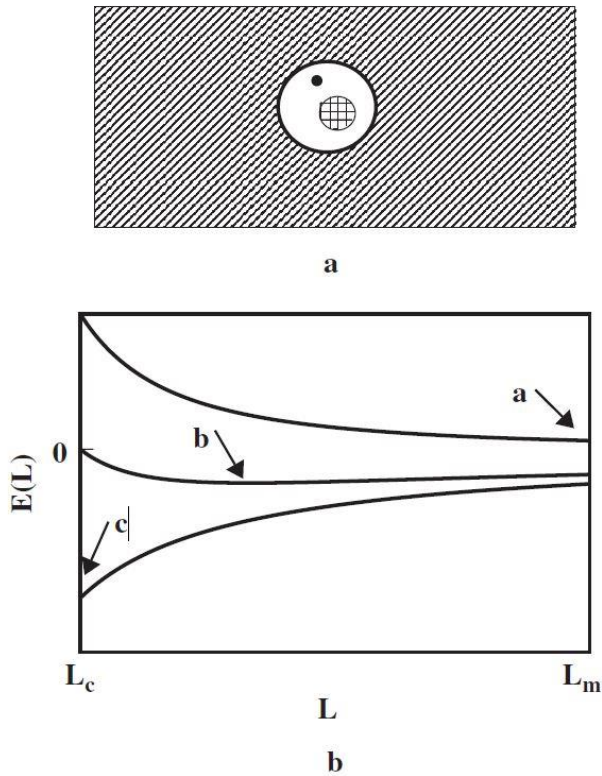
Fig. 2.6 Solutions for the polaron free energy as a function of the scaling factor L with a schematic drawing of the three solutions on top. The diagonal hatched big square represents the surrounding medium. The white circle represents the solution (a) of a polaron occupying all the molecule with its minimum energy at L_m. The square hatched area represents the solution (b) a polaron occupying a subset of equivalent structural units within the molecule with an energy minimum at an intermediate distance between L_m and the smallest possible structural unit (L_c). The dot represents the solution (c) corresponding to a polaron which is collapsed to the smallest possible structural unit as the energy minimum is located at L_c. [36]

As previously demonstrated, polaron formation is associated with carrier induced shifts of atomic vibrations and equilibrium positions. This effect is magnified in the case of molecular polarons. Indeed, for molecular polarons carrier induced shift of molecular vibrations is relatively large as the extent of the carrier state is of the size of the molecule. However, this effect is more pronounced in intermediate size polarons, since their carriers are the most polarizable because they are neither constrained by the molecule dimensions nor by the carrier's collapse to the smallest unit.

2.2.3 Polaron transport

Weak coupling polarons transport can be treated as a band like transport where the carriers move freely and exhibit occasional scattering events. The mobility, in this case, depends on the polaron effective mass and the characteristic time between two successful scattering events according to this relation:

$$\mu = \frac{et_s}{m^*} \quad (2.6)$$

where e is the charge of the electron, t_s is the time between two successful scattering events and m^* is the effective mass. The effective mass of the polaron increases with increasing the strength of the long-range electron-phonon interaction and the polaron mobility decreases. The scattering probability increases with increasing the temperature leading to a decrease in the time between two successful scattering events which decreases the mobility of the polaron. This type of transport is not believed to be of a major effect in organic semiconductors conduction. However, in some highly pure single crystals conduction measurements, evidence of band-like transport was detected like in the case of rubrene [37] and TIPS-pentacene [38]. This

transport mechanism is characterized with relatively high electron mobilities (more than 10 cm^2/Vs) which are inversely proportional with temperature.

Large polaron moves coherently as previously demonstrated and, for the condition of coherent movement to be fulfilled, the distance between two scattering events must be less than the carrier's special extent. Thus, we can set the carrier diameter in the case of large polaron as the minimum distance between two scattering events and this would lead to very high mobility if the mass of the carrier was the mass of the free electron. However, since large polaron's effective mass is much higher than that of the free electron, the mobility, in this case, is much less. This large effective mass makes it difficult for low momentum phonons to cause any significant scattering and the time between two successful scattering events, in this case, is greatly elongated. This proportionality between the effective mass and the scattering characteristic time leads to mobility which is independent of the effective mass to a good approximation. Indeed, one-dimensional large polaron mobility can be approximated by the following relation:

$$\mu_{LP} \approx \frac{ec_sL}{\kappa T} \quad (2.7)$$

where c_s is the sound velocity in the material, L is the large polaron length and κ is the Boltzmann constant. We can see that for high sound velocity materials the mobility increases. This proportionality is related to the phonons' momenta in material as that high velocity acoustic phonons move with low momenta and can only weakly scatter charge carriers. However, in the case of the temperature dependence, the situation is more complex than the simple negative dependence in this equation. When temperature increases the density of phonons increases as well and that is what is shown in the previous relation. However, there are two other important effects for increasing temperature. By increasing temperature, the disorder increases and the large polaron length decreases. On the contrary, with increasing temperature, the momenta of the phonons decrease which makes it less able to cause significant scattering to the polarons. However, regardless of this complex dependence of the mobility on temperature, large polaron's mobility generally decreases with increasing temperature.

Small polaron hopping is the most complex transport process out of the three polaron types. As previously demonstrated small polaron motion is incoherent. Since the small polaron's charge carrier is confined to one atom or chemical bond, it only can move if the atom moved. Thus, small polaron movement is induced by phonons and their mobility increase with increasing temperature.

In Fig. 2.7 a schematic illustration of the small polaron hopping process is shown. In the lower subpanels, the molecular configurations and the effect of the charge carrier (circle dot) on it are represented. In the upper subpanels, the carrier's self-trapping potential well caused by molecular deformation in response to the carrier presence is represented. The left panels represent the situation before the tunneling process while the right panels represent it after the carrier's tunneling. The arrows between the two panels represent the tunneling process and the arrows' sizes represent the probability of each process. As the temperature increases, the degree of equivalence between the two sites increases which increase the tunneling probability. This behavior is represented by the three cases (a), (b) and (c) with increasing tunneling probability going from (a) to (c). This representation, however, is not particularly accurate. The hopping process, in fact, practically only occurs when the two sites are almost equivalent as illustrated by the case (c). Thus, small polaron transport is mainly governed by two factors; how often the atomic vibrations offer the chance for the hopping process and how probably the carrier will take this chance and perform the hop. The density of the hopping opportunities offered by the atoms increases with temperature while the hopping probability increases with increasing the carrier's transfer integral. Based on the ability of the charge carriers to take the opportunities offered by the atoms to hop, two types of small polarons transfer regimes can be identified; adiabatic transfer and non-adiabatic transfer. In the adiabatic transfer regime, carriers envisioned to take every hopping opportunity

which is offered by the atoms while in the non-adiabatic transfer, carriers rarely take hopping opportunities and thus show relatively lower mobilities.

Fig. 2.7 A schematic illustration of the small polaron hopping process. Atomic vibrations modify the self-trapped carrier potential well depth which allows the carrier to tunnel to the nearest equivalent site. The tunneling process probability depends on the degree of equivalence between the two sites. Processes (a), (b) and (c) represent three different cases with three different tunneling probabilities.

When the polarons density is high enough to fill most of the space, the hopping distances is just a few times longer than the carriers' radii. In this case, the transfer integrals of the carriers are usually larger than the phonons energies which the carriers interact with and the polaron transfer is adiabatic. In other words, the transfer integral of the carrier is larger than the polarons binding energy or the reorganization energy. On the other hand, when the hopping distances are much larger than the carriers' radii, the transfer integrals are usually smaller than the phonons energies which the carriers interact with and the transfer is non-adiabatic. In this case, the transfer integral of the carrier is lower than the polarons binding energy or the reorganization energy. The transfer integral, the reorganization energy and the temperature affect the electronic transfer rate according to the following equation:

$$K_{ET} = \frac{4\pi^2}{h} \frac{1}{\sqrt{4\pi\lambda\kappa T}} \tau^2 e^{\left(-\frac{\lambda}{4\kappa T}\right)} \quad (2.8)$$

where h is the Blank constant, λ is the reorganization energy and τ is the transfer integral [39]. Again, the temperature dependence is more complex than what is shown in equation (2.8) as the temperature affects both the polaron's binding energy and the transfer integral.

When it comes to organic semiconductors, there are different explanations for the conduction mechanisms and up to now, there is no clear picture of a unified rule. Most of the times more than one mechanism are involved which makes the interpretation very difficult. However, in this subsection, I have reviewed the basic physics concerning charge carriers and transport in semiconductors generally and molecular semiconductors particularly which can be applied to organic semiconductors as well. Paring in mind that in one organic semiconductor charge carriers can take different forms of the previously demonstrated polarons. Depending on different external parameters, carriers can go back and forth from one polaronic state to another which exponentially increase the difficulty of describing a transport mechanism in one semiconductor material.

2.3   Organic Field Effect Transistors

Field effect transistors are three terminal devices (source, drain and gate) which use a vertical voltage applied between the source and the gate to modulate the current flowing between the source and the drain. They are known for their high signal-to-noise ratio and their low energy consumption. Organic semiconductors entered in the field of field effect transistors thanks to their practical advantages over inorganic semiconductors. These advantages include large area low-cost fabrication, flexibility, light-weight and the ability of functionalization in order to tune their properties. The first organic field effect transistor has been fabricated at the end of the 80s and, since then, progress in this field has been rapidly growing. Organic field effect transistors are not only showing growing importance in modern technology but they represent a valuable tool for studying organic semiconductors from the point of view of fundamental physical properties, like charge transport mechanisms and structural-property relationship.

A schematic drawing of a typical field effect transistor is present in Fig. 2.8 where the main device components are shown. The device at its simplest form consists of five main components; source and drain electrodes, organic semiconductor active medium, a dielectric insulator layer and a gate. The current flows between the source and drain electrodes upon applying a drain voltage while the source electrode is usually grounded. This current is modulated upon applying a vertical voltage between the gate and the source which produces an electrical field between the source and the dielectric insulator. This electric field induces charge injection from the source and drain electrodes, hence forming the conduction channel at the semiconductor/dielectric interface. By applying a gate voltage, the charge density in the conduction channel increases which leads to an increase in the source-drain current as well.
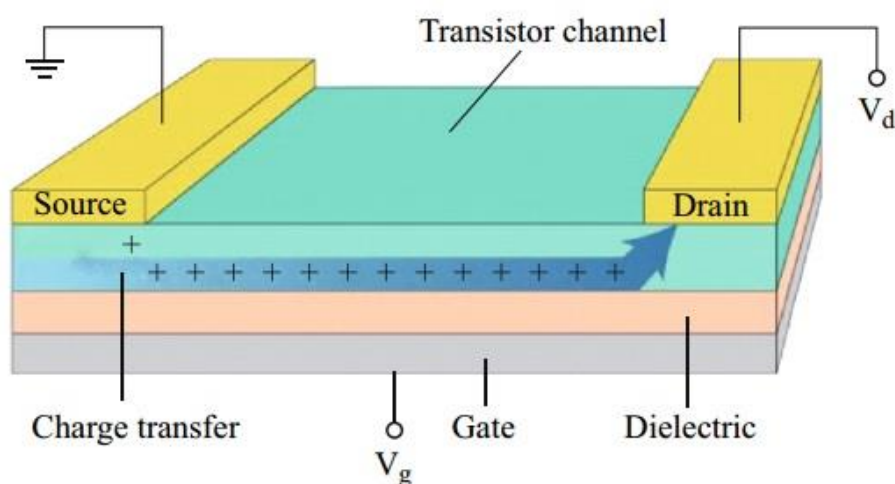
Fig. 2.8 Schematic drawing of a typical organic field effect transistor

2.3.1 Device architecture

Organic field effect transistors possess four different configurations in basis on its components' arrangement. In Fig. 2.9 the four possible configurations of the organic field effect transistors are represented. In panel (a) the top gate/top contact (TG/TC) configuration is shown. In this configuration, the semiconductor is first deposited on a substrate then the source and drain electrodes are deposited on top of it followed by the dielectric then the gate electrode. In panel (b) the top gate/bottom contact (TG/BC) is shown. In this configuration, the source and the drain electrodes are firstly deposited on a substrate then the semiconductor followed by the dielectric insulator layer then the gate electrode. In panel (c) the bottom gate/top contact (BG/TC) configuration is shown. In this configuration, the gate electrode is firstly deposited, then the dielectric insulator layer followed by the semiconductor and finally the source and drain electrodes. In panel (d) the bottom gate/bottom contact (BG/BC) configuration is shown. In this configuration, the gate electrode is firstly deposited then the dielectric insulator layer followed by the source and drain electrodes and finally the semiconductor material.
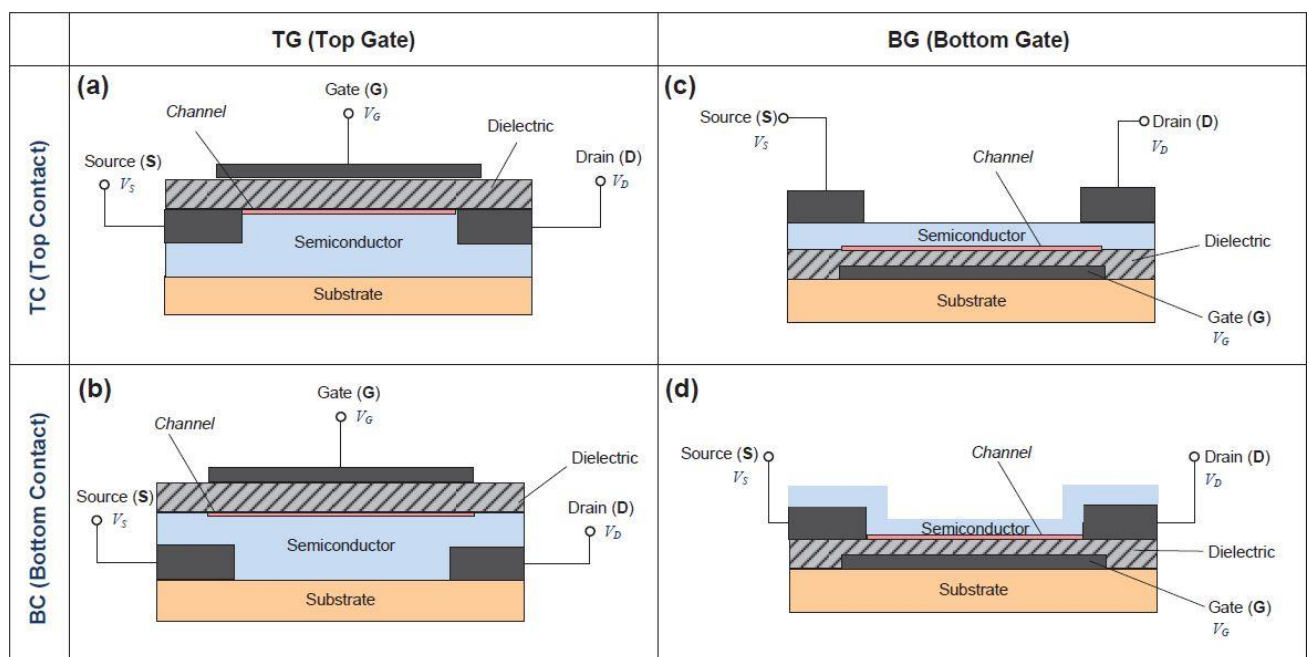
Fig. 2.9 Four configurations of organic field effect transistors [34].

The top gate configurations are generally more selective in terms of the choice of materials. Since the dielectric insulator layer in these configurations must be deposited on top of the semiconductor layer, some technical considerations must be considered. The main issue in this scenario is the ability of the semiconductor to sustain whatever deposition technique which shall be used for depositing the dielectric layer. This selectivity put constrains on the semiconductor and the dielectric choices. Another issue, which generally appears when choosing the top gate configuration, is that the off current of the device is generally higher in comparison to the bottom gate configuration. This can be due to oxygen doping that can occur when some oxygen molecules get accumulated between the dielectric and the semiconductor interface during the deposition process. An important consideration when applying the gate electrode is to make sure that the gate covers all the distance between the source and the drain electrodes; otherwise, there will be a high resistance area which is not affected by the gate and the total resistance of the device will increase.

When it comes to the choice of the source and drain contacts position generally the bottom contact configuration is favorable in terms of manufacturing complexity. However, bottom contact's devices usually exhibit higher contact resistance. This behavior can be attributed to the disturbance which is caused by the electrodes to the semiconductor material uniformity. When the semiconductor is deposited, the area of the

interface between the contacts and the semiconductor exhibits a more disordered morphology which arises from the contacts disturbance. This disordered area increases the traps density at the contacts/semiconductor interfaces which increase the difficulty of charge injection from the contacts leading to a decrease in the device performance in general.

An example of the effect of the bottom contacts on the semiconductor grain size is shown in Fig. 2.10, where on the left panel (a) a schematic drawing of the molecules at the interface area and on the right panel (b) a scanning electron microscope image of the contact/semiconductor interface area is shown. From the image, the grain size of the pentacene in contact with the gold electrode is smaller than the grain size in the region away from the electrodes. However, this is true for some cases especially for high crystalline small molecules but in general, a bottom gate/bottom contact configuration can be more convenient for crystalline materials as PH3 in which it would be complicated to make a good top interface.
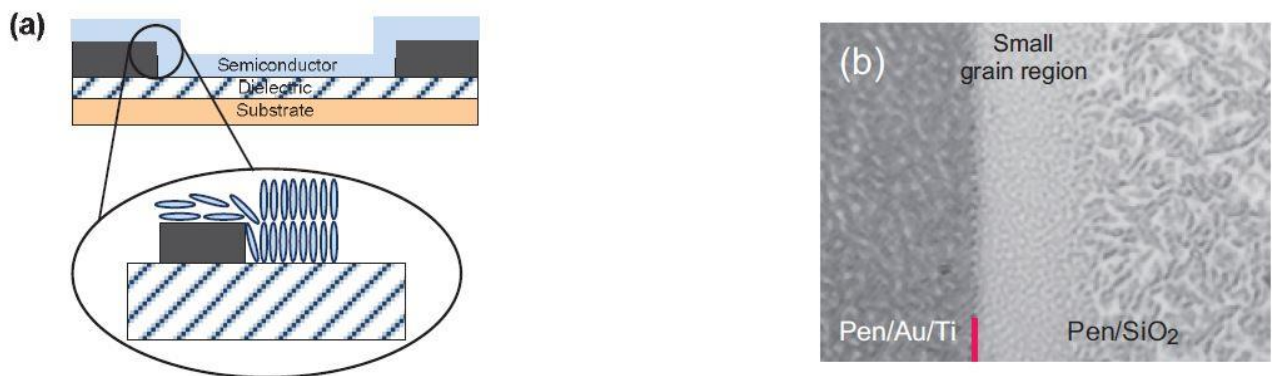
Fig. 2.10 contact/semiconductor interface between gold electrode and pentacene as a semiconductor showing effect on grain size. (a) schematic drawing of the deposited molecule, (b) scanning electron microscope image of the interface [40].

Regarding the relative position of the source and drain electrodes to the gate, the four configurations show two possibilities. When the source and drain electrodes are on the same side of the gate with respect to the semiconductor layer, we have what so-called the coplanar configuration. On the other hand, if the source and drain electrodes were on the opposite side of the gate, then we have the staggered configuration. In the staggered configuration, the charges must cross the low conductivity bulk area of the semiconductor to reach the semiconductor/dielectric interface which increases the charge injection difficulty of the device. In the coplanar configuration, the charges will not have to cross that high resistance semiconductor bulk but the charge injection area will be confined to the conduction channel depth since the charge injection, in this case, is only lateral.

2.3.2 Operation regimes

In organic field effect transistors, the organic semiconductor is generally of low conductivity when it is in its intrinsic form and by applying the gate voltage charges start to accumulate at the semiconductor/dielectric interface leading to an increase in the current. This working mode is called the accumulation regime where, by applying the gate voltage, we have the on high current and, when no gate voltage is applied, we have the off low current. In this mode, the gate and the drain voltages are of the same sign. For p-type devices both the gate and the drain voltages are negative and the charge carriers are holes while for n-type devices both the gate and the drain voltages are positive and the charge carriers are electrons.

Usually, two types of electrical characteristics are measured on a transistor: the output curve (Fig. 2.11a) and the transfer curve (Fig. 2.11b). The output curve shows the results of measuring the drain current as a function of the drain voltage while the gate voltage is constant for each sweep. However, the gate voltage is increased in a stepwise starting from zero to the maximum value, one step per sweep. The transfer characteristic curve

shows two sweeps between the drain current and the gate voltage where the first sweep is done at constant low drain voltage while the second sweep is done at constant high drain voltage.

The drain voltage is responsible for the charge movement from the source to the drain; hence it is of a direct effect on the charge distribution along the conduction channel. Based on the drain voltage there are two distinct regimes the device operates at, the linear regime and the saturation regime.

When the drain voltage is low, the charge distribution in the conduction channel is nearly uniform, then the device work as a resistor whose current is controlled by the gate voltage and in this case the drain current/gate voltage relation is linear and it follows this relation:

$$I_{Dl} = \frac{W}{L} \mu C_i (V_G - V_T - \frac{V_D}{2}) V_D \quad (2.9)$$

where W and L are the channel width and length, respectively and C_i is the unit area capacitance of the gate dielectric.

When the drain voltage further increases, the uniformity of charges in the conduction channel gradually disappears and the Coulombic interaction between charges starts to affect the effective drain voltage value at the drain electrode. At high drain voltage, the effective potential difference between the source and the drain saturates at a pinch-off value equal to the difference between the gate voltage and the threshold voltage. At this pinch-off point, the arriving charges number is no more dependent on the applied drain voltage, but instead, this number is now modulated by the gate voltage. Any further increase of the applied drain voltage will only move this pinch-off point from the drain side towards the source side and will not affect the current anymore. Thus, we can expect a square dependence of the drain current on the gate voltage and indeed the drain current in the saturation regime follows this relation:

$$I_{Ds} = \frac{W}{2L} \mu C_i (V_G - V_T)^2 \quad (2.10)$$
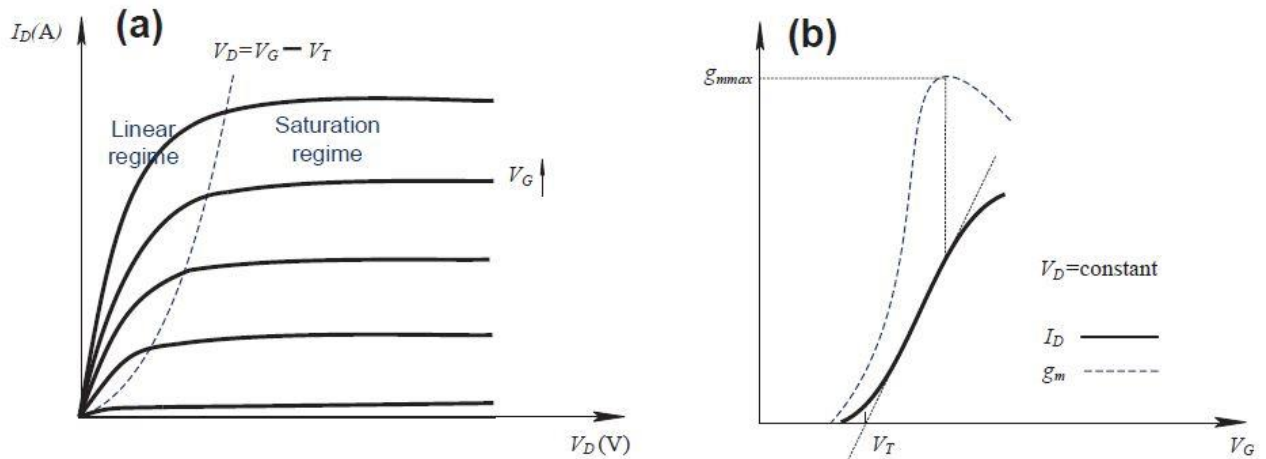
Fig. 2.11 (a) example of transistor output curve where V_D, V_G, V_T, are the drain voltage, gate voltage, threshold voltage respectively and I_D is the drain current. (b) Typical transfer characteristic curve in the linear regime where the drain voltage is kept constant at a low value and g_m is the transconductance [34].

2.3.3 Field effect mobility and parameters affecting device performance

The mobility of the charge carriers in the semiconductor is an intrinsic property of the material. However, the mobility which is measured in the organic field effect transistors is a macroscopic property of the device which its upper limit is the intrinsic mobility of the organic semiconductor. Indeed, there are several factors which affect the mobility of the device as the contacts resistance, the density of traps and defects in the material,

the semiconductor grain size, the dependence of mobility on the gate voltage and the dielectric/semiconductor interface effect on mobility. However, by optimizing the factors affecting the device performance, a field effect mobility as close as possible to the intrinsic organic semiconductor mobility can be achieved. It is worth mentioning that the organic semiconductor doping process was not mentioned as a good strategy for increasing device mobility. Indeed, doping can increase the overall mobility of the device but it usually increases the bulk conductivity which increases the off current of the device and decreases significantly its on/off current ratio. The latter is a second important parameter when it comes to transistors field (for practical applications the on/off ratio must be more than 10^6).

The device mobility is, in fact, the collective mobility which is the resultant of all different mechanisms and regions in the conduction channel. The different mobilities, corresponding to different areas in the device, collectively contribute to the final device mobility in such a way that the minimum mobility out of all dominates over the others acting as a bottleneck for the current. The collective mobility then follows this relation:

$$\frac{1}{\mu} = \frac{1}{\mu_1} + \frac{1}{\mu_2} + \frac{1}{\mu_3} + \cdots + \frac{1}{\mu_n} \quad (2.11)$$

representing different mobilities for different regions.
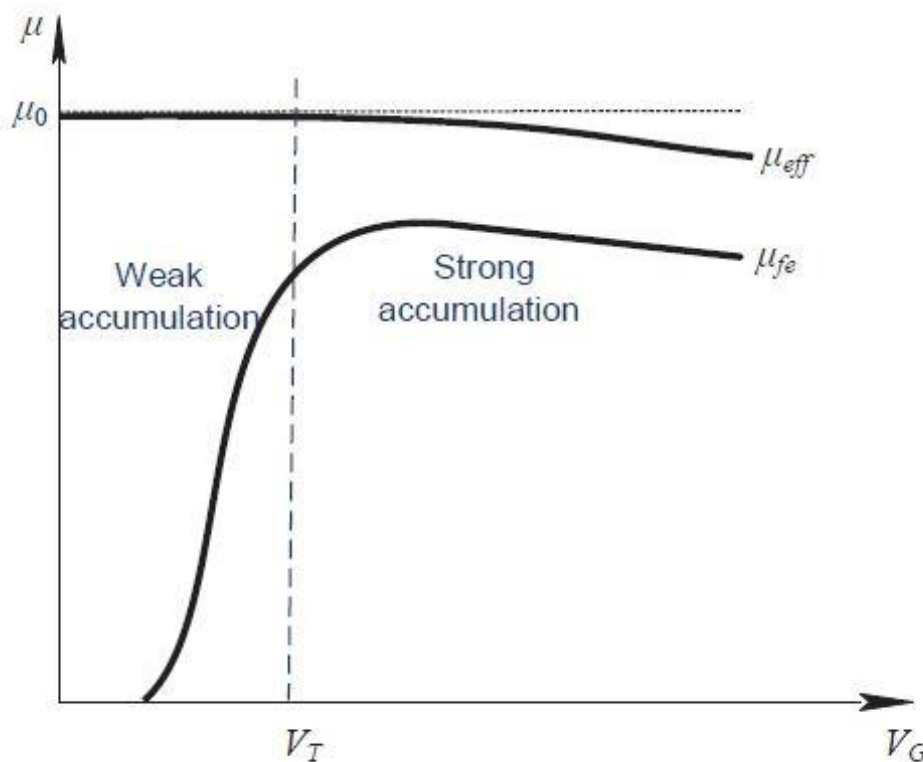
Fig. 2.12 Typical mobility dependence on the gate voltage. The upper curve represents the intrinsic mobility of the organic semiconductor while the lower curve represents the field effect mobility of the semiconductor in the device [34].

In Fig. 2.12 the mobility dependence on the gate voltage is represented with two curves. The upper curve represents the intrinsic mobility of the organic semiconductor while the lower curve represents the field effect mobility of the semiconductor in the device. The intrinsic organic semiconductor mobility as was demonstrated is always higher than the field effect mobility. However, both mobilities show a slight decrease with increasing the gate voltage to high values. This behavior is indeed expected for devices which are as close as possible to be ideal. At a high gate voltage, a high number of charges accumulate in the conduction channel.

This accumulation induces a Coulombic interaction between the charges which increases charge scattering and the overall mobility finally decreases. However, in many cases, the mobility increases with increasing the gate voltage which is considered a non-ideal behavior. The increase in mobility with the gate voltage can be attributed to two main reasons. The first possibility is that, with increasing the gate voltage, deeper traps are gradually filled; thus, the incoming new charges see only shallower traps, so they move with higher mobility. The second possibility is that by increasing the gate voltage, the energy barrier between the contacts Fermi level and the semiconductor conduction level (HOMO in p-type devices and LUMO in n-type devices) decreases. When the injection energy barrier decreases, the charges are efficiently injected into the semiconductor and the overall mobility of the device increases as well.

In Fig. 2.13 a schematic drawing of the effect of the gate voltage on the Fermi energy and the traps is shown. On the left (a) the state with a low gate voltage where the Fermi energy is still not high enough to fill the traps which lead to a high barrier for charges to overcome when hopping from site to site as indicated by the arrow. On the right (b) the state when the gate voltage increases, in this case, Fermi energy is nearly at the edge of the barrier and the traps are nearly filled. This situation facilitates the charges' movement and increases their overall mobility. This type of gate voltage dependence of mobility can be seen in the polycrystalline devices in comparison with large crystals devices. The polycrystalline devices usually show an enhancement of mobility with increasing the gate voltage but with the same type of semiconductor material, this dependence disappears for large crystals.

Apart from the mobility, another parameter which is important in field effect transistors is the threshold voltage. The threshold voltage is the voltage where the current starts to increase with the gate voltage. Ideally, for organic field effect transistors, the threshold voltage should be zero.
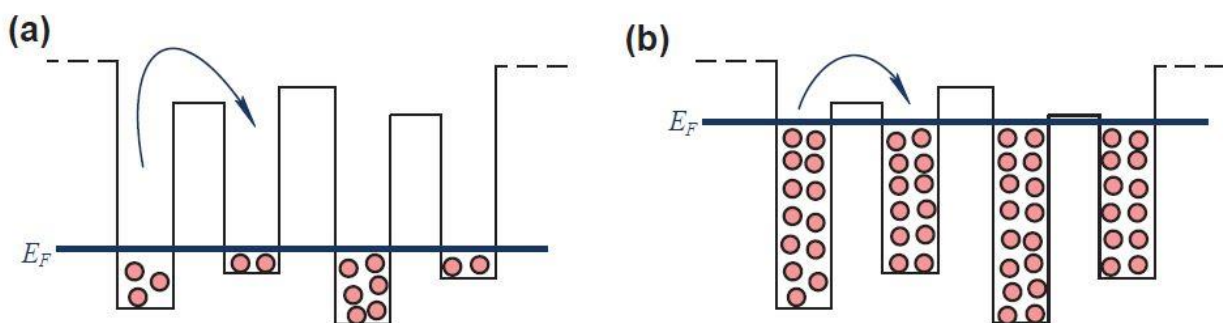
Fig. 2.13 Schematic drawing of the effect of the gate voltage on the Fermi energy and the traps. On the left (a) the state with a low gate voltage and on the right (b) the state when the gate voltage increases. The arrows indicate the direction of the charges (red circles) hops [34].

2.3.4   Traps and hysteresis

Hysteresis cycle in the transistor measurements is the difference in the current between the forward sweep and the backward sweep of the gate voltage. This difference can be attributed to the traps that are formed at a high gate voltage. At high gate voltages, the charge density in the conduction channel is high and the interactions between these charges increase which in the presence of a trapping factor lead to charge trapping. The hysteresis is represented by a shift in the threshold voltage which in the case of an ideal organic semiconductor should be zero. However, there are two main factors that can lead to the shift in the threshold voltage like traps in the semiconductor or contact's resistance. The effect of the gate voltage on the contact resistance was described in the previous subsection and with the same arguments, the shift of the threshold voltage can be explained. However, in the case of the hysteresis, the threshold voltage is different concerning the forward and the backward sweep of the gate voltage. To understand the origin of this difference one should analyze the dynamics of the measurement process. When the gate voltage is applied, and an electric

field is generated between the source electrode and the dielectric surface. When the gate voltage increases, this electric field strength increases accordingly. This electric field moves the system from its equilibrium state which forces the mobile charges in the material to move accordingly to regain the equilibrium state. The number of charges accumulated on the dielectric surface is then proportional to the electric field strength. By increasing the gate voltage gradually during the forward sweep, more mobile charges are accumulated on the dielectric surface. The drain voltage, in this case, move these accumulated mobile charges and we measure the drain current accordingly. If there are traps at the dielectric/semiconductor interface, those mobile charges fill these traps and they are no longer mobile. Let us imagine that upon increasing the gate voltage by ΔV_G then ΔN of charges accumulated on the interface. This ΔN and because the presence of traps is divided into ΔN_m mobile charges and ΔN_T trapped charges. By decreasing again the gate voltage with the same amount ΔV_G the same number of charges ΔN should leave the interface for the sake of equilibrium. However, only mobile charges N_m can move to leave the dielectric/semiconductor interface. Thus, the decrease in the current, in this case, will be proportional to $\Delta N + \Delta N_T$ while in the forward sweep the increase in the current was only proportional to ΔN_m.

The traps which are responsible for this phenomenon is mainly the traps present at the dielectric/semiconductor interface. These traps can be intrinsic traps in the material itself or traps due to the dielectric layer or traps resulting from the adhesion between the semiconductor and the dielectric. The traps are any reason which forces the carrier to collapse to a severely bound state. Examples of intrinsic traps that can be present in the semiconductor material itself can be impurities of defects which bin the charge carriers leading to their collapse, grain boundaries and disorder in the semiconductor which can confine the charge carrier special extent leading again to its collapse. High surface roughness and poor adhesion between the semiconductor and the dielectric material can be reasons for charge carrier's confinement and collapse. High dielectric constant materials are known to interact with the polarons in the semiconductor binning their charge carriers. SiO_2 is a widely used dielectric material. However, it is known to block n-type transport and create traps for p-type transport because of the dangling hydrogen atoms connected to the oxygen atoms on its surface [41].

2.3.5   Organic semiconductors and sp-carbon in field effect transistors

Organic semiconductor materials can be classified into two main categories: molecular materials and polymers. Small molecules usually show better devices' performances than polymeric materials. However, small molecules are generally less stable and more difficult to process than polymeric materials. In both categories, π-conjugation is a key element in the material performance in field effect transistors. By increasing the conjugation, the electronic overlap between molecules or macromolecules is believed to increase leading to an increase in the transfer integral. Besides increasing the conjugation, molecular packing and intermolecular distances are important factors influencing the transfer integral. Processability is an important factor which has an indirect effect on the device performance and reproducibility too.

Four possible molecular packing configurations are shown in Fig. 2.14. In panel (A) we can find the Herringbone packing (face-to-edge) without ππ-overlap which achieves the least ππ-overlap between molecules and hence expected to show the worst performance. Pentacene is known to take this packing configuration. In panel (B) herringbone packing with ππ-overlap between adjacent molecule is shown. This configuration is not perfect concerning the ππ-overlap; however, it is better than the previous configuration. Rubrene is a good example that takes this configuration. Another configuration is the lamellar motif, 1-D π-stacking which is shown in panel (C). In this configuration, the ππ-overlap is larger than the previous two configurations and hexyl-substituted naphthalenelene diimide is an example which takes this configuration. The pest configuration in terms of ππ-overlap is the lamellar motif, 2-D π-stacking shown in panel (D). TIPS-PEN is known to take this configuration.
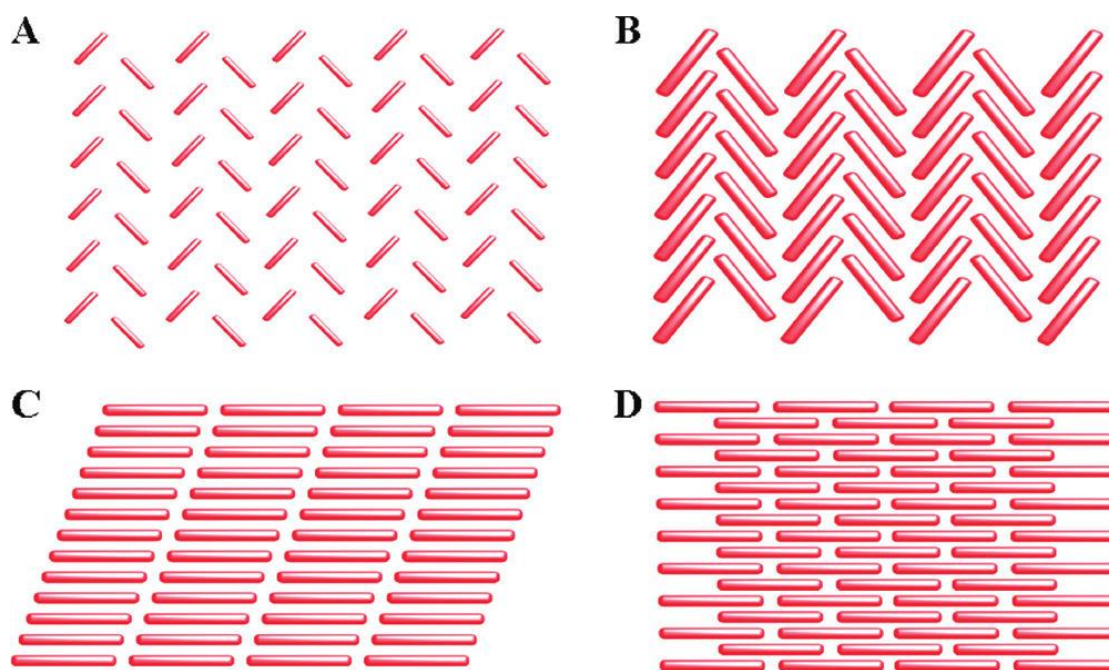
Fig. 2.14 four possible molecular packing configurations. (A) Herringbone packing (face-to-edge) without ππ-overlap. (B) herringbone packing with ππ-overlap between adjacent molecule. (C) lamellar motif, 1-D π-stacking (D) lamellar motif, 2-D π-stacking. [42]

Molecular design strategies most of the time aim to increase conjugation and improve packing. However, high conjugated materials usually show stability problems due to their narrow band gap. Rigid molecular backbone is one of the strategies to increase the conjugation as it prevents the rotation of different units in the molecule, leading to loss of conjugation. Rigid molecular backbones are also important for crystallinity due to the absence of free motion in the molecule. A drawback which accompanies the high crystallinity is the poor solubility which leads to difficulties in processing. A usual way to overcome the solubility problem is to add subunits to the side or the head of the backbone which act as a crystallinity hindering substitutions with little electronic effect on the conjugation for example. The substitutions are also used to force a different form of packing aiming for better ππ-overlap between molecules. Another way of using substitutions is to make use of the electronegativity of these substitutions where high electronegative substitutions act as an electron acceptor and decrease the HOMO and the LUMO energy while low electronegative substitutions act as electron donner and increase the HOMO and the LUMO energy levels of the molecule.

Pentacene and rubrene are among the most established organic molecules in the field of organic electronics. Pentacene with a band gap of 1.8 eV indeed, has shown the highest mobility which was recorded for organic semiconductors of 40 cm^2/Vs [43]. Although the band gap and the molecular packing are important parameters to be considered when designing organic molecules for electronics but the case of pentacene shows that they are not always the leading factors. For example, hexacene, which is more conjugated than pentacene, has a lower band gap of 1.4 eV, shows lower mobility of around 4 eV [44]. This situation is an example of how difficult it is to put a general rule when it comes to organic semiconductors. Indeed, research in this area is still in its early stages and due to the complexity of parameters and its large number, finding a general rule is a challenging issue.

R=t-Bu,
R=SiMe$_3$,
R=SiMe$_2$t-Bu,
R=Si(i-Pr)$_3$,
R=Si(C$_6$H$_{13}$)$_3$,
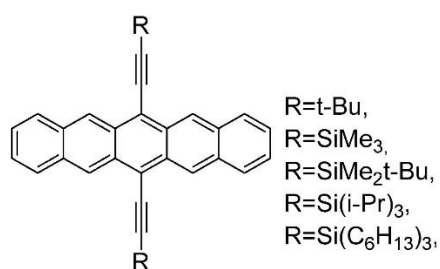
Fig. 2.15 pentacene with sp-carbon chains as subunits with different terminations [45].

Sp-carbon chains have never been investigated as semiconducting material in the field of field effect transistor. However, sp-carbon units are usually used as subunits for processability improvement or to force one form of molecular packing over the other but not as the main element in the molecule. An example of using sp-carbon chains as subunits to improve packing and stability is shown in Fig. 2.15. Indeed, this strategy led to changing from the Herringbone packing (face-to-edge) without ππ-overlap configuration obtained by pentacene to lamellar motif, 2-D π-stacking configuration, which an example of using substitutions to improve the molecular packing [45].

The molecules in Fig. 2.16 are an example of sp-carbon chains in the field of organic field effect transistors. In this work, it was shown that by introducing an electron donating group as in molecule 2 and 3 the transistor showed current modulation while for molecule 1 there were no working devices. The mobilities for molecules 1 and 2 were 0.3 and 3*10^{-4} cm^2/Vs respectively, which an example of using substitutions to modulate the energy levels of the molecule [46]. It is worth mentioning that the all sp-carbon structures which were investigated before, are usually short polyynic type chains and no cumulenic chains have ever been used before.
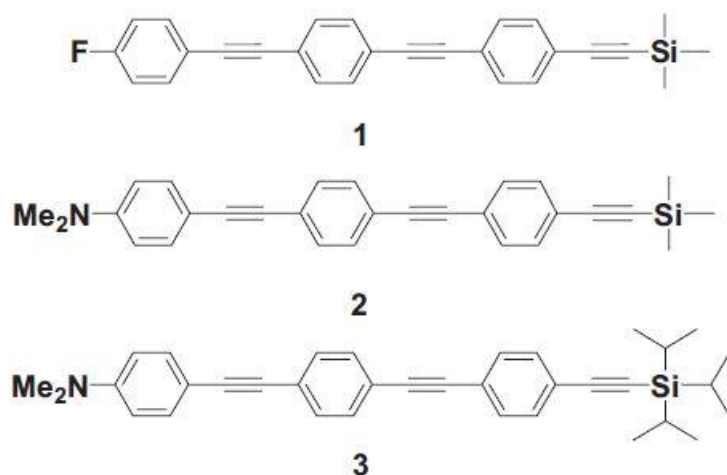
Fig. 2.16 molecules with sp-carbon chains as the main component [46].

3 Materials and methods

In this chapter, the investigated molecules in this work will be presented along with the protocols I used in preparing the samples, the characterization methods and procedures as well. The instruments used in the investigation process will be shown too.

3.1 Investigated molecules

Four molecules have been investigated in this work Ph5, Ph3, 1,2-Diphenylacetylene (DPA) and 1,4-Diphenylbutadiyne (DPB). Ph5 and Ph3 are two molecules synthesized by Tykwinski et al. shown in Fig. 3.1, while DPA and DPB are commercial molecules.

3.1.1 Cumulenic molecules
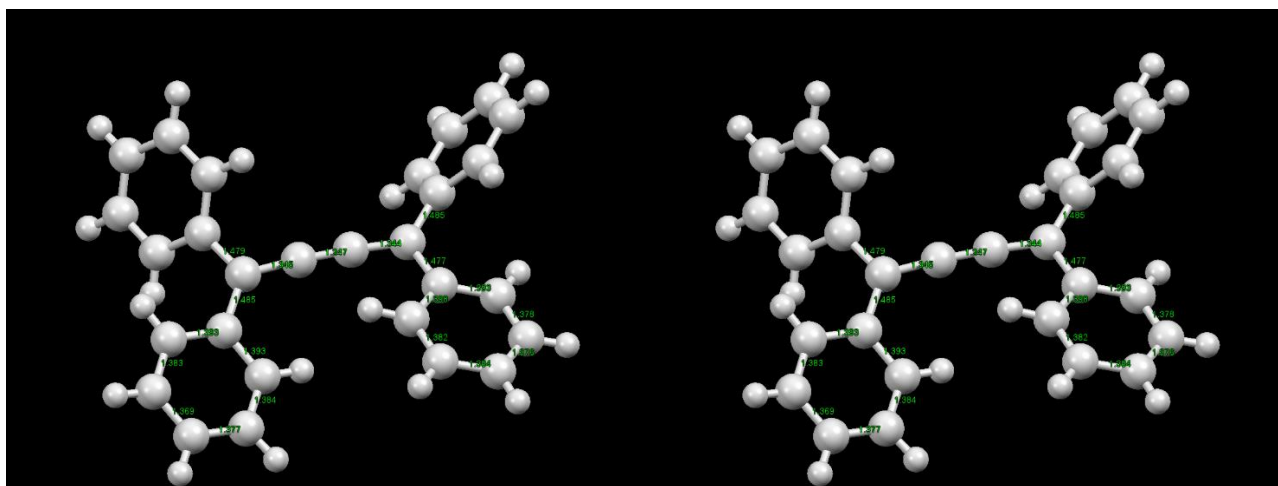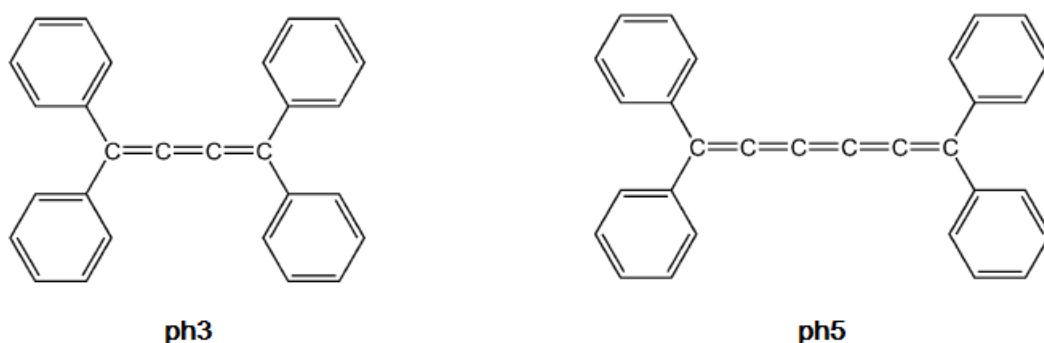
Fig. 3.1 Ph3 (left) and Ph5 (right) molecules. On top, the molecular structure is shown while in the bottom the XRD molecular structure and the bond lengths in A are shown (the XRD data were provided by the manufactural)

Ph3 and Ph5 molecules are composed of a chain of sp-carbon atoms connected with double bonds in a cumulenic configuration and terminated with two sp^2-carbon atoms, one on each side. The sp^2-carbon atoms are connected to two phenyl groups each. The connection to the two phenyl groups on each side is the reason for the cumulenic character in the chain. The chain in Ph3 is composed of four carbon atoms connected with three double bonds while in Ph5 the chain is composed of six carbon atoms connected with five double bonds (see Fig. 3.1). The name was chosen based on the structure where the Ph represents the presence of the phenyl groups terminations while the number that follows represents the number of the double bonds in the chain.

These molecules have been previously characterized in our laboratory in terms of their Raman spectra and their crystal formation when drop-casted on a surface. On the other hand, the XRD on the powder of the molecules and the UV-Vis spectrum in solution have been provided by the manufacturer.

3.1.2 Polyynic molecules

Fig. 3.2 1,2-Diphenylacetylene (DPA) (on the left) and 1,4- Diphenylbutadiyne (DPB) (on the right) molecules

DPA and DPB are composed of a chain of sp-carbon atoms connected with an alternation of a single and triple bonds terminated with two phenyl groups, one on each side. The chain of the DPA is composed of four carbon atoms while the chain in DPB is composed of six carbon atoms connected in a polyynic way (see Fig. 3.2). These molecules are known to form colorless crystals and are used as building blocks in organic synthesis. It is worth mentioning that the similarity between the molecules makes a good base for a comparative study.

3.2 Device fabrication and preparation

In this section, the device fabrication which I did in order to obtain my results will be explained. Bottom-gate bottom-contact prepatterned substrates have been used for the transistor fabrications. These substrates are commercially available from the Fraunhofer institute. The molecules have been deposited from solution using drop casting and spin coating methods. In some experiments, two types of self-assembled monolayers were used which I applied on the Fraunhofer substrates.

3.2.1 Substrate preparation

The Fraunhofer substrate is a premanufactured substrate designed especially for organic field effect transistors measurements. There are sixteen devices on the same substrate divided into four groups. Each group is composed of four devices having the same distances between the source and drain electrodes (channel lengths), 2.5, 5, 10 and 20 μm. The contacts are made in an interdigitated way where half the devices in the same group are aligned vertically and half are aligned horizontally. The contacts pads are 0.5 * 0.5 mm^2 and the channel width for all the devices is 10 mm while the whole substrate is 15 * 15 mm^2 (see Fig. 3.3).
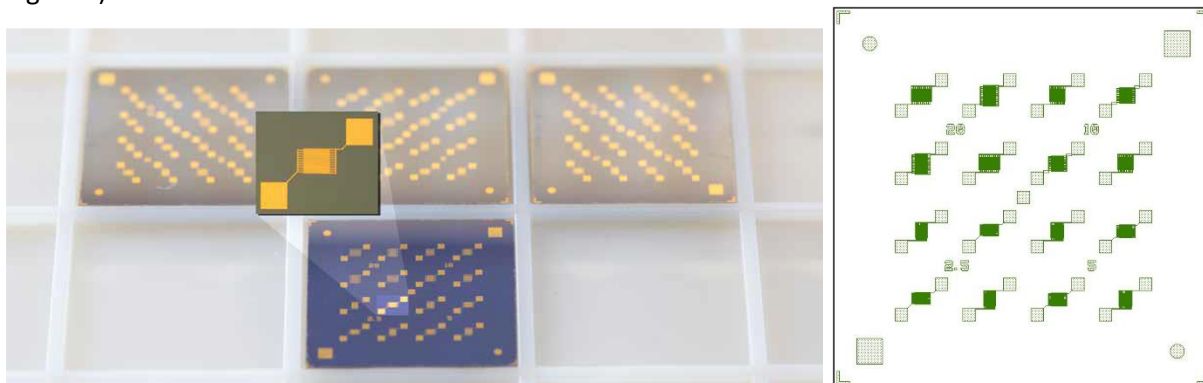
Fig. 3.3 Fraunhofer substrate. The number between every four devices is the distance between the source and the drain electrodes.

All the devices have a common gate and possess the configuration bottom gate/bottom contact (BG/BC). Each device is composed of gold source and drain electrodes of thickness 30 nm deposited on top of an adhesion layer of ITO of thickness 10 nm. The dielectric insulator is 230 nm layer of SO_2. The common gate is a Si wafer n-doped with a doping concentration of $3*10^{17}$ cm^{-3} (see Fig. 3.4).

Before depositing the molecules on the substrate, a specific cleaning protocol was followed. First, the substrate was rinsed with acetone then was emerged in acetone and left in an ultrasonic water bath for ten minutes. This step is necessary for removing a protection polymeric thin film which is deposited on the substrate by the manufacturer for protection reasons. After that, the substrate was rinsed with isopropanol then was emerged in isopropanol and left in another ultrasonic water bath for 10 minutes. The substrate is

then dried using a nitrogen flow to remove the isopropanol. This step is necessary to remove any left acetone on the substrate. After that and just before the molecules' deposition, the substrate was cleaned with oxygen plasma cleaning. The oxygen plasma cleaning is done by putting the substrate in a plasma generator which uses low pressure ionized oxygen to burn any left organic impurities on the substrate. After the cleaning process, the substrate is immediately used for molecules deposition.
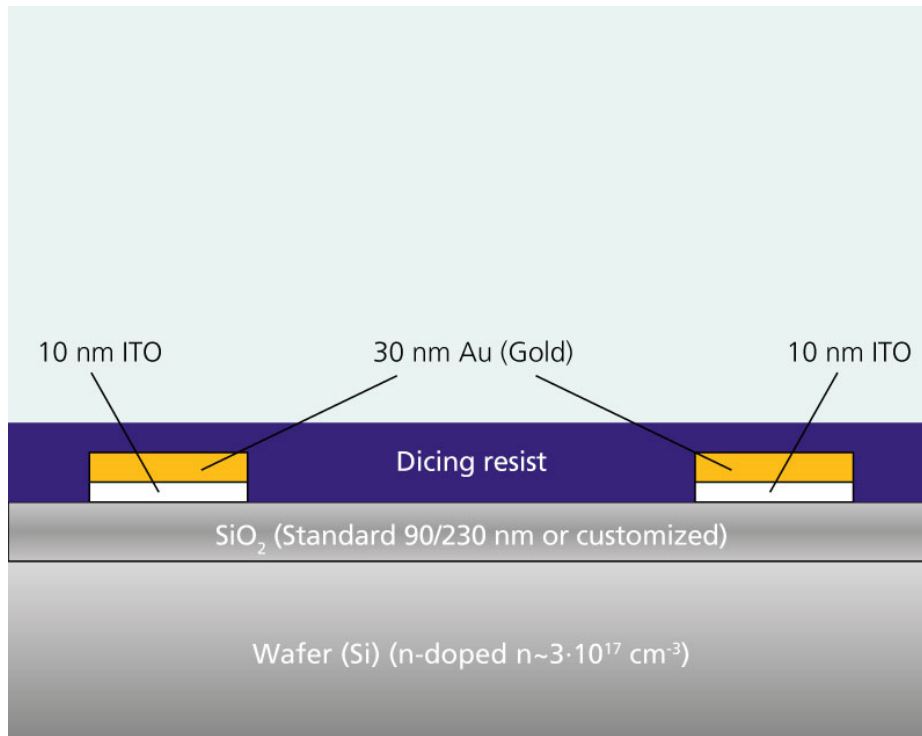
Fig. 3.4 Fraunhofer substrate device architecture and components.

3.2.2 Self-assembled monolayers' application

In this work, two self-assembled monolayers were used, octadecyltrichlorosilane (OTS) and pentafluorothiophenol (PFBT). The OTS was used to passivate the OH groups on the surface of the SO2 which are known to cause traps in the semiconductor. On the other hand, the PFBT was used to modulate the work function of the gold electrodes in order to decrease the injection barrier between the gold and the HOMO level of molecular crystals.

OTS is an alkyl chain terminated from one side with the functional group $SiCl_3$. This termination is responsible for the OTS attachment to the OH group on the surface of the silicon oxide. The Cl detaches from the chain and the dangling bond in the silicon atom replaces the hydrogen in the OH group and attaches to oxygen. In the presence of oxygen in the environment, a polymerization reaction takes place between the different OTS molecules linking silicon atoms together with an oxygen atom in between to form a monolayer covering the silicon oxide surface and removing hydrogen from the surface (see Fig. 3.5).

OH group on the surface of the silicon oxide acts as a pinned trap for the moving charges in organic semiconductors. The dangling protons of hydrogen interact with electrons moving in the conduction channel and hinder their movement; in other words, block n-type conduction in the transistor. If the moving charges were holes, their interaction with the dangling proton would be less pronounced; nevertheless, it will create hysteresis when the gate voltage is swept forward and backward. Therefore, removing hydrogen from the surface was essential for n-type measurements and for eliminating a possible trapping factor in p-type measurements. However, OTS self-assembled monolayer (SAM) has another effect which is making the surface hydrophobic. This effect must be optimized in such a way to allow for the molecules to be deposited.
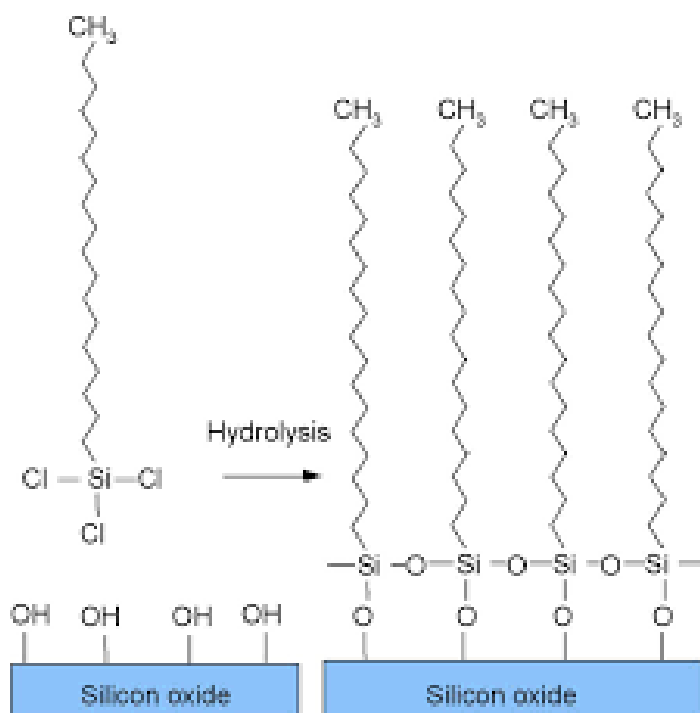
Fig. 3.5 OTS SAM on silicon oxide functionalization process.

For applying the OTS SAM on the substrate, a protocol was followed. A solution of OTS molecules and toluene with an OTS concentration of 20 µg/ml was prepared inside the glove box where oxygen and water vapor concentration were kept to the minimum. The substrate was emerged inside the solution and was left for two hours. The reason that the process had to be inside the glove box is that the presence of water boosts the polymerization process too much and a thick film is formed on the substrate. The duration of the process along with the concentration of the OTS in the solution determine the coverage percentage of the surface. However, the perfect coverage, in this case, is not desired as it makes the substrate too hydrophobic for the molecules to be deposited. Indeed, after several trials, these parameters were found to be the optimum for this application. After the two hours, the substrate was then taken out from the solution and rinsed in toluene followed by hexane followed by isopropanol then dried out using a nitrogen flow.

The PFBT molecule is a benzene ring with all the hydrogen atoms substituted with fluorine atoms except one which is substituted with SH group. This SH group is responsible for the attachment to the gold surface after the hydrogen atom is released and the S atom attaches to the gold (see Fig. 3.6). The extremely high electronegativity of the fluorine atoms is the main reason for creating a dipole interaction with gold leading to a change in its work function. However, as the work function of the metal decreases in response to the PFBT SAM, it becomes closer to the HOMO of the semiconductor than the LUMO. Thus, PFBT SAM on gold electrodes blocks n-type conduction and facilitate p-type conduction.

For applying PFBT SAM on the gold electrode, the following protocol was followed. After cleaning the substrate as previously explained, the substrate was emerged in a solution composed of PFBT molecules and isopropanol with a ratio of 4 µl/12 ml. The substrate was left in the solution for five minutes then was rinsed with isopropanol and then dried out using a nitrogen flow. The substrate is then immediately were used for the molecules' deposition.
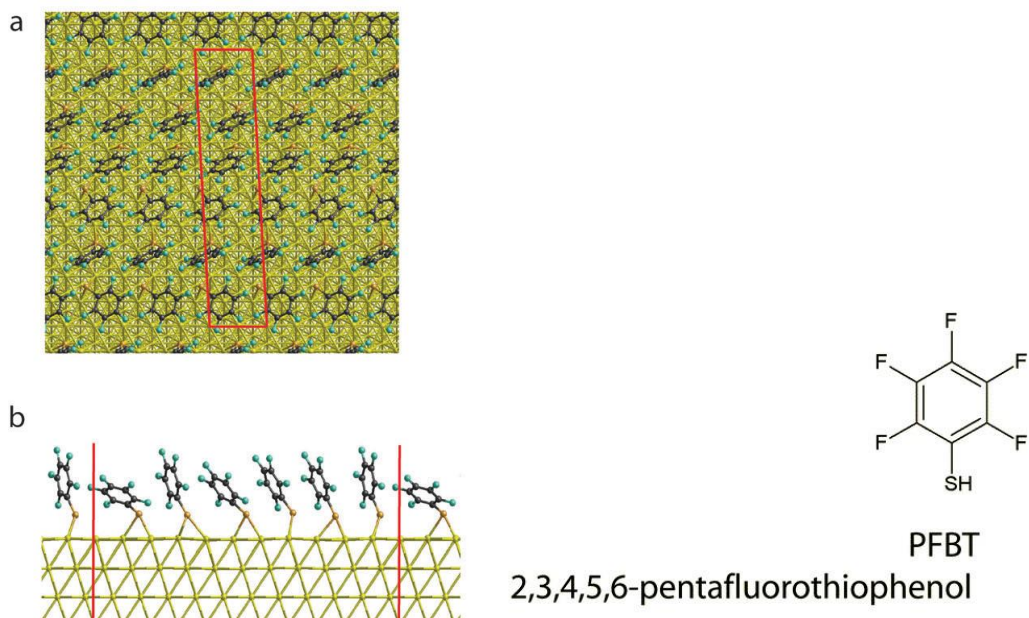
Fig. 3.6 PFBT molecule on the right and its self-assembled monolayer on the gold surface on the left where (a) is the top view while (b) is the side view [47].

3.2.3 Drop casting

The main technique that was used in this work to deposit the molecules is drop casting. Drop casting is a simple solution-based deposition technique. In this technique, a drop of the solution containing the molecules is dropped on the substrate and left to dry. After the solution is all dried out the left molecules on the substrate form the desired deposition.
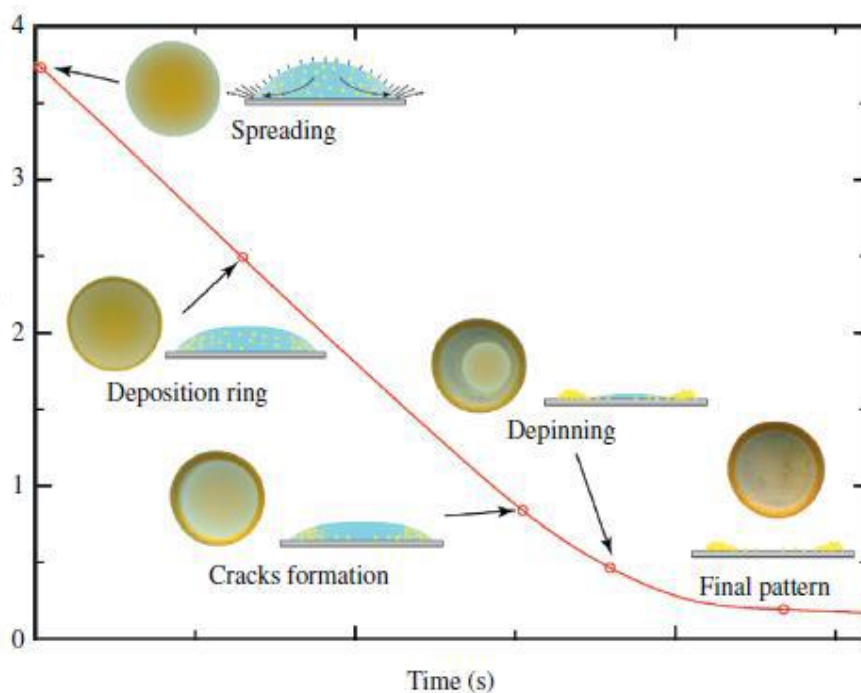
Fig. 3.7 Drop casting deposition process is represented as a function of time showing different phases of the evaporation where at the depinning point the phase changes from uniform deposition to a disordered low thickness deposition [48].

This technique is characterized by a coffee stink pattern of deposition. At the beginning of the deposition, the molecules take their time to accumulate on the borders of the droplet and form thick more uniform

44

deposition. As the droplet diameter and height further decrease the evaporation process enters in a different phase where fast evaporation occurs and deposition of less uniformity and thickness results in the middle. In Fig. 3.7 the deposition process is represented as a function of time showing different phases of the evaporation where at the depinning point the phase changes from uniform deposition to a disordered low thickness deposition. Many factors affect this process: the solvent, the molecules, the surface, the temperature, the amount of solution which was dropped, these factors make the optimization of the deposition process.

In this work, Dichloromethane (CH_2Cl_2) was used as a solvent for the cumulenic molecules and hexane was used for the polyynic molecules. The molecules concentration in the solvents was the same for all molecules of 4 mg/ml. The solvent and the concentration were chosen after the work of Y. Pensotti. He worked on the cumulenic molecules to optimize their deposition conditions and Raman characterizing them [48]. A certain amount of the solution was sucked by a micrometer pipette and released on the substrate to evaporate. The amount of the solution to be drop casted was around 100 µl per substrate. This amount was chosen after different trials to determine the best amount. The major problem that was faced was the film uniformity. Since the substrate contains sixteen different devices, the loss of uniformity changes the film shape and thickness from device to another. However, drop casting technique allows the crystals to form freely which decreases the defects in the crystals and produces large crystalline domains.

3.2.4   Spin coating

Spin coating technique is similar to the drop casting technique, but in this technique, the substrate is fixed on a rotating stage. Right after dropping the solution on the substrate the stage starts to spin to cause a centrifugal force on the solvent which was just dropped. This centrifugal force leads to fast evaporation and more uniform film. The film properties depend on the acceleration and the final speed of the rotating stage (see Fig. 3.8). The solvent, the molecules, the surface tension, the temperature and the amount of solvent dropped play a similar role like in the case of the drop casting technique.
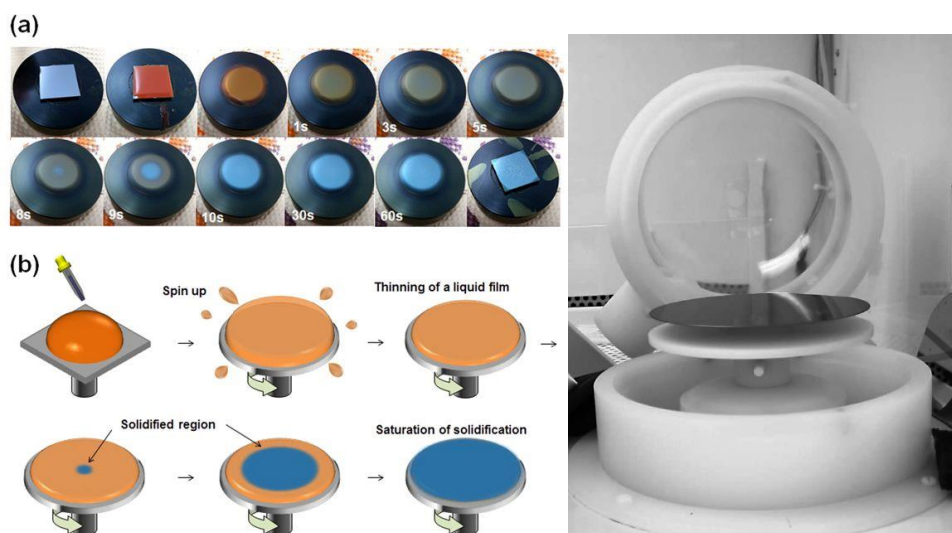
Fig. 3.8 Spin coating film formation stages on the left [49] and a picture of the spin coater on the right

3.3   Characterization techniques

During the work, Raman spectroscopy, UV-Vis spectroscopy and electrical characterization for the molecules were done and, in this section, the procedures which were followed to obtain the results along with the protocols for data collection and analysis will be explained.

3.3.1   Raman

The Raman spectrum of the four molecules was obtained in the solid-state form. The molecules were deposited on the Fraunhofer substrate and a silicon substrate using the drop casting deposition technique and were characterized using two micro Raman measuring instruments. For each instrument one laser type was used, argon ion (Ar+) laser with a wavelength of 514,5 nm (green laser) for the first instrument (see Fig. 3.9) and laser diode with a wavelength of 785 nm (red laser) for the second instrument. With the green laser, two intensities were used 1 mW and 0.1 mW. The red laser was used in two intensities as well, 1 mW and 10 mW. The laser was focused on the molecules using integrated optical microscope lenses of magnification 5X, 10X, and 50X. With the red laser, two types of lenses were used: long focal length lenses and short focal length lenses.

To obtain the spectrum, the instrument was calibrated with silicon and the peak was centered at 520 cm^{-1}. After the calibration, the spectrum of the molecules was obtained in a dark room to reduce the noise.

Fig. 3.9 Micro Raman instrument (used for green laser).

3.3.2   UV-Vis

The UV-Vis spectrum of the molecules was obtained using two experimental setups, direct setup and an integrating sphere setup. The direct setup as shown in Fig. 3.10 only collects the direct transmitted light through the sample. The light coming from the monochromator is split into two beams, one beam passes through the sample and the other passes through a reference sample. The transmitted beam from the sample is detected by a detector placed in front of the sample. Thus, only direct transmitted light is detected while

scattered light is not. The integrating sphere setup as shown in Fig. 3.11 allows the collection of the scattered light as well as the direct transmitted light. In this setup, the data can be collected in transmission mode or reflection mode depending on the place of the sample in the sphere. However, the reference sample spectrum should be measured separately.
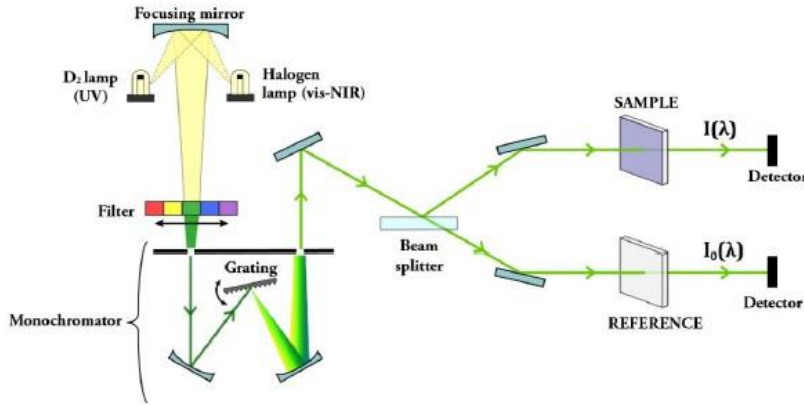
Fig. 3.10 Direct transmission setup.

Glass substrates were used for the transmission measurements and Fraunhofer substrates were used in the reflection measurements. The protocol that was used to obtain the spectrum was as follows. First, a baseline frequency sweep is done by the instrument where no sample is installed. After the baseline check, the sample is installed along with the reference sample in the direct setup or alone in the integrating sphere setup. The spectrum is collected for the sample and the reference sample and the data is deduced according to the following formula:

$$T_M = \frac{T_S}{T_0} \quad (3.1)$$

where T_M, T_S and T_0 are the film transmittance, sample transmittance and reference sample transmittance respectively. The absorbance is deduced out of the transmittance according to the following relation:

$$A = 2 - \log_{10} T \quad (3.2)$$

where A is the absorbance and T is the transmission in percentage.
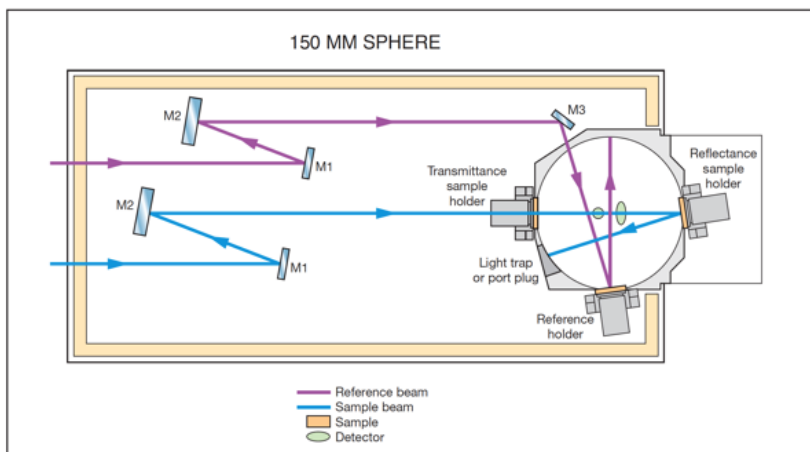
Fig. 3.11 Integrating sphere setup.

3.3.3   Electrical characterization

The main work in this thesis was to characterize the solid-state form of the investigated molecules electrically. This electrical characterization was done in two ways, resistivity measurements and transconductance measurements. The solid-state form of the molecules was obtained using the previously described deposition techniques, drop casting and spin coating. The characterization was done on the Fraunhofer substrates in an inert atmosphere inside a glove box with water and oxygen concentrations of around 0.1 – 0.5 ppm respectively. The instrument which was used in the characterization is the Agilent B1500A Semiconductor Device Analyzer with a current resolution of 0.1 fA connected to a four-probe adjustable stage with an optical microscope camera on top (see Fig. 3.12).
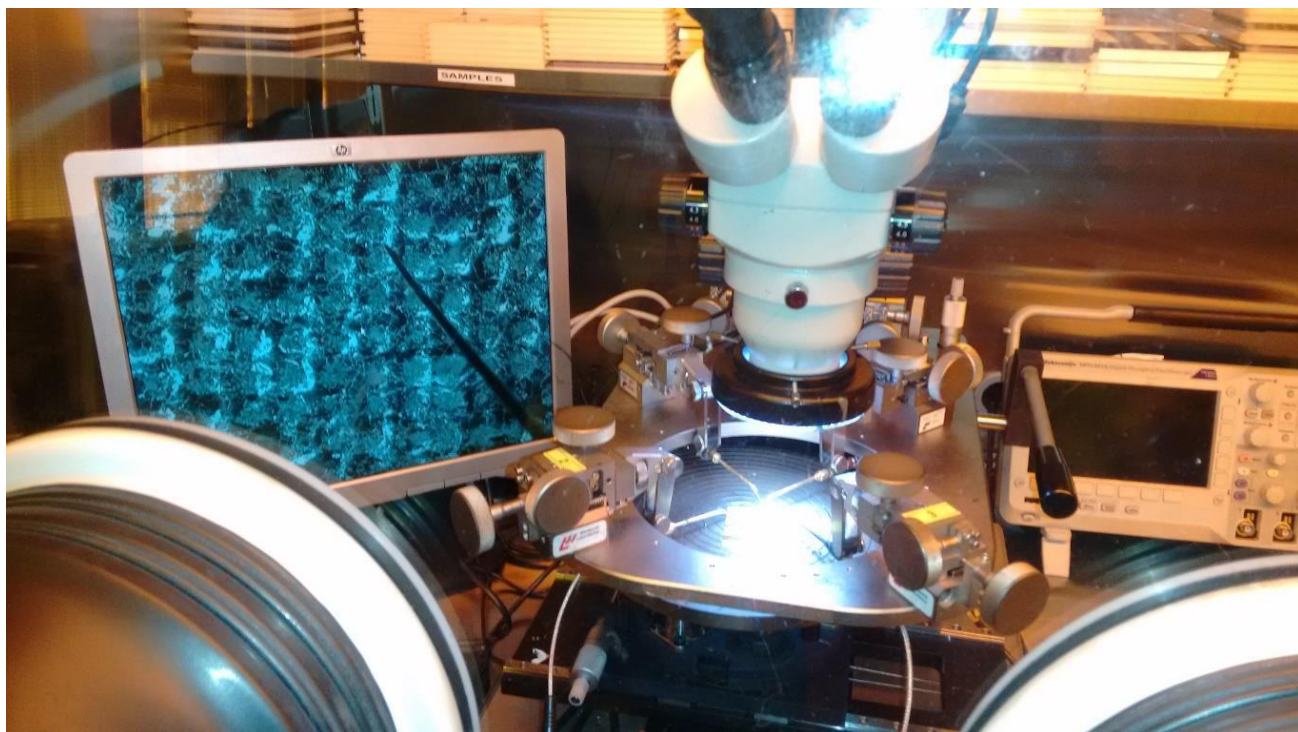
Fig. 3.12 The four-probe stage inside the glove box with the optical microscope camera.

The resistivity measurements of the molecules were done using two probes, one is the source and the other is the drain. An I-V relation was obtained by sweeping the voltage and measuring the current. In the resistivity measurements the sweeping was fast (1.4 V per step) and the measurement started from -60 V to 60 V and the current was measured with each step. The transistor measurements were done using three probes: source, drain and gate. Since the stage is metal and the substrate has a common bottom gate, an insulator layer was put under the substrate to decrease the noise in the measurements. The transfer transistor characteristic curve was obtained by fixing the drain voltage and sweeping the gate voltage while measuring the current coming in and out from the three probes. Ideally, the gate current should be negligible and the current coming out from the source probe should be exactly equal to the current coming into the drain probe. However, a non-negligible leakage gate current is often encountered, which on the other hand has to be lower than the source-to-drain current.

Giving all probes are properly connected to their electrodes, four gate voltages sweeps were done to obtain the transfer characteristic curve. Forward and backward sweeps in the linear regime with a fixed low drain voltage and forward and backward sweeps in the saturation regime with a fixed high drain voltage were done. The sweeping was optimized to medium speed (0.75 V per step). For p-type measurements the gate voltage was swept between 10 V and -60 V wherein the linear regime the drain voltage was kept fixed at -5 V and in the saturation regime the drain voltage was -60 V. For the output curve, the drain voltage was swept seven

times from 0 to 60 V and the drain current was measured along the sweep. The gate voltage was kept constant during each sweep and was increased by a value of 10 V from sweep to sweep starting from 0 V during the first sweep up to 60 in the seventh sweep.

For analyzing the data and extracting the parameters, the transfer characteristic curves were used even though the same parameters can be deduced from the output curves. A MATLAB code was written and used for the main data analysis. The main parameter that was extracted using the MATLAB code is the field effect linear and saturation mobilities. The linear mobility was plotted against the gate voltage according to the following relation:

$$\mu_{Lin} = \frac{L}{W C_i V_D} \frac{\partial I_D}{\partial V_G} \quad (3.3)$$

where L, W and C_i are the channel length, channel width and dielectric capacitance respectively. While the saturation mobility was plotted against the gate voltage according to the following relation:

$$\mu_{Sat} = \frac{2L}{W C_i} \left(\frac{\partial \sqrt{|I_D|}}{\partial V_G} \right)^2 \quad (3.4)$$

The derivatives in both equations were calculated numerically and the I_D/ V_G curve was smoothed using the Savitzky-Golay numerical filter method.

The threshold voltage was deduced as the intercept of the I_D/V_G curve fit with V_G axis for the linear regime and the $\sqrt{|I_D|}$/V_G curve fit with V_G axis for the saturation regime.

4 Results and discussion

In this chapter, the results obtained during the work will be presented and discussed. In the first part of the chapter, the properties of the molecules will be shown, after that the electrical characterization of the molecules will be presented which is the main aim of the work.

4.1 Molecular, structural, vibrational and electronic properties

In this section, the properties of Ph3 and Ph5 molecules will be presented. The structural properties obtained through XRD data (provided by Tykwinski group) and the optical microscope along with the scanning electron microscope image analysis will be shown. The vibrational properties will be discussed through Raman analysis. The electronic properties will be analyzed through the discussion of UV-Vis spectra of the molecules.

4.1.1 X-Ray analysis

By analyzing the XRD data provided by the Tykwinski group of Ph3 and Ph5 molecular crystals, some minor differences in packing were found. Although both molecules adopt the same packing configuration (Herringbone packing) but one important difference is that Ph3 crystal has two molecules per unit cell while Ph5 crystal has four molecules per unit cell. The difference between the molecules in one unit cell is in the torsion angles of the phenyl groups which is slightly different from one phenyl group to another. These differences in the torsion angles make both Ph3 and Ph5 molecules slightly asymmetric from one side of the chain to the other. Another difference which can be noticed is that the chain in Ph3 has a little bend while in Ph5 the chain is perfectly straight.

Fig. 1.1 shows the unit cell for Ph3 and Ph5 with the distances between the molecules in the unit cell (the data obtained from XRD on powder of Ph3 and Ph5). We can see from the figure that the nearest neighbor intermolecular distance in Ph3 is slightly longer than Ph5 (longer by 0.1 A). However, there are some other differences in the torsion angles of the phenyl groups and the frustration in the bond angle of the sp^2 atoms on the sides of the chain (the angles are different from 120). The torsion angles are important for the π-conjugation and in Ph3 the angles are 26.5, 36.5, 27.5 and 34.5 degrees for the four phenyl groups while in Ph5 the angles are 33.9, 34.5, 32.3 and 24.5 degrees for the four phenyl groups. Generally, the differences in the angles in Ph5 is less than Ph3 which is expected since Ph5 is longer and has less steric hindrance. Moreover, the frustration in the sp^2 angle in Ph5 is less than Ph3 which can be attributed to the same reason (Ph5 angles are 120.5, 121.3 and Ph3 angles are 121.2, 122.6).
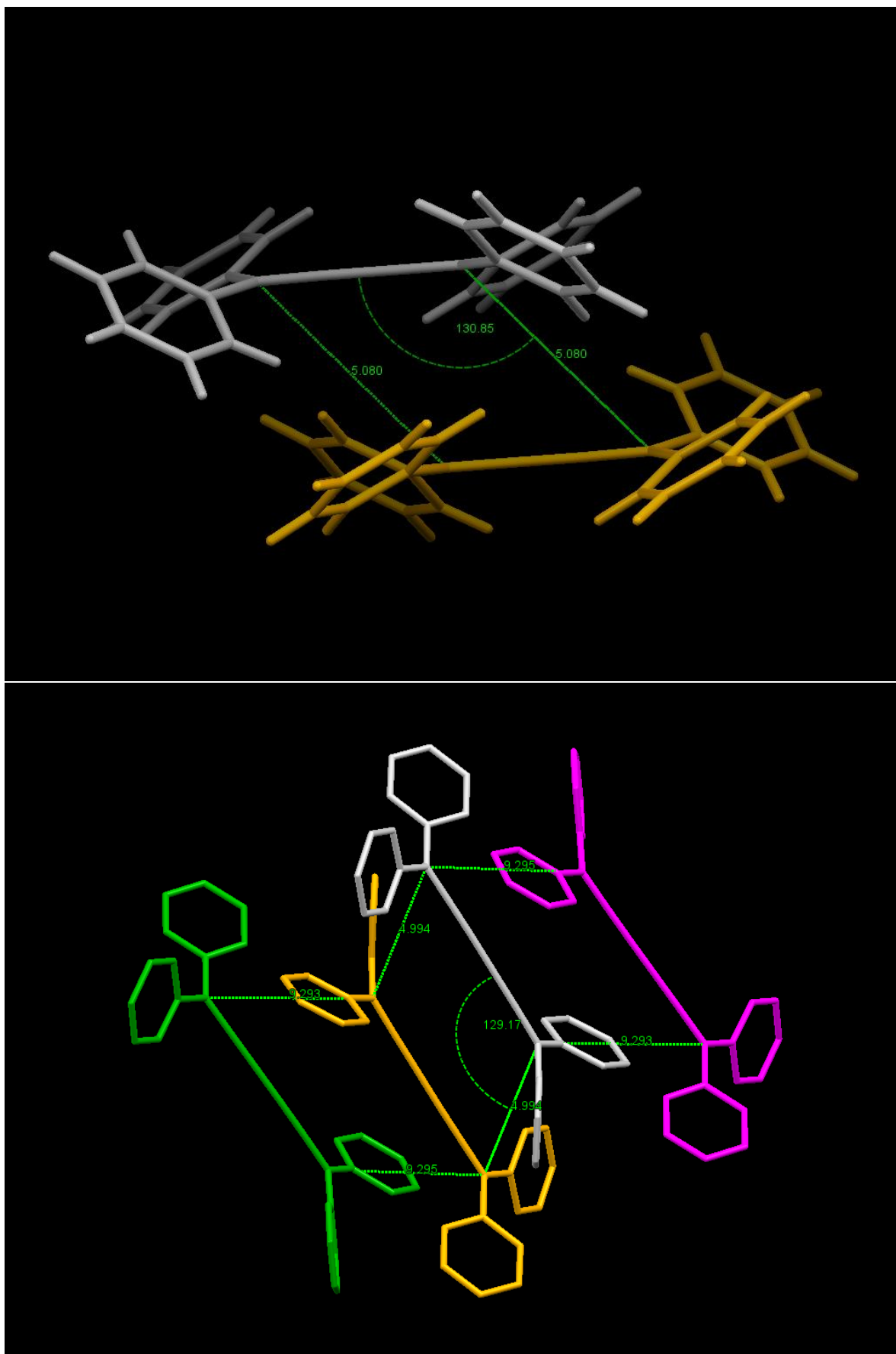
Fig. 4.1 Ph3 (top) and Ph5 (bottom) molecules in one unit cell with intermolecular distances shown in angstroms (different colors represent different symmetry).

4.1.2   Molecular crystals morphology

Before performing any characterization on the molecules, it was useful to have an idea about the general features of the deposited films. Drop casting and spin coating were used to obtain the films and by analyzing the images obtained by the optical microscope and SEM of these films, a general idea about the crystallization of the molecules under different conditions was obtained.

Ph3 and Ph5 molecules are known to crystallize in needle-like crystals. Using drop casting technique, the crystallization of the molecules was slower which led to the formation of long crystals while with the spin coating method the fast evaporation of the solution induced smaller crystals with smaller voids in between. This difference can be seen by analyzing the images of the deposited films. Nonetheless, the difference between the morphology and the crystals sizes between the drop casted films and the spin-coated films is extremely obvious.
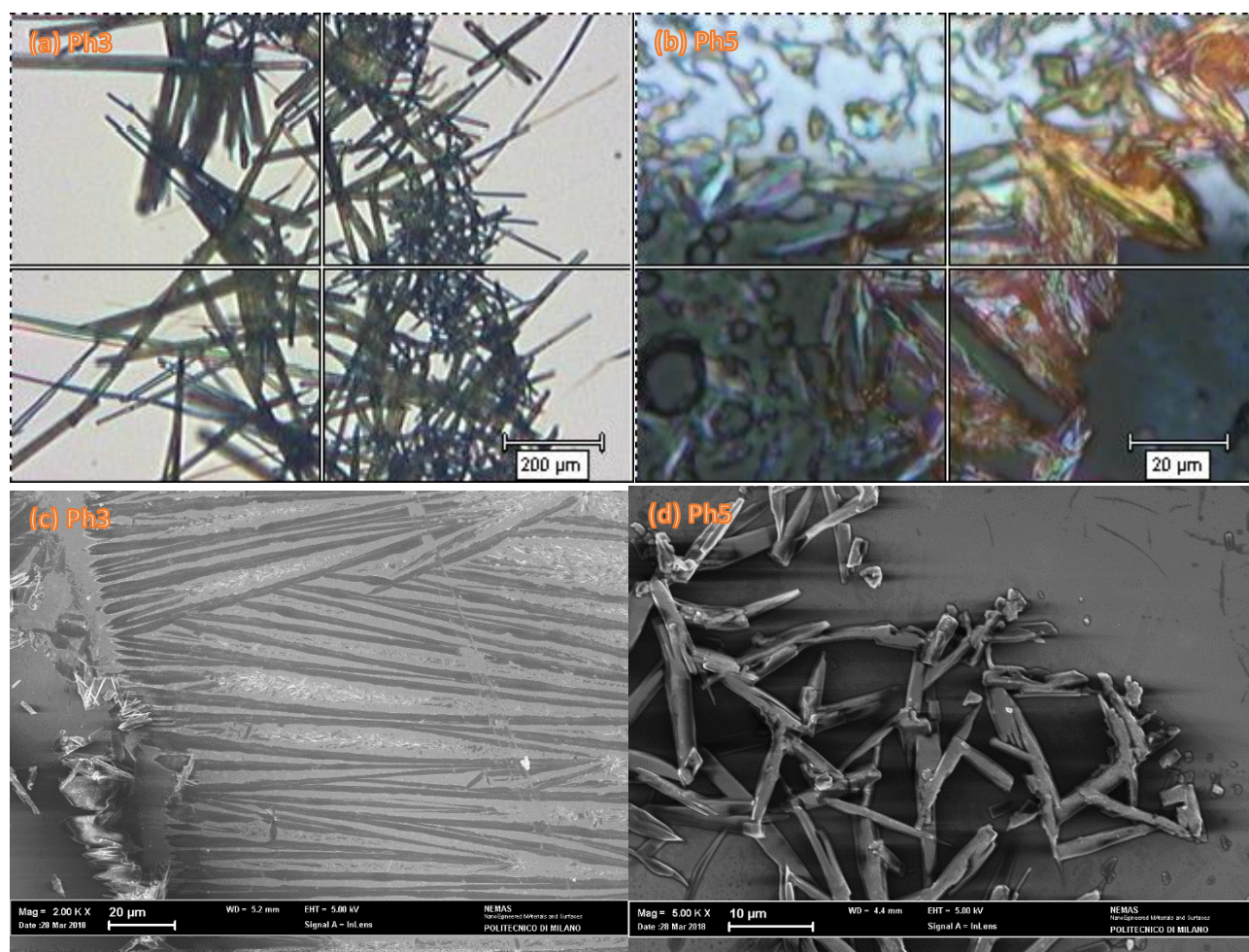
Fig. 4.2 Ph3 (a and c) and Ph5 (b and d) images taken by the optical microscope (top) and SEM (bottom) of the molecules deposited using drop casting technique.

The top panels of Fig. 4.2 show the optical microscope images of drop casted Ph3 crystals and Ph5 crystals. From these images, two pieces of information can be deduced. First, the uniformity of the film and the percentage of the surface coverage, second, the average size of the crystals of Ph3 and Ph5. The uniformity as it is clear from the images is not present in both molecules while the surface coverage is by far very low. The crystals of Ph3 are longer in general than the crystals of Ph5 and from the scale on the images, an estimation of the average crystal length of Ph3 is of the order of hundreds of microns while of Ph5 is of the order of a tenth of microns. However, the density of the film and the surface coverage are found to be a function of the crystal average length and size, the longer the crystals, the less dense is the film. This relation extends

throughout the analysis of different deposition techniques as well. More detailed information can be deduced from SEM images of Ph3 and Ph5 (bottom panels). From the SEM images, we can estimate the average length of Ph3 crystals to be between 200 and 300 μm while the average length of Ph5 crystals can be estimated to be between 20 to 30 μm (this is in the case of drop casting).
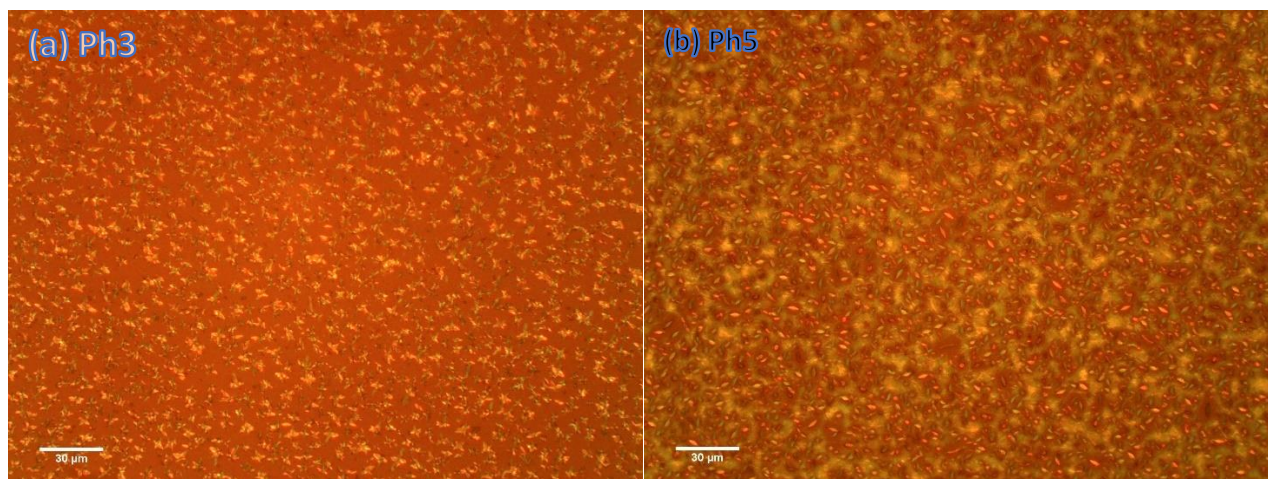
Fig. 4.3 Optical microscope images of spin-coated films for Ph3 (a) and Ph5 (b)

Fig. 4.3 shows the optical microscope image of Ph3 and Ph5 films obtained using the spin coating technique. For both molecules, the films are denser and with much smaller crystals than the case of the drop casting technique. An estimation of the average crystal dimension in both cases would be some micrometers. This difference in dimensionality between the two deposition techniques will be very pronounced throughout the analysis of the molecules.

4.1.3   Raman

Raman spectra of the molecules were obtained and compared with the previous work on the same molecules in order to be able to use their spectra as a fingerprint throughout the characterization. Moreover, the differences between the Ph3 and Ph5 Raman spectra gave an insight into the differences between the two molecules. Indeed, in this subsection, the Raman spectra of these molecules will be discussed identifying those differences and realizing the sp-carbon fingerprint peak for each molecule.
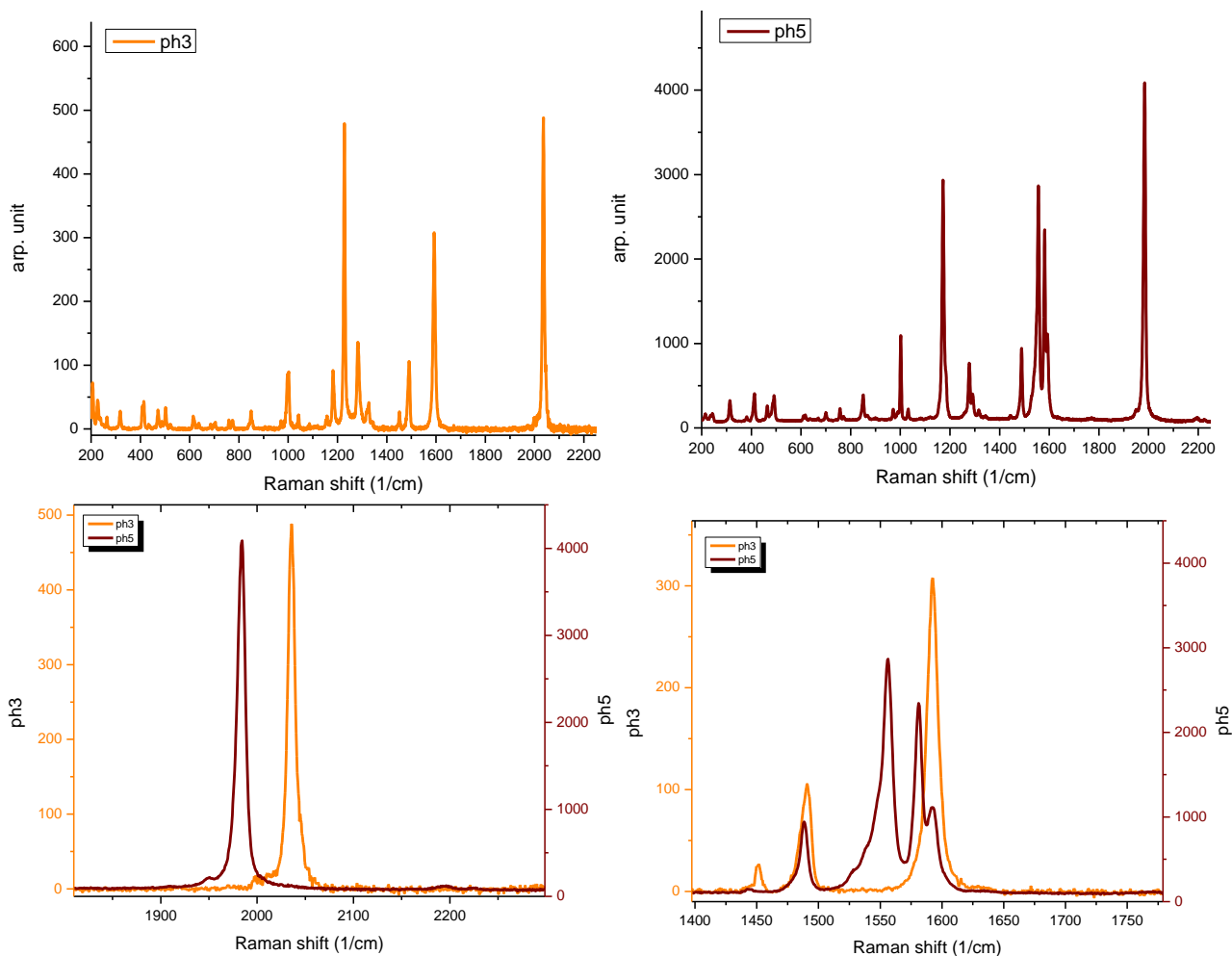
Fig. 4.4 The Raman spectra of Ph3 (top left) and Ph5 (top right) with the comparison between their spectra in the region of sp carbon peak (bottom left) and the sp^2-carbon peaks (bottom right).

In Fig. 4.4 the spectra of Ph3 (top left) and Ph5 (top right) is shown and the peaks corresponding to the sp-carbon can be identified in the region from in the 1800-2500 cm^{-1}. The peaks related to the sp-carbon in the Ph3 and Ph5 molecules are isolated (bottom left) and by comparison, one can see the redshift of the Ph5 peak (centered at 1985 cm-1) with respect to the Ph3 peak (centered at 2037 cm^{-1}). This redshift is an indication of a lower BLA value of Ph5 than Ph3. This is indeed consistent with the calculated band gap for the two molecules, 3.21 eV for Ph3 and 2.72 eV for Ph5 (the calculation was done by A. Milani). On the other hand, the phenyl groups in the two molecules can be identified in the Raman spectra as well, in the region from 1550 to 1600 cm^{-1}. By comparing the two molecules' spectra in this region (bottom right), it is found that the aromatic ring peak in Ph5 is split in two unlike the case in the peak of Ph3. This split is explainable by the presence of two phenyl groups on each side of the molecule, as the split in the peak indicates that the two phenyl groups feel a slightly different environment. However, the absence of the split in Ph3 peak can be an indication of the absence of a different environment with respect to the two phenyl groups.

Fig. 4.5 Ph3 and Ph5 deposited on a silicon substrate locked inside a sealed chamber to perform Raman without exposing to air

Raman measurements were done to check the stability of the molecules concerning different situations. It was used to check the stability with time and it was used before and after the electrical characterization to check for the structural stability. Another investigation using Raman was to check if the molecules are affected by the atmosphere. The solution and the deposition of the molecules were done in the glove box with nitrogen atmosphere then the molecules were transformed in a sealed chamber with a glass top (see Fig. 4.5) to perform Raman without exposure to the atmosphere. However, the molecules showed stability concerning time, electrical measurements and exposure to the atmosphere, at least from the Raman point of view.
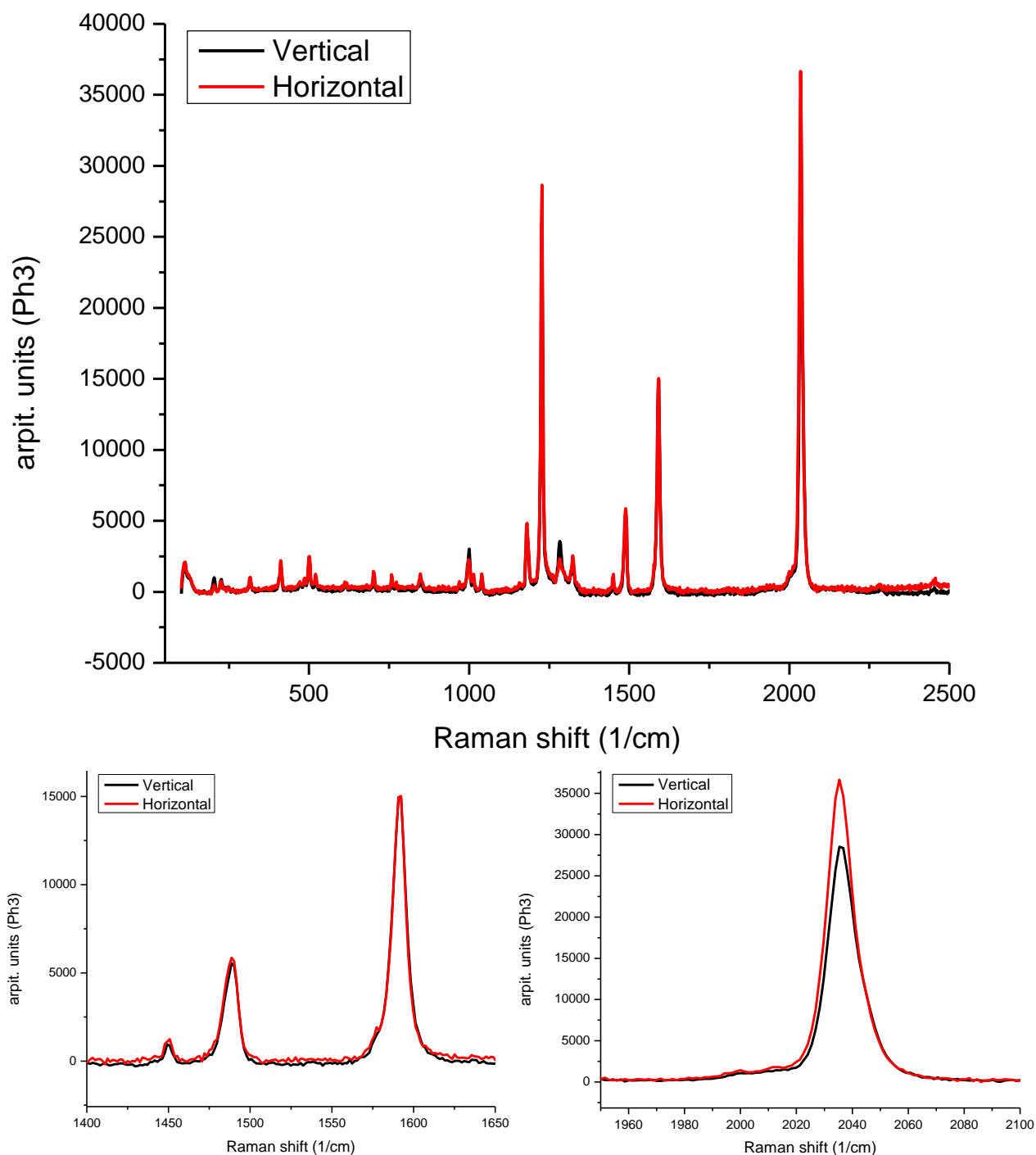
Fig. 4.6 Raman spectra of a Ph3 crystal in a vertical orientation and a horizontal orientation with respect to the Raman laser polarization (top panel) with the isolation of the sp^2 normalized peaks (bottom left) and the sp peaks (bottom right).

From the XRD data and the crystal formation, it was useful to understand whether the crystal growth is parallel or perpendicular to the carbon chain in the molecules. To answer this question, Raman analysis with polarized laser was done when the crystal is parallel and perpendicular to the laser polarization. By comparing the two spectra as shown in Fig. 4.6 for Ph3, it was found the following. The two spectra were normalized with respect to the phenyl group peak at 1590 since the phenyl rings should have no preferential orientation (bottom left panel). The sp-carbon chain peaks at 2037 cm^{-1} after normalization were different with a more intense peak for the perpendicular crystal orientation (bottom right panel). However, the polarization of this normal mode

is stronger along the chain axes; thus, we can conclude that the crystal growth direction is perpendicular to the chain axes.

4.1.4   UV-Vis

UV-Vis spectroscopy was done on Ph3 and Ph5 in the solid state for both deposition techniques, drop casting (DC) and spin coating (SC). Nonetheless, UV-Vis spectra of the two molecules in solution was provided by the manufacturer and with comparison with the solid-state spectra, some information was deduced.
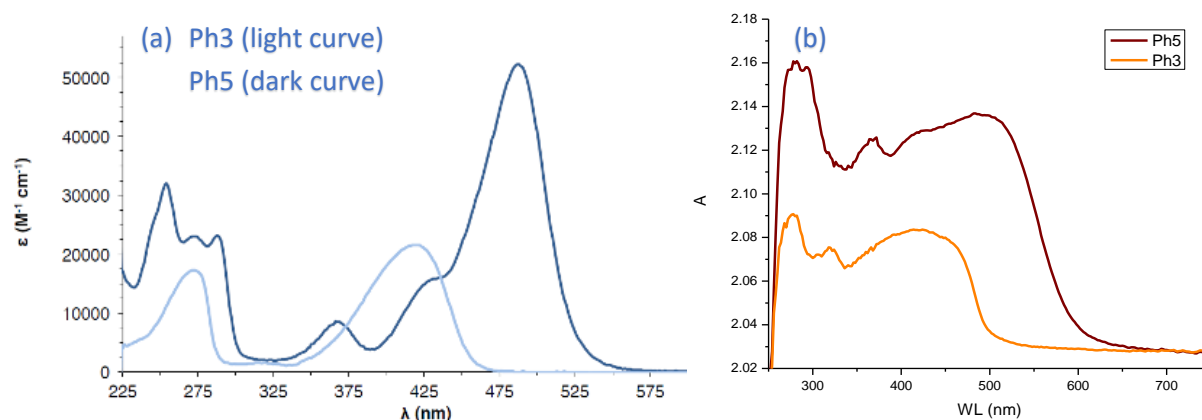
Fig. 4.7 Absorption spectra of Ph3 and Ph5 in solution (a) and when deposited using drop casting (b) with the fitting of the drop casted spectra of Ph3 (c) and Ph5 (d).

Fig. 4.7 shows the spectra of the two molecules in solution and drop casted. The spectra in solution show the typical two bands for cumulenic structures in both molecules. By analyzing the bands at longer wavelengths, we can see that Ph3 band is blue-shifted with respect to Ph5 band and the optical band gaps deduced from the spectra are 2.7 and 2.3 eV for Ph3 and Ph5 respectively. On the other hand, the solid-state form of the molecules shows lower optical band gaps for both molecules. From we can see that the bands in the solid state are less pronounced and wider than their counterpart in the solution. However, the bands at the longest wavelengths are redshifted with respect to their counterpart in the solution state. This redshift can be corresponding to a new band which is formed due to the interaction between the molecules and this band is typically of a longer wavelength than the bands of the isolated molecule. However, the optical band gaps in the solid state are 2.48 and 2.07 eV for Ph3 and Ph5 respectively.
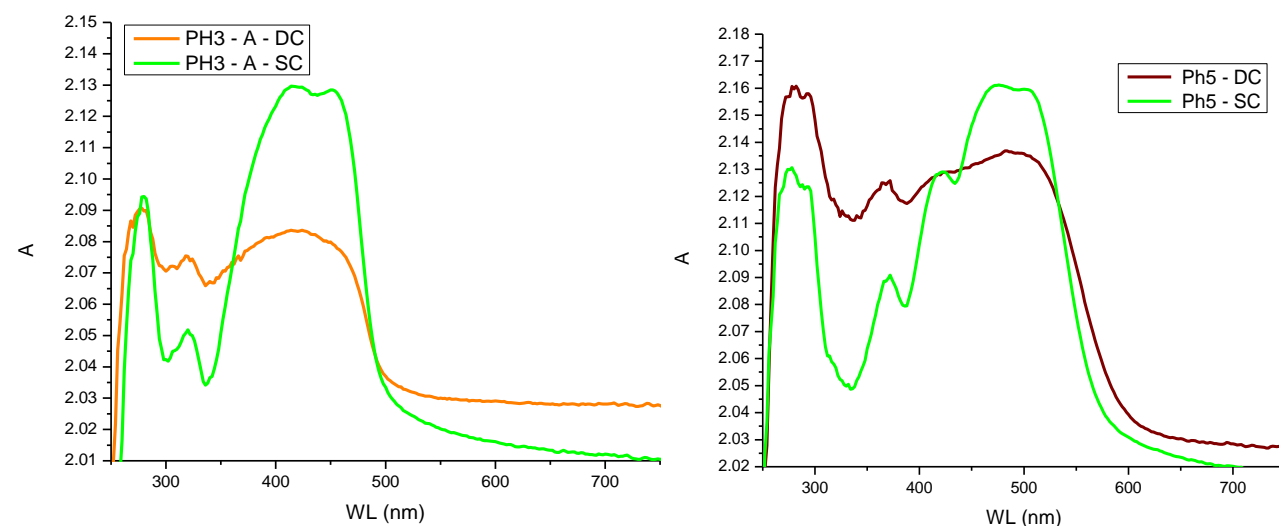
Fig. 4.8 Absorption spectra of Ph3 (left) and Ph5 (right) when deposited using drop casting and spin coating.

Fig. 4.8 shows the spectra of Ph3 and Ph5 in the solid state when deposited using drop casting and spin coating techniques. Previously it was shown that drop casting leads to bigger crystals with less uniformity while spin coating leads to smaller more uniform crystals. The difference in uniformity is pronounced in the spectra of the molecules as the spectra of the drop casted molecules are less detailed and the contrast between the strong absorption areas and the weak absorption areas is less than in the case of spin coating. When the film is less uniform and contains more voids, it allows for the light to pass through the voids without absorption leading to the saturation of the detector which may hide some bands. Indeed, the main absorption above 350 nm shows additional structured components, probably due to the solid-state interaction between molecules, which is a common feature in organic semiconductors. In particular, the main absorption present in solution is retained in the solid state, with the formation of a new absorption at higher wavelengths. This feature is present both for Ph3 and Ph5.
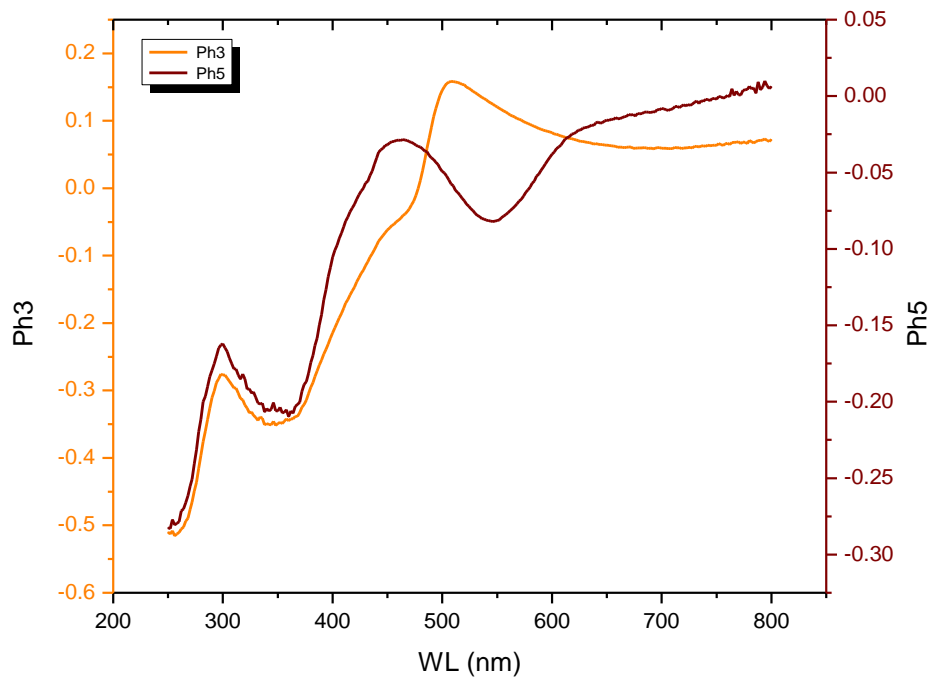
Fig. 4.9 Reflection spectra of Ph3 and Ph5 taken on the Fraunhofer substrate.

Fig. 4.9 shows the reflection spectra of Ph3 and Ph5 drop casted on the Fraunhofer substrate. In order to obtain the reflection spectra of the molecules out of the measured spectra this formula should be used:

$$R_m = R_c - R_s T_m^2 \quad (4.1)$$

where R_m, R_c, R_s and T_m are the film reflection, the collected reflection, the substrate reflection and the film transmission respectively. However, since the substrate is opaque, the molecule transmission was not obtained; thus, the plotted spectra are just the collected reflection minus the substrate reflection. Nonetheless, the bands seem to be consistent with the absorption spectra as in the case of the Ph3 the reflection decreases starting from 500 nm wavelength and in the case of Ph5 it starts at 600 nm which are the same values of the starting of the absorption for Ph3 and Ph5 respectively.

4.2   Electrical transport characterization

In this section, the resistivity measurements of the Ph3, Ph5, DPA and DPB will be presented. However, before that, a full dimensional analysis of the crystals will be presented which serve the resistivity measurements in this section and the transistor measurements in the next section.

4.2.1   Dimensional analysis

For accurate interpretation of the data, a dimensional analysis was done on the molecular crystals deposited on the measurement substrate (Fraunhofer substrate). The different types of morphology, the length and thickness of the average crystal and the substrate coverage were analyzed. Statistical data were collected by analyzing SEM images taken for the substrates with the molecules deposited on them (using ImageJ software). It is worth mentioning that the deposition method which was used mainly for the electrical characterization is drop casting. The choice of this method was based on the previously mentioned analysis for the two deposition methods. For simplicity, the area of the electrodes with the molecules deposited on top will be called the device.
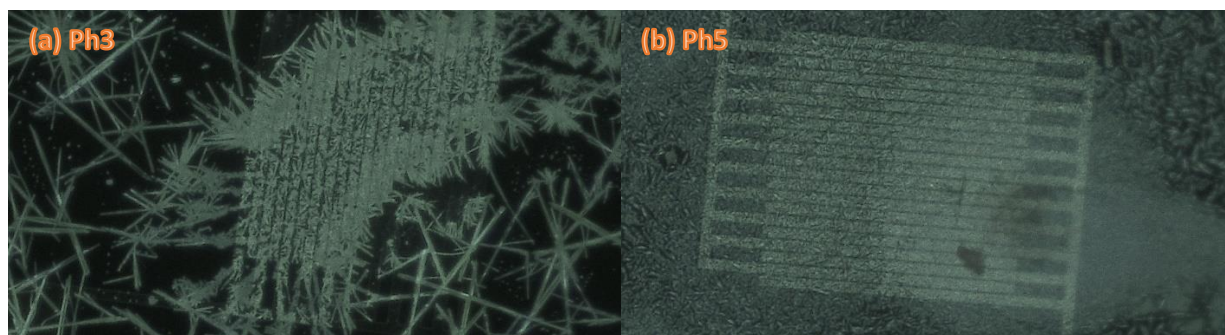
Fig. 4.10 Optical microscope images of Ph3 device (a) and Ph5 device (b).

The film morphologies of Ph3 and Ph5 molecules are very different; thus, each molecule's film morphology will be analyzed separately and differently. Nonetheless, the main features of each morphology can be compared and linked to the electrical transport properties later. In Fig. 4.10 a microscopic image which was taken by the optical microscope of the electrical characterization instrument for Ph3 and Ph5 devices before starting the measurements.
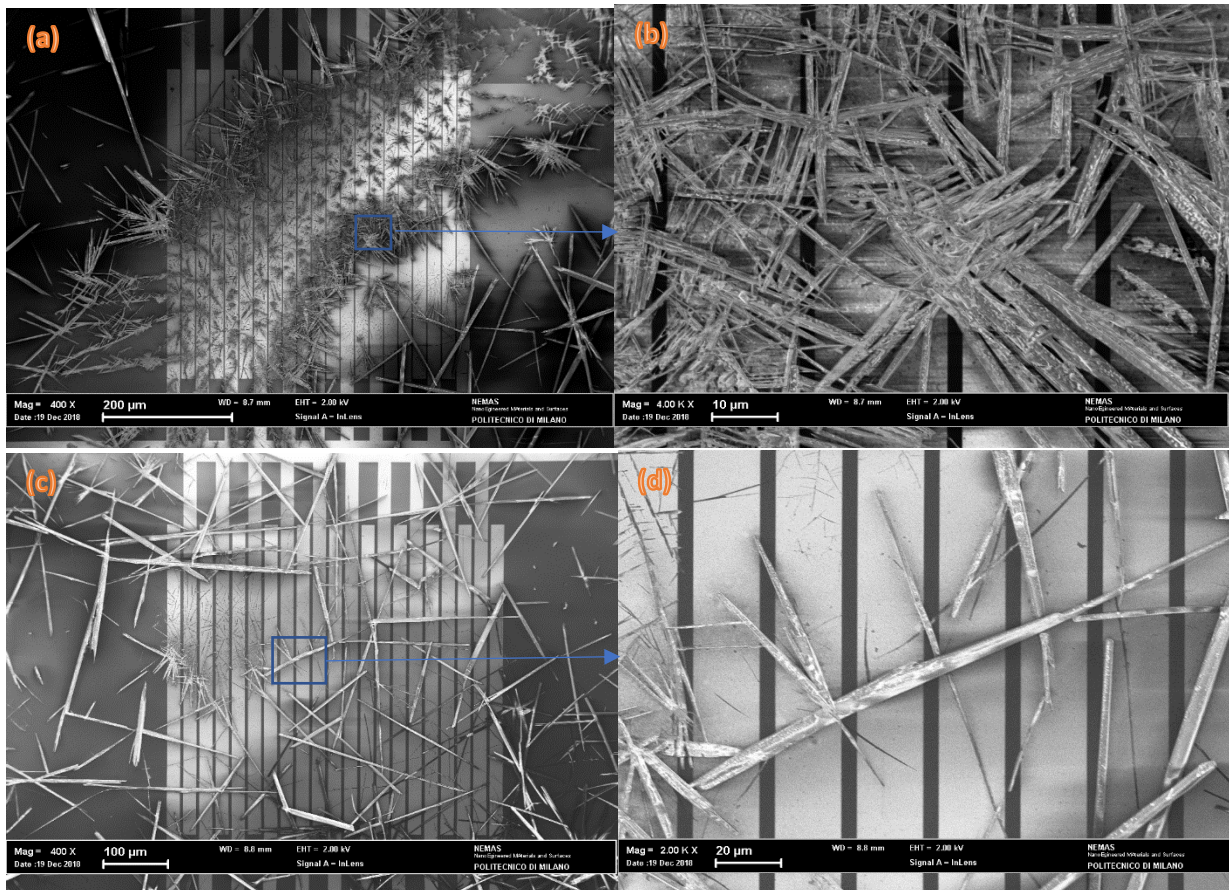
Fig. 4.11 SEM images of two Ph3 devices showing two different morphologies (a and c) with a magnification of the devices on the right (b and d).

Ph3 crystals show two main kinds of morphologies when deposited on the Fraunhofer substrate, that can be identified in Fig. 4.11 where the SEM images of two devices are shown. On the top panel, two images of the first morphology type with different magnification are shown, while on the bottom panels there is the other type of morphology. The first type can be described by shorter more dense crystals while the second type can be described as longer less dense crystals where the average crystal length in the first type is around 30 µm while in the second type it is 180 µm. It is worth mentioning that the high-performance devices of Ph3 were all of the first type of morphology and the average device coverage in this morphology was calculated to be of 30% coverage with deviations from 10 to 50% and same values were found for Ph5 as well despite the difference in morphology (the calculation were done through image analysis of the SEM images using imageJ software).
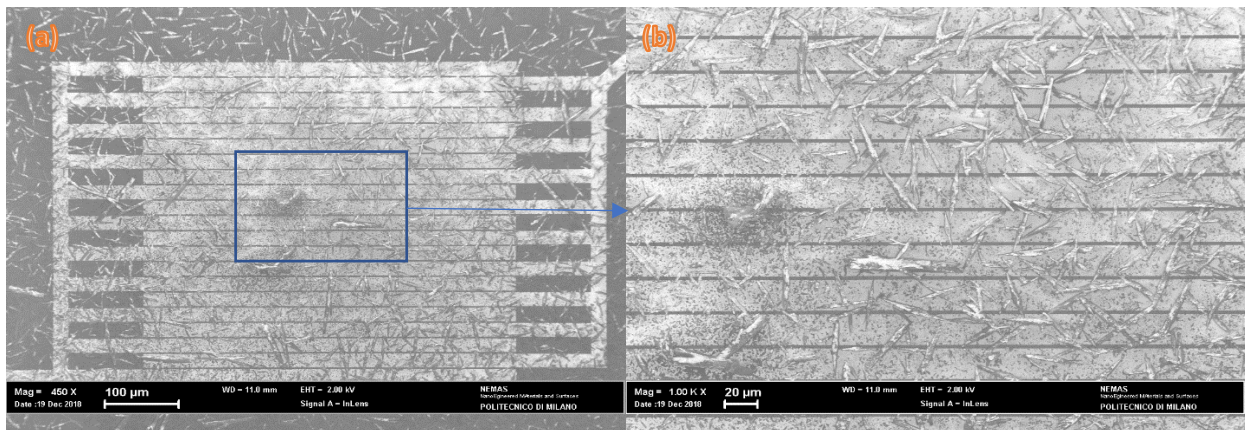
Fig. 4.12 SEM image of a Ph5 device with two different magnifications.

The Ph5 crystals, on the other hand, show more or less one kind of morphology which is shown in Fig. 4.12. From the optical microscope image, it appears that the Ph5 film is uniform and dense. However, by going to higher magnification using the SEM, it turned out that the film is composed of short crystals arranged randomly forming a low-density film. The average crystal length that was calculated is around 11 μm.
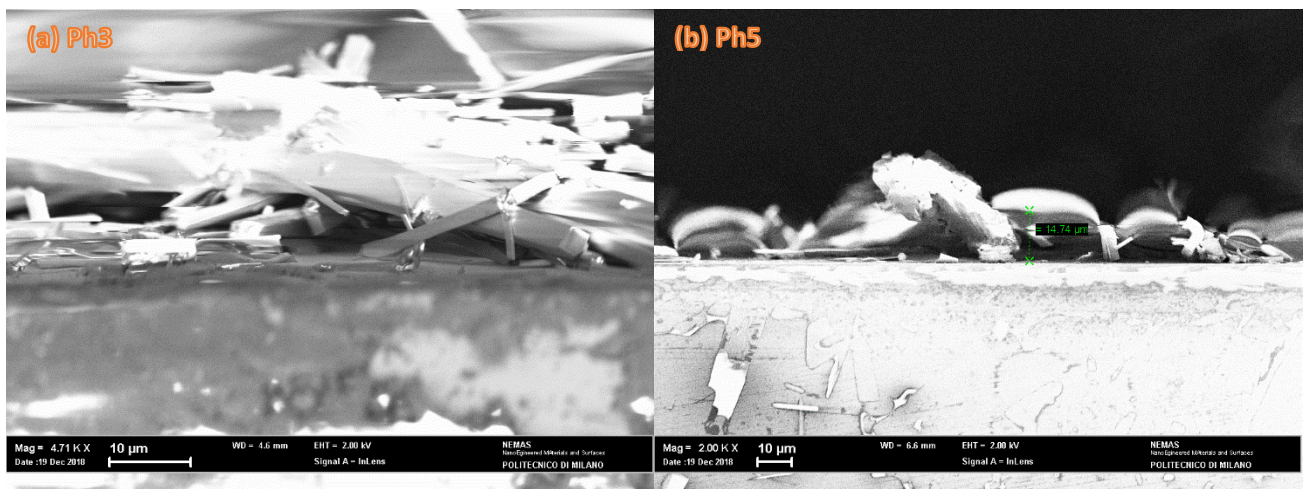
Fig. 4.13 SEM images of Ph3 (a) and Ph5 (b) taken from the side view of the Fraunhofer substrate showing the thickness and the quality of the crystal/substrate interface.

Fig. 4.13 shows the SEM images of Ph3 (a) and Ph5 (b) taken from the side view of the Fraunhofer substrate showing the thickness and the quality of the crystal/substrate interface. The average film thickness which is taken to be the median of different areas of the substrate for Ph3 is around 15 μm and for Ph5 is of the same value. However, the crystal/substrate interface as shown in the image of Ph3 is not ideal and most of the crystals are not in contact with the substrate while the situation is less severe in the case of Ph5. It is worth mentioning that these images are taken on the side of the substrate and the film morphology in the center where the devices are is very different from the sides; thus, the information taken from these images cannot be extended to the devices area in any case.

We can notice a pronounced difference in the morphology between this section and the previous section. This difference is due to many factors like the type of the substrate, the atmospheric temperature (its effect is noticeable due to the low boiling point of the solvent) and the speed of the air around the substrate in the time of deposition. Another important issue to be pointed out that different areas on the same substrate can have different morphologies and this is due to the previously demonstrated drawback of drop casting technique.
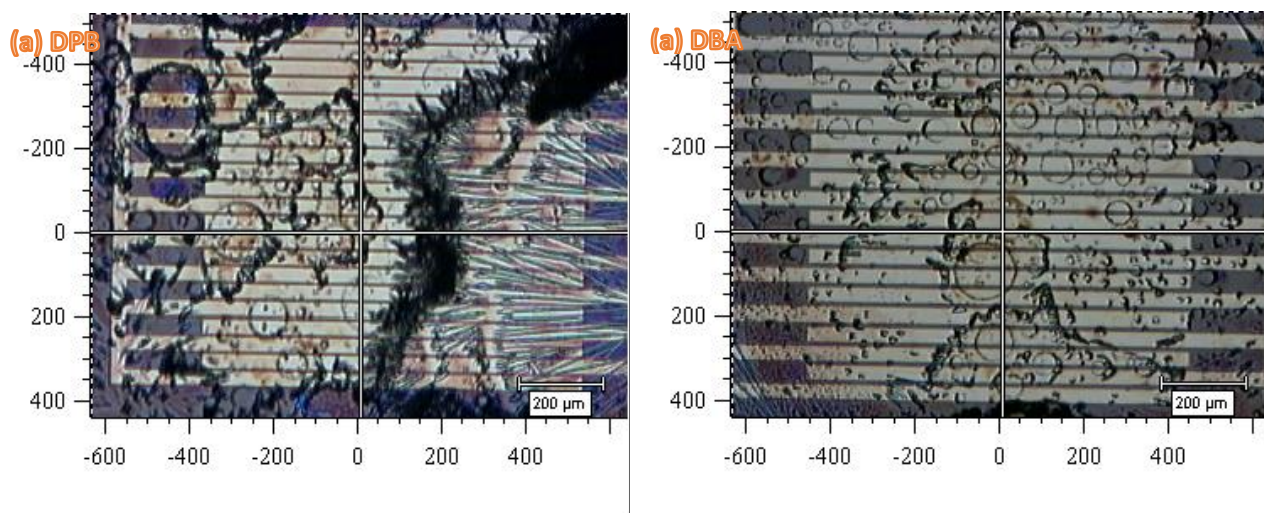
Fig. 4.14 DPB (a) and DPA (b) devices microscope images.

In Fig. 4.16 the microscope images of DPB (a) and DPA (b) devices are shown. The crystals are colorless but the differences in morphology can still be noticed

4.2.2 Electrical conductivity measurements of the deposited crystals

In this subsection, the I-V measurements on the deposited crystals for the four molecules will be presented along with the derivatives of the currents. The derivative of the current dI/dV represents the differential conductivity of the deposited crystals. It is worth mentioning that all the derivatives in this subsection were calculated numerically by Origin software and no filters were applied.
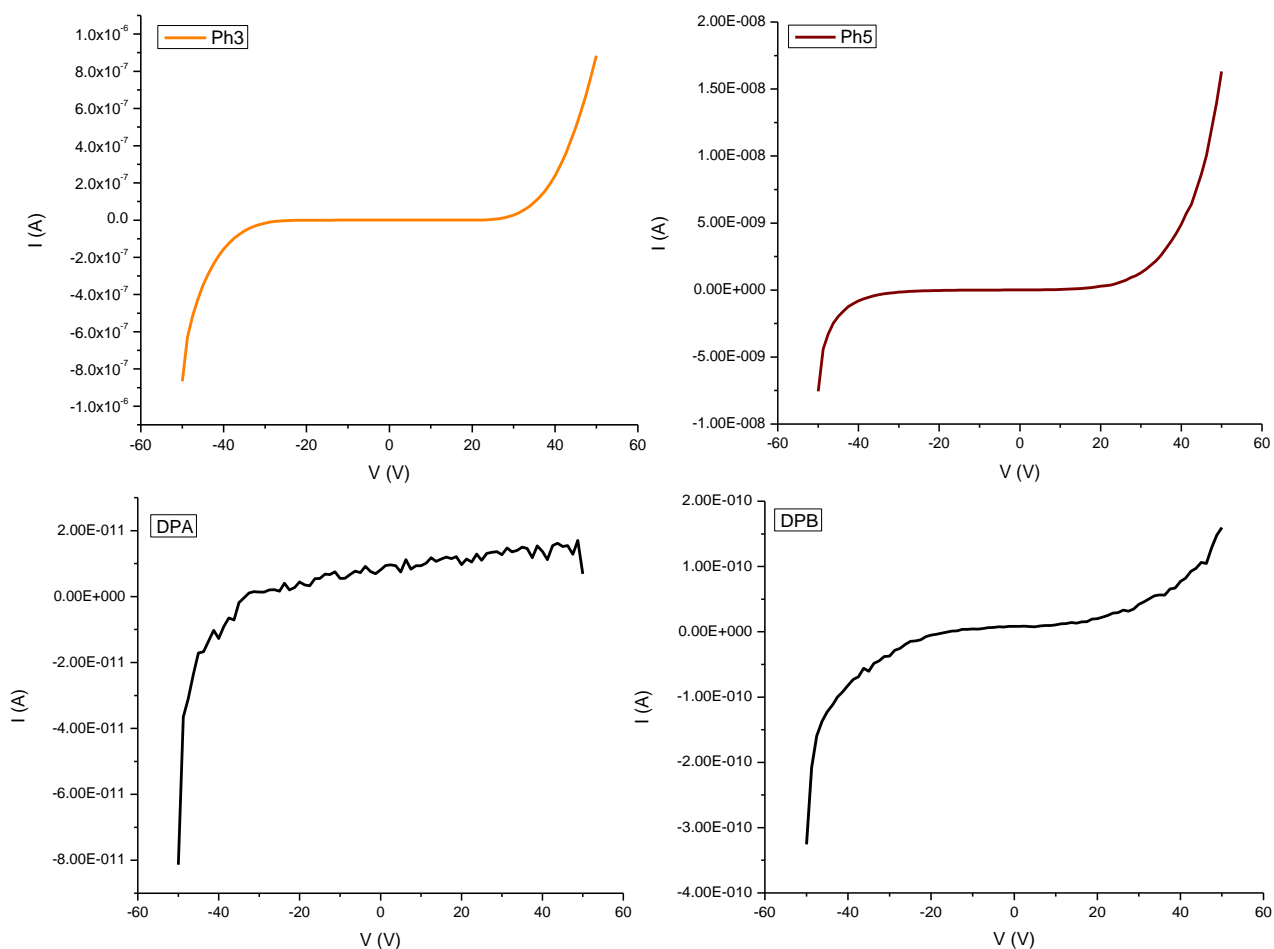
Fig. 4.15 I-V curves of Ph3 (top left), Ph5 (top right), DPA (bottom left) and DPB (bottom right).

In Fig. 4.15 the I-V curves of Ph3, Ph5, DPA and DPB molecules are shown. Ph3 and Ph5 show a moderate increase of the current at high voltages, while DPA and DPB shows a negligible current, essentially due to background noise. Therefore, Ph3 and Ph5 show a low concentration of free charges and probably upon application of a strong bias the energy levels bending allows charge injection from the contacts and therefore a certain intrinsic conductivity.
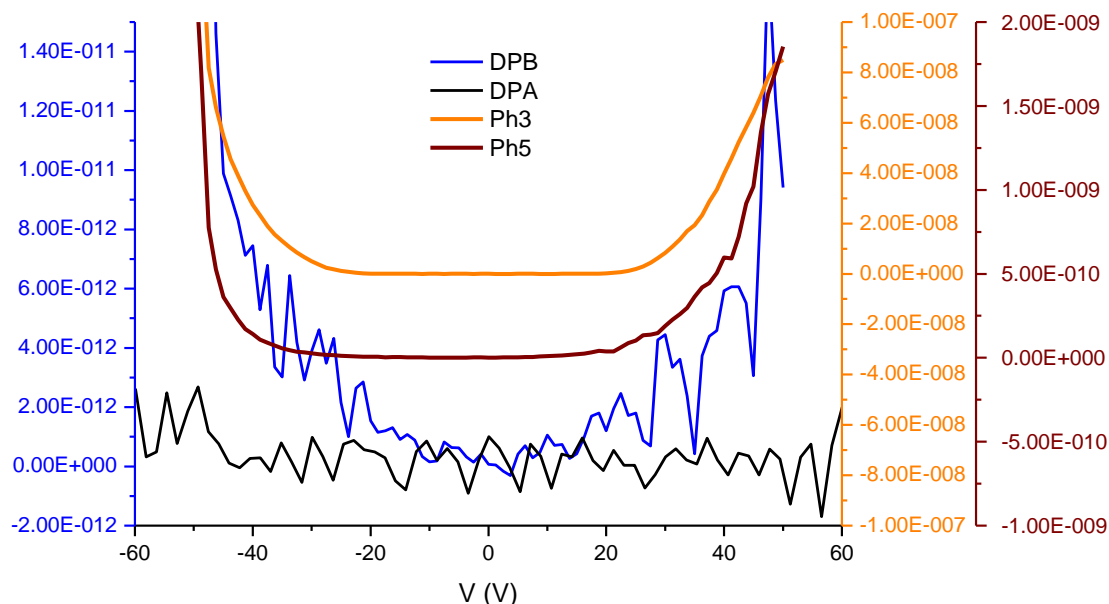
Fig. 4.16 Deferential conductivity as a function of the applied voltage of Ph3, Ph5, DPA and DPB calculated from the previous I-V curves (DPA and DPB same scale, Ph3 and Ph5 different scale each).

In Fig. 4.16 the dI/dV curves of the four molecules are shown where DPA and DPB are on the same scale while Ph3 and Ph5 each is on a different scale due to the high difference in conduction. The differences between Ph5, DPA and DPB, are logical and justifiable in the frame of their molecular structure. Ph5 is the most conjugated with the least band gap and is expected to show higher conduction which is the case. DPB comes in the second place as it is more conjugated than DPA but since it is polyynic type, the conjugation is not as pronounced as the case in cumulenic type molecules. Indeed, looking at its conduction curve, we can identify the increase of conductivity with the voltage typical for semiconductors. Going to DPA and as its I-V curve was in the noise regime, its conduction curve is indeed a flat noise with no useful information. However, the high conductivity of Ph3 is consistent with the transistor measurements which will be presented in the next section.

4.3   Field effect transistors with Ph3 and Ph5

Considering that Ph3 and Ph5 show only a low conductivity at high bias, we then fabricated field effect transistors using these molecules as the active medium. Nonetheless, DPA and DPB molecules were tested in field effect transistors as well but no current modulation was recorded using these molecules although several trials were done. On the other hand, Ph3 and Ph5 successfully showed current modulation in their devices and the transistor behavior of these molecules will be discussed. It is worth mentioning that the results which will be shown in this section are representative results aiming to demonstrate the concept. However, many devices were fabricated and tested and the observations which will be mentioned in this section are realized in most of the devices of the same case; thus, no artifacts can infiltrate through the results and affect the conclusion.

4.3.1   Transistor behavior realization

For transistor measurements, the devices were fabricated using drop casting on the Fraunhofer substrate. The Fraunhofer substrate has sixteen devices which offered the ability to have statistical data for each device fabrication.
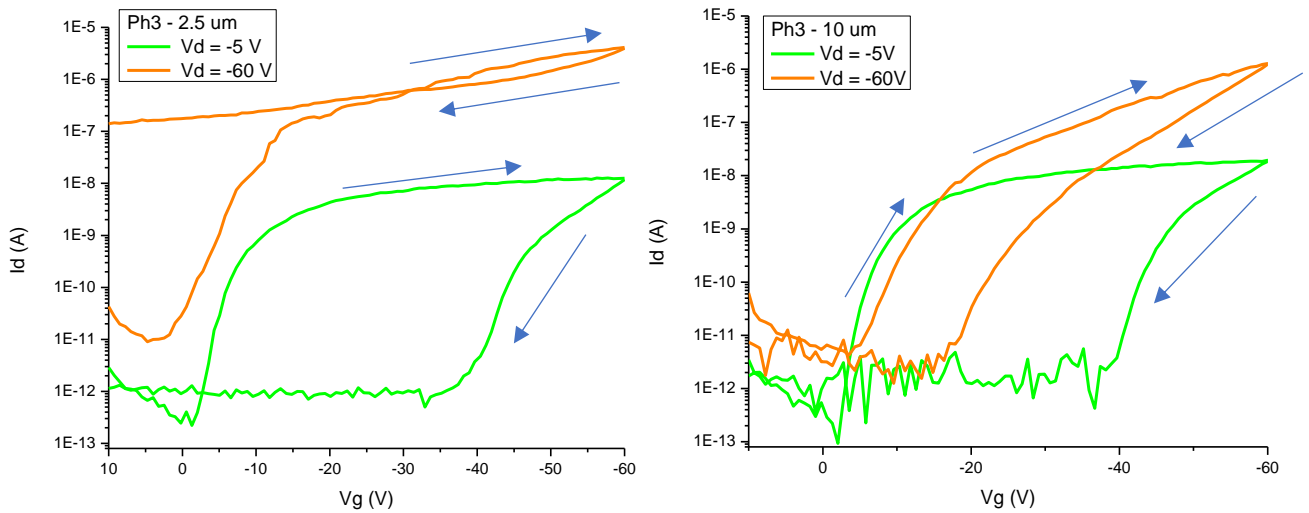
Fig. 4.17 characteristic transfer curves of two Ph3 devices of different channel length. The devices belong to the same substrate and they were fabricated in the glove box then exposed to air then measured in the glove box. The arrows show the direction of the current sweep considering that the linear regime (Vd=-5) is always measured before the saturation regime (Vd=-60). The two curves have the same scale.

Fig. 4.17 shows two transfer curves for Ph3 with two different channel lengths. A clear gate modulation is present, despite a strong hysteresis in the reverse sweep. However, the charge modulation starts from zero gate voltage and the hysteresis in the saturation regime become less pronounced with respect to the linear regime, as well as by going to shorter channel lengths. It is worth to point out that these devices were prepared in the glove box; then the sample was transferred in air to another glove box for the electrical measurements. Indeed, in the first trials, only one or two devices were working out of the sixteen which profoundly challenged the repeatability of the results. After several trials to find out the reason for the diversity in the results, it turned out that the device should be freshly prepared and even the solution used in the drop-casting should be freshly prepared in order to have reproducible working devices.
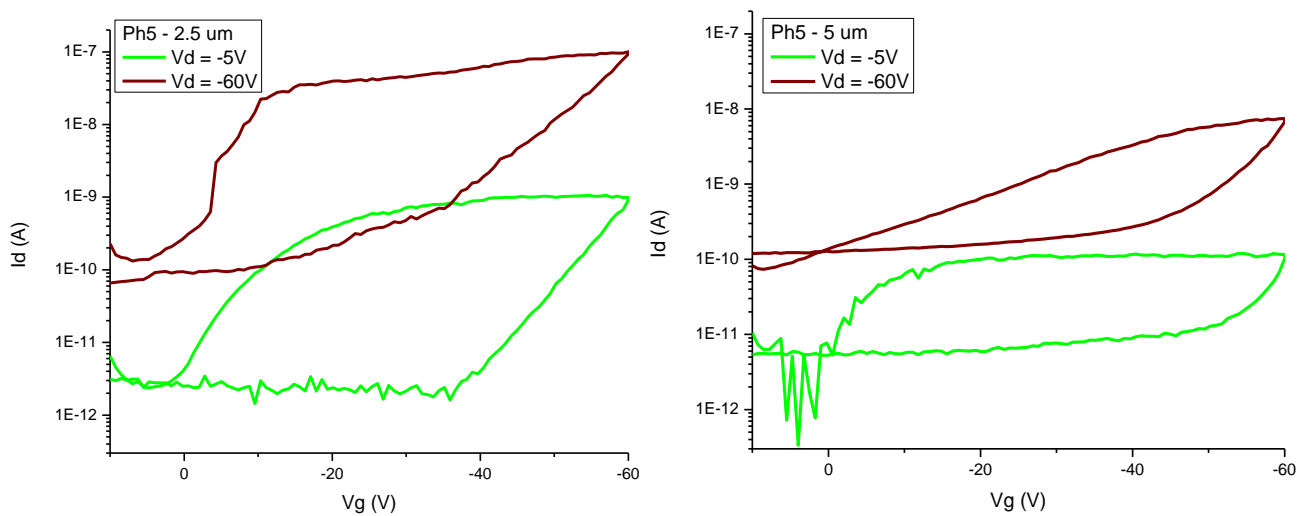
Fig. 4.18 The characteristic transfer curves of two Ph5 devices of different channel length. The devices belong to the same substrate and they were fabricated in the glove box then exposed to air then measured in the glove box. The two curves have the same scale

In Fig. 4.18 two transfer curves of Ph5 is shown with different channel lengths. These curves were obtained by the same procedure as the previous curves. As in the case of Ph3, the hysteresis cycle is pronounced for both channel lengths. However, the difference in the hysteresis between the linear regime and the saturation

regime is negligible with respect to the same case in Ph3. Another observation is that the maximum current for Ph5 is way less than its counterpart in Ph3. Moreover, the difference in the maximum current between 2.5 μm and 10 μm channel lengths in Ph3 is of the order of half an order of magnitude while the difference in the maximum current between 2.5 μm and 5 μm in Ph5 is of the order of one order of magnitude. This could be associated to the average crystal dimensions and the film morphology of Ph3 and Ph5. Indeed, the average crystal length in Ph3 is around 30 μm which is longer than the channel length with a reasonable amount and over that the film morphology in Ph3 ensures that these crystals will cross the gap between the electrodes. On the other hand, for Ph5 the average is 11 μm which is comparable to the channel length and the film morphology does not ensure that every crystal which is longer than the channel length will cross the gap, as any angle which the crystal will take will increase the gap length. This difference in the average crystal size and film morphology between Ph3 and Ph5 will put limits to channel lengths for both molecules. This being said, other phenomena could also play a role here, such as for instance an intrinsic worse charge transport of ph5 or a more severe instability during the measurements.

4.3.2   Comparison between devices prepared with PFBT and OTS self-assembled monolayers (SAMs)

After several trials, the device fabrication process was optimized. Fresh solution is used to prepare new devices which are immediately measured and no air exposure was allowed. Considering the very pronounced hysteresis occurring during the measurements and the lack of n-type operation, an OTS SAM was employed in the device fabrication. As previously demonstrated, OTS helps in eliminating the traps resulting from the SO2 dielectric that could be associated with these two issues. However, the hysteresis persisted and even with OTS, there was no n-type conductance. Another issue that we observed in the electric characteristics is the presence of pronounced contact resistance. Contact resistance may have different origins, as we discussed above a possible issue is related to the energetic matching between the semiconductor energy levels and the metal work function; therefore, we employed here a PFBT self-assembled monolayer.
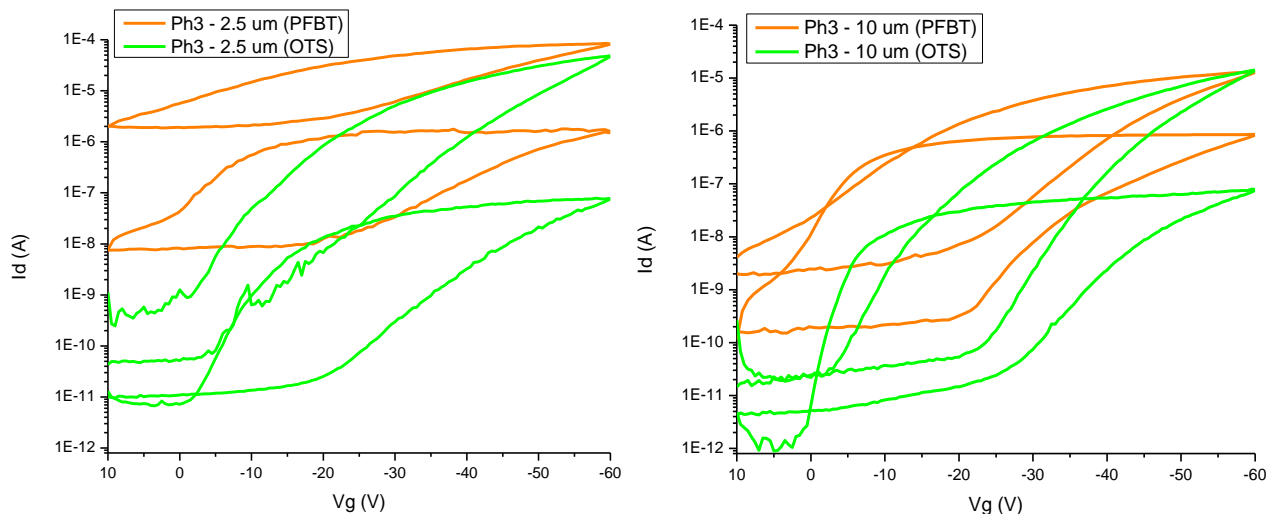
Fig. 4.19 The characteristic transfer curves comparison between devices with PFBT and devices with OTS of Ph3 of different channel lengths. The devices with the same SAM belong to the same substrate. The two curves have the same scale.

Fig. 4.19 shows the comparison between the transfer curves obtained with OTS and PFBT of Ph3 for two different channel lengths. The First observation which can be noticed is that for OTS forward curves the current modulation onset occurs at 0 V for linear regimes in both channel lengths but for the saturation regime it only starts from zero in the 2.5 μm channel length while it is slightly sifted in the 10 μm channel length. On the other hand, for PFBT, this behavior is less pronounced. This behavior can be explained in the framework of the effect of the measurement process on the formation of traps and the threshold voltage shift due to the presence of contact resistance. At first, the device is measured in the linear regime and upon moving to the

saturation regime, the device is then already affected by the first measurement process, inducing the formation of traps and the threshold voltage is then shifted forward. In the 2.5 channel length; however, this behavior is absent and here it comes the role of the contact resistance. The contact resistance tends to shift forward the threshold voltage of the linear regime than the saturation regime since the higher lateral field employed in saturation enables a better charge injection. The contact resistance, however, is dominant at short channel lengths rather than for long channel lengths. Putting these two effects together we can justify the observed behavior. Moreover, the less severity of this behavior in PFBT case is a sign on a decrease in the contact resistance in this case. The second observation is that the off current in the case of OTS is always lower than in the case of PFBT. On the other hand, the on the current of the linear regime in the case of OTS is always less than in the case of PFBT while in the saturation regime it is only lower for 2.5 μm channel length and not 10 μm channel length. This observation is another clue on the decrease of the contact resistance in the case of PFBT since the contact resistance is only not a limiting factor in the saturation regime of long channel lengths which is where the two currents (OTS and PFBT) are the same.
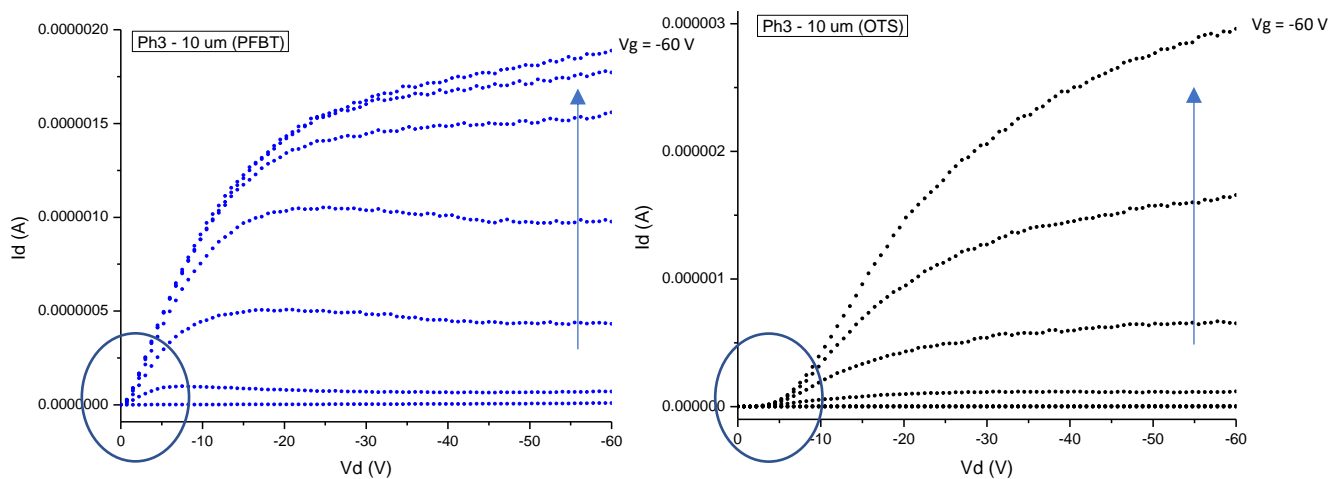
Fig. 4.20 The output curves for two Ph3 devices one with PFBT and one with OTS where the gate voltage is increased with the arrows and the circles are to identify important features of the curves. The two devices have 10 μm channel length. The two curves have different scales.

Fig. 4.20 shows the output curves for Ph3 with PFBT and OTS. For OTS, the increase in current is not linear with the gate voltage at low V_D; therefore, the injection is not ohmic. This S-shape (the circled area) is completely absent in the case of PFBT. Indeed, in the case of PFBT, an ohmic injection is present. Normally the current should increase linearly with gate voltage but since in the second sweep the current is already affected by the first sweep measurement, due to the hysteresis, then the increase in the current with gate voltage loses its linearity. Here, however, only the forward sweep is shown for simplicity. It is also worth pointing out that the drop-casting method employed in the device fabrication does not lead to uniformity and reproducibility of the crystal distribution on the substrate; therefore, a quantitative comparison between devices is not always possible.
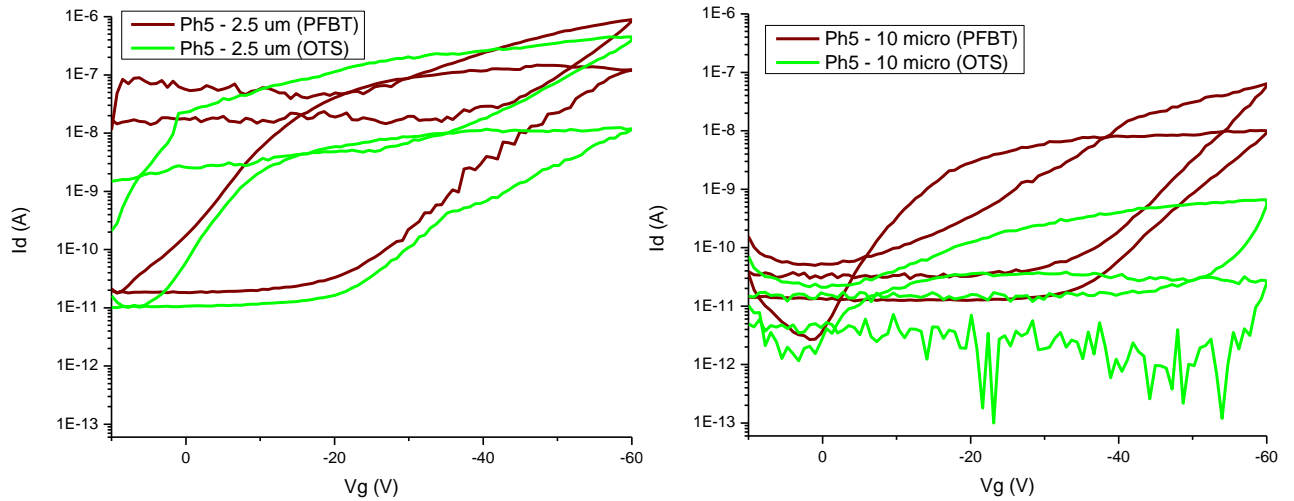
Fig. 4.21 The characteristic transfer curves comparison between devices with PFBT and devices with OTS of Ph5 of different channel lengths. The devices with the same SAM belong to the same substrate. The two curves have the same scale.

Fig. 4.21 shows the characteristic curves for Ph5 comparing PFBT and OTS for different channel lengths. The first observation is that the currents in these curves are two orders of magnitude lower than their counterpart for Ph3. Here, however, the behavior is different with respect to what has been observed with Ph3 curves. In the case of OTS with 10 μm channel length, the linear regime current is in the noise limit of the instrument and no reliable information can be deduced from this part. However, the off and on currents in both channel lengths are always lower in the case of OTS than PFBT. Nonetheless, in the case of PFBT, there is an obvious degradation during the first sweep in the linear regime, affecting consequently the forward curve of the saturation regime. Indeed, the turn-on of the device appears shifted towards negative voltage values.
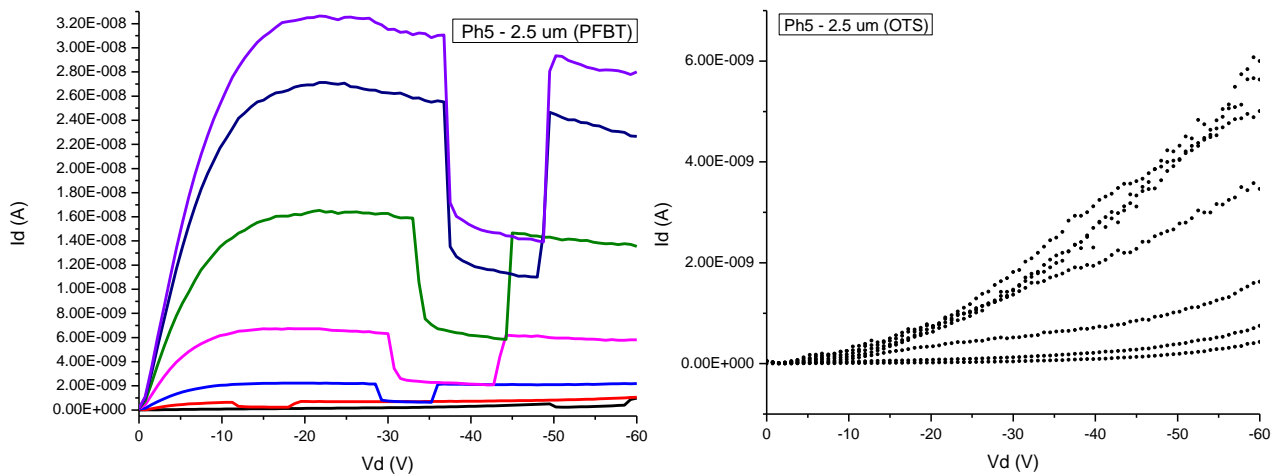
Fig. 4.22 The output curves for two Ph5 devices one with PFBT and one with OTS. The two devices have 2.5 μm channel length. The two curves have different scales.

Fig. 4.22 shows the output curves of Ph5 for both PFBT and OTS. In the case of OTS, the device is completely in the linear regime and this is a result of many factors combined like the effect of the previous measurement process, the contact resistance and the high density of traps. In the case of PFBT, the evidence of the contact resistance is absent indeed but the increase in the current with gate voltage is still nonlinear. The drops in the current in the middle of the curve are manually done by turning off the light and turning it back on which shows the effect of light on the current. A similar effect was found in the case of Ph3 as well and no further investigation was done in this area. Currents are in general lower here, again as a consequence of the degradation occurring during the measurement.

68

4.3.3 Aging

Transistors were found to stop working when it was remeasured after a couple of weeks. Even devices which were prepared and never measured until a week after did not work. After concluding that both Ph3 and Ph5 devices lose their functionality with time regardless of the measuring process, the following investigation was done.
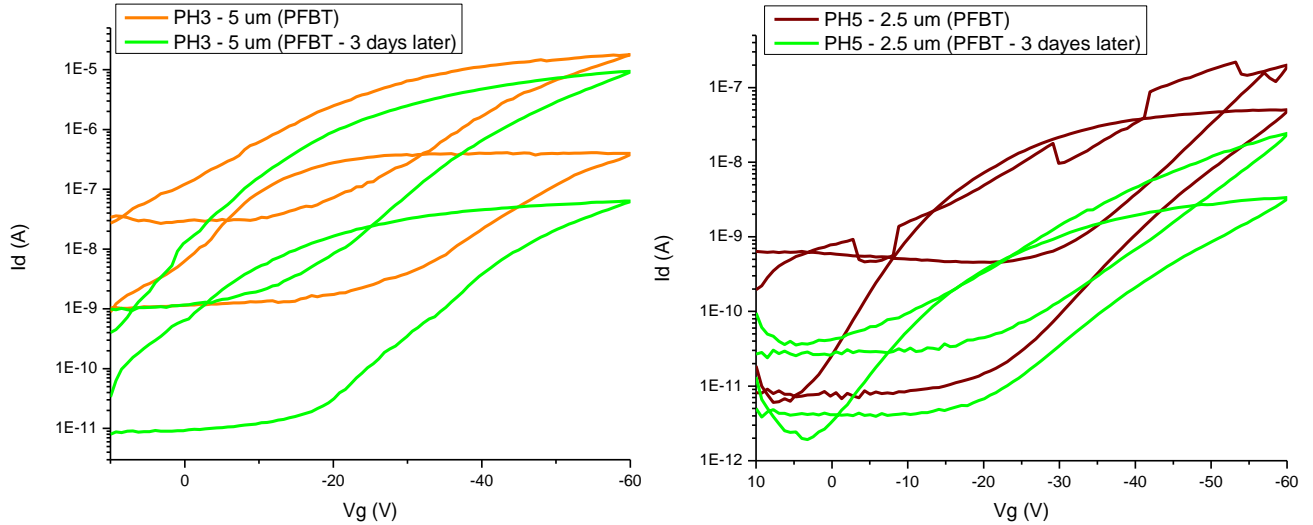
Fig. 4.23 The characteristic transfer curves of a Ph3 and a Ph5 devices which were measured after preparation and then three days later.

Fig. 4.23 shows the characteristic transfer curve of a Ph3 and a Ph5 devices which were measured after preparation and then three days later. The curves show a general decrease in the current for both Ph3 and Ph5. For Ph3 in the saturation regime, there was no noticeable effect on the mobility while in the linear regime the mobility decreased by three orders of magnitude. On the other hand, for Ph5 the mobility for both the saturation and the linear regimes decreased with one order of magnitude measuring the device after three days. However, Raman measurements were done on the device when it was working and after the loss of functionality and no trace of chemical change was observed at least from the Raman point of view. Another evidence of the absence of chemical degradation is that the molecules on the devices which are not working when re-dissolved and redeposited on fresh devices worked as good as before. The decrease of performance with time, in this case, can be attributed to the environment (water and oxygen) as that the working devices were found to stop working when measured in the air which manifests the effect of water and oxygen on the device performance.

4.3.4 Hysteresis analysis

The difference in the current between the forward and the backward sweep is proportional to the number of trapped charges due to the measurement process. These charges as was demonstrated in chapter two are trapped due to traps which are formed at high gate voltage. Thus, by running a hysteresis analysis for the linear regime and the saturation regime one could get information about the energy categories which these traps belong. The hysteresis analysis normally done by reporting the shift in the threshold voltage between the forward and the backward sweeps of the current. However, this method does not consider the difference in slope between the forward sweep current and the backward sweep current. Thus, in order to get the percentage of the trapped charges between the forward and the backward sweeps I integrated the forward and the backward currents to get the total moving charges for both according to the following relation:

$$I = \frac{dQ}{dt} \Rightarrow Q = \int I \, dt \quad (4.2)$$

Then I took the ratio of the total moving charges in the forward sweep to the backward sweep. The integration was done numerically using Origin software and no filter was applied.
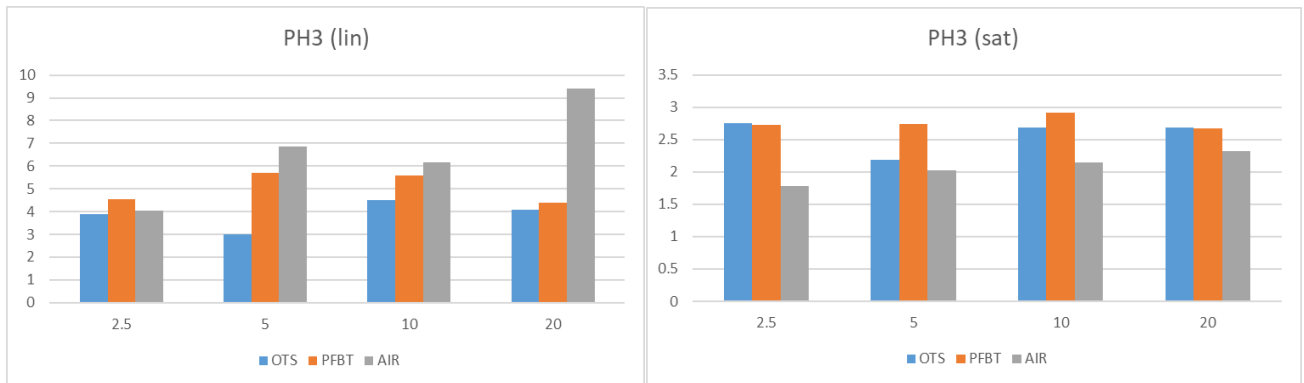
Fig. 4.24 The ratio between the total charges in the forward sweep and the backward sweep of the current in the linear and the saturation regime for Ph3 shown for different channel lengths and when using OTS, PFBT and exposing to air.

The graphs in Fig. 4.24 show the ratio between the integral of the current of the forward sweep to the backward sweep for the linear regime (left) and the saturation regime (right). The devices shown in this graph are the highest mobility devices for every channel length for OTS, PFBT and the ones which are exposed to air before the measurement. In the linear regime, the Air devices show the highest hysteresis for every channel length (the data shown in the graphs are for the highest mobility devices however the observations which will be listed are true for all the other devices which are not shown as well). On the other hand, the OTS devices show the least hysteresis in the linear regime. For the saturation regime, the Air devices show the least hysteresis while there is no pattern noticed for OTS and PFBT in this case. We can divide the traps which cause the hysteresis into shallow traps and deep traps based on whether the traps are formed in the linear regime or the saturation regime. Adapting this classification, one possible justification is that exposing to air increases the shallow traps while decreases the deep traps. The traps we are talking about in this case are most likely surface traps which are accessible only at high gate voltages. My interpretation is that exposing to air leads to oxygen accumulation on the far surface of the semiconductor which acts as a far surface traps (surface traps can be classified into far-surface and near-surface traps with respect to the dielectric layer). This kind of traps is indeed accessible at high gate voltages. By applying a gate voltage, the Fermi energy of the semiconductor starts to bend at the interface with the dielectric. At high gate voltages, this modulation in the Fermi energy reaches the other side of the semiconductor and gets affected by the far surface traps. However, the measuring process seems to provoke oxygen diffusion into the semiconductor which in this case becomes a dopant instead of a trap. This interpretation is supported by analyzing the transfer curve for the Air devices. Looking at the transfer curves in Fig. 4.17 one can notice how the backward current in the 2.5 µm does not go back to the off current value but it goes back instead to a much higher value which is a sign of oxygen doping (doping increases the off current). This effect is not present in 10 µm curves; nonetheless, the hysteresis is severely decreased in the saturation regime. Indeed, this behavior is expected since by increasing the channel length the doping percentage decreases and the doping process becomes less effective. For the OTS it seems that it reduces some shallow traps which are overcome by increasing the drain current, that explains why the OTS effect on the hysteresis disappears in the saturation regime.
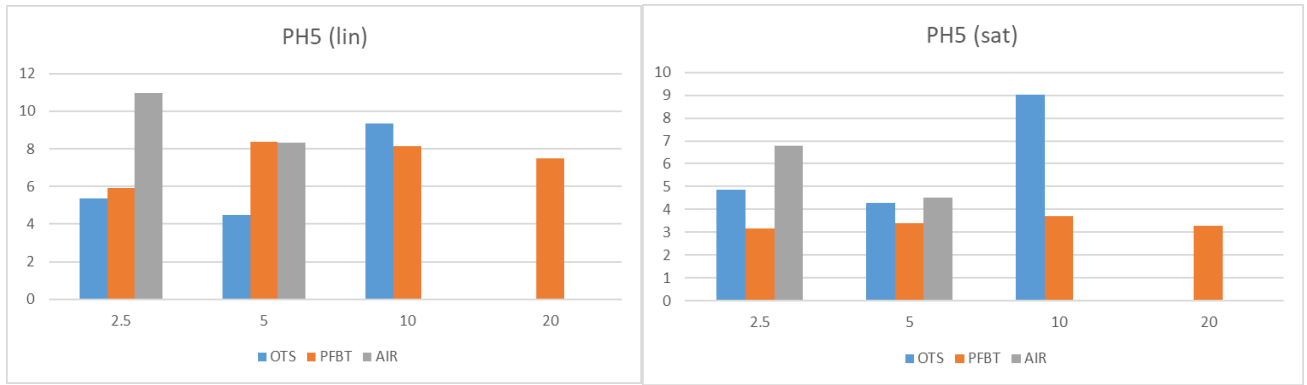
Fig. 4.25 The ratio between the total charges in the forward sweep and the backward sweep of the current in the linear and the saturation regime for Ph5 shown for different channel lengths and when using OTS, PFBT and exposing to air.

Fig. 4.25 shows the same comparison for Ph5 and since for long channel lengths, Ph5 morphology does not ensure closing the gap as was previously demonstrated, only data for the devices of 2.5 and 5 μm channel lengths are reliable in terms of information deduction. However, there is no obvious pattern in the hysteresis process as it was the case in Ph3. This absence of the order in the data may be attributed to the low number of variables to be compared (only 2.5 and 5 μm channel lengths).
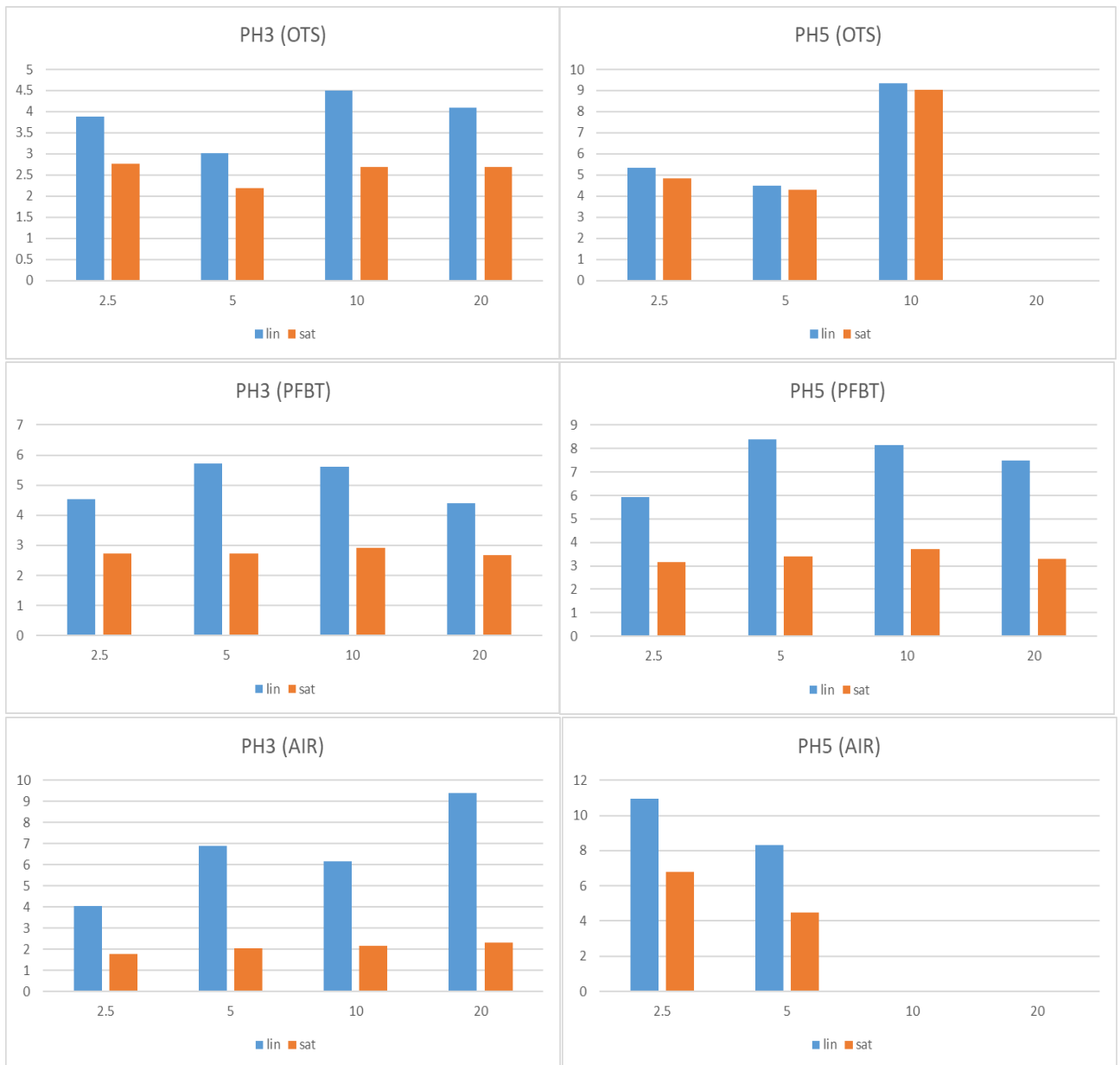
Fig. 4.26 Comparison between hysteresis (represented by The ratio between the total charges in the forward sweep and the backward sweep of the current on the vertical axis) in saturation and linear regimes for different channel lengths in different conditions.

Fig. 4.26 shows the comparison between the linear and saturation regimes hysteresis for each of OTS, PFBT and Air devices. In all the data the linear regime hysteresis is always higher than the saturation regime hysterics and this is expected indeed since in the linear regime deep and shallow traps play a role while in the saturation regime only deep traps are involved. Thus, by analyzing the difference between the linear hysteresis and the saturation hysteresis one can get an idea about the ratio of the deep traps to the shallow traps in the material. We can notice that generally going from OTS to PFBT to Air the difference in hysteresis between the linear and the saturation regimes increases. The low difference between the linear and the saturation hysteresis noticed in the case of OTS can be understood in the framework of what was previously noticed that OTS helps in decreasing the shallow traps. However, for Ph5 the difference in hysteresis between linear and saturation regimes is the least although the general hysteresis for both is relatively high. This situation suggests that most of the traps in Ph5 are deep traps and with OTS removing some shallow traps the hysteresis remains high only due to the deep traps which behave the same in linear and saturation regimes.

It is worth mentioning that in this argument I used a different definition for deep and shallow traps than their normal definitions. The traps are localized states in the band gap of the semiconductor. When these states are in the middle of the band gap, they are called deep traps while if these states were close to the HOMO or the LUMO they are called shallow traps. In my description, I used the term deep traps for the traps that cannot be overcome by the high drain voltage in the saturation regime while the shallow traps those which affect the current at low drain voltage in the linear regime and their effect disappears in the saturation regime.

4.3.5   Mobility analysis

As was demonstrated in chapter two the field effect mobility shows a dependence on the gate voltage. Analyzing this dependence reveals valuable information about the semiconductor and the device. In this subsection, the mobility dependence on the gate voltage will be analyzed and then the maximum mobility in the curve will be adapted as the device mobility. Unlike the case of the dependence of mobility on the gate voltage, the mobility should not depend on the channel length. However, in most cases, this is not true and analyzing the behavior of mobility with respect to different channel lengths again can reveal valuable information about the nature of conduction processes. Another parameter that ideally the mobility should not depend on is the drain voltage; in other words, the saturation and the linear mobility should be equal. However again this does not happen in most cases and by monitoring the differences more understanding of the nature of conduction in the material can be achieved. It is worth mentioning that the crystal formation on each device was different; therefore, a quantitative comparison between devices is not fully possible. Nonetheless, the following observations are noticed in most of the devices of the same conditions.
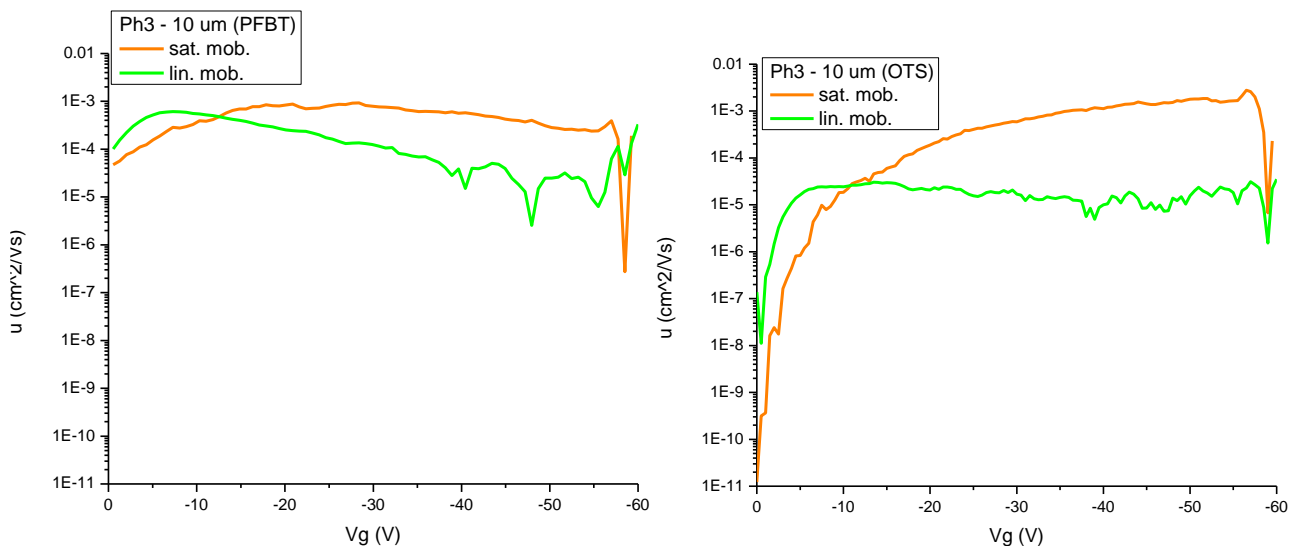
Fig. 4.27 Ph3 mobility as a function of gate voltage for the linear and the saturation regimes with PFBT (left) and OTS (right).

Fig. 4.27 shows the linear and saturation mobility relation with the gate voltage for Ph3 with PFBT and OTS. By looking at the two curves, we can immediately realize that the one for PFBT is the closest to ideality. For PFBT the difference between the linear and the saturation mobility is not pronounced and the mobility in both regimes slightly decreases by increasing the gate voltage which is normal behavior as was previously demonstrated. However, the linear mobility is still slightly lower, and its maximum is at a low gate voltage (-5 V in this case) while the saturation mobility is almost flat nonetheless its maximum is close to the middle of the curve (-27 V in this case). On the other hand, in the case of OTS, the linear mobility is nearly constant with the gate voltage while the saturation mobility increases with the gate voltage. This behavior can be justified in the framework of the contact resistance. For the linear mobility, the increase in the gate voltage has a little effect on the charge injection and by increasing the charge density in the conduction channel traps are created and the mobility decreases which is the case in PFBT. On the other hand, in the case of OTS, this little decrease

in mobility with increasing the gate voltage is compensated by a little improvement in the charge injection giving rise to almost constant mobility with respect to the gate voltage. Moving to the saturation regime, by increasing the gate voltage, the barrier for the charge injection is decreased leading to an increase in the overall mobility of the device. However, the contact resistance, in this case, is not a limiting factor for the mobility, since the same mobility is reached even though it was at high gate voltage. For PFBT the absence of this behavior is evidence on the reduced contact resistance which indeed was the aim of applying the PFBT SAM at the first place.
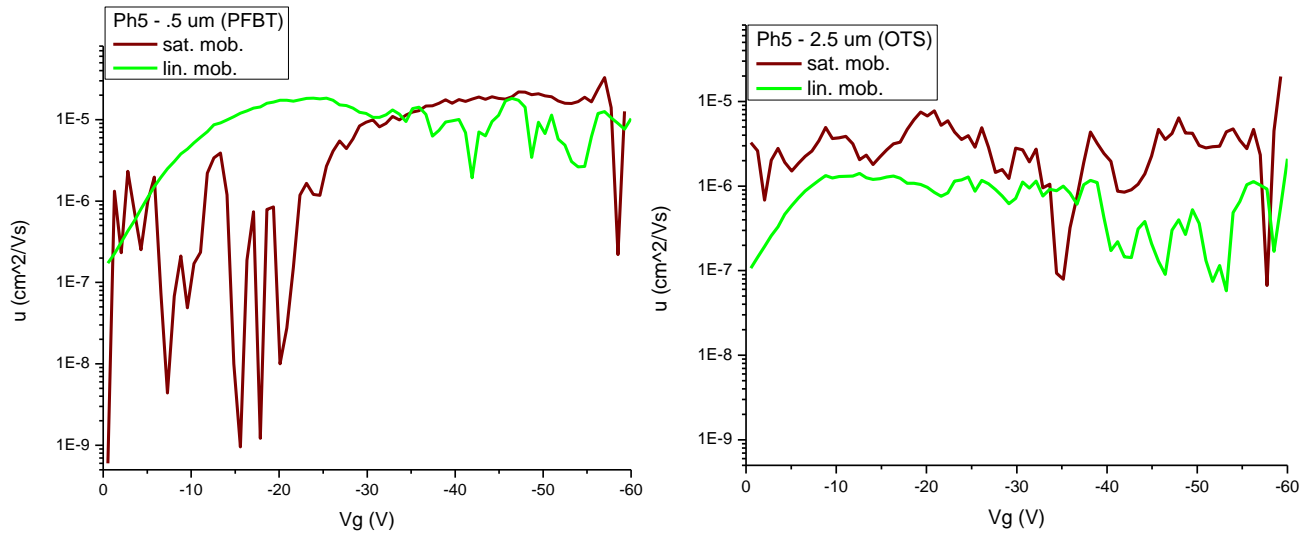
Fig. 4.28 Ph5 mobility as a function of gate voltage for the linear and the saturation regimes with PFBT (left) and OTS (right).

Fig. 4.28 shows the mobility relation with the gate voltage for Ph5 with PFBT and OTS. We can notice that the overall noise in the curves is higher than the case with Ph3 and that is because the currents here are around one order of magnitude less than in Ph3 case and with low current the noise increases (notice with Ph3 curves the channel length was 10 μm while here it is 2.5 um). Regardless of the noise, one can notice that the linear regime mobilities in both cases show a maximum at low gate voltage and slightly decrease after that. On the other hand, the saturation regime mobility in the case of PFBT increases with increasing gate voltage while in the case of OTS its maximum is at Vg = -18 V although it can be approximated as constant with the gate voltage. In Ph5 generally, we can say that the contact resistance does not play a role in the conduction process and this can be understood in the framework of the alignment between the work function of the electrodes and the HOMO in Ph5. This is consistent with the difference in energy gap between Ph3 and Ph5 where without external factors Ph3 can be expected to show higher contact resistance than Ph5. Indeed, by applying PFBT, one can think that the energy difference between the levels of the electrodes and Ph3 decreased and so the contact resistance. However, in the case of Ph5 since it had low contact resistance already, applying the PFBT did not improve much at this point. Nonetheless, the devices with PFBT for Ph5 showed much better performance than without PFBT. On the light of this analysis, we can assume that the increase of the mobility with the gate voltage in PFBT case in the saturation regime is of different origin than the contact resistance. One can think of deep traps which are filled with increasing the gate voltage as was demonstrated in chapter two. On the other hand, the absence of this behavior in the case of OTS is simply because the current is much lower in the case of OTS than PFBT and there is not enough current to manifest the effect of the gate voltage on mobility. In other words, the behavior was hidden by the low current and upon measurement, the device degrades; therefore, the mobility extraction will not be precise.
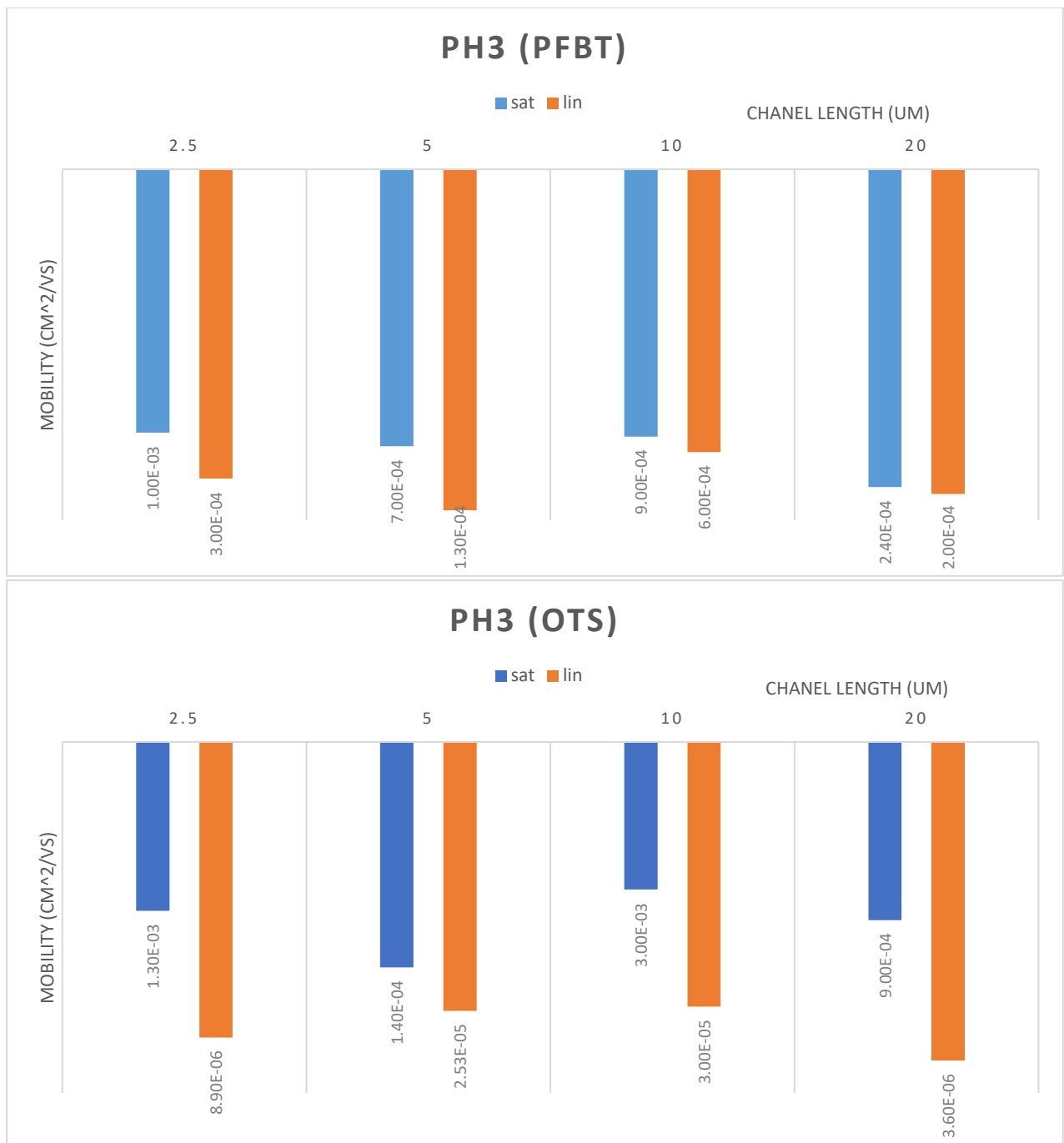
Fig. 4.29 Maximum mobilities achieved for Ph3 with PFBT and OTS for each channel length.

Fig. 4.29 shows a diagram of the maximum mobilities obtained for Ph3 in different conditions (PFBT and OTS for different channel lengths). The maximum mobility out of them is $3*10^{-3}$ cm^2/Vs which is obtained in the saturation regime using OTS at 10 μm channel length. However, all the saturation mobilities for OTS and PFBT are in the same range of values. Although the saturation mobility is always higher than the linear mobility in both OTS and PFBT cases but the difference in the case of OTS is much higher than that of PFBT. Indeed, the linear mobility in the case of OTS is around two orders of magnitude less than the saturation mobility while in the case of PFBT it is of the same order of magnitude. This behavior again can be justified in the framework of the contact resistance which is only a limiting factor at the linear regime.
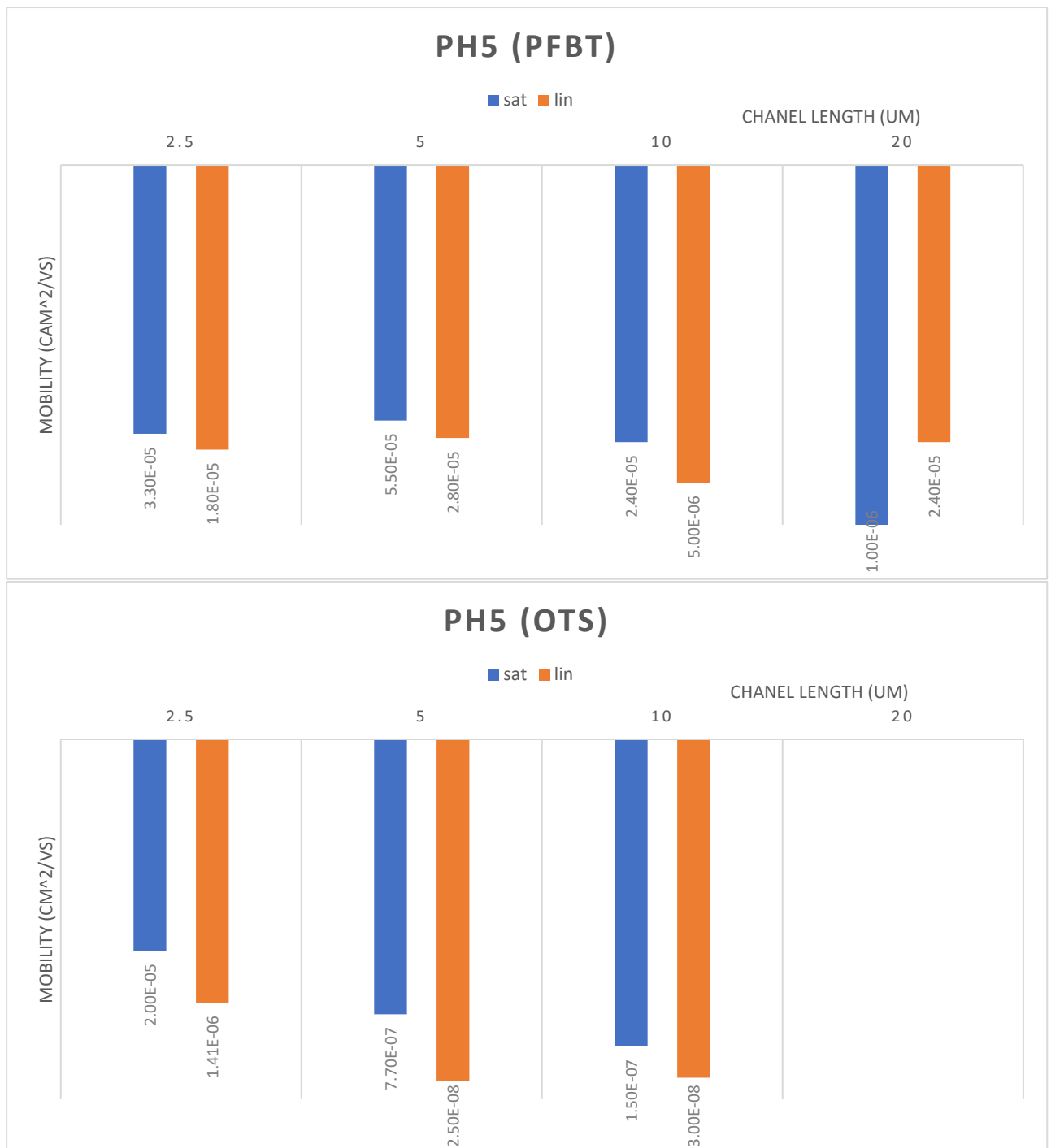
Fig. 4.30 Maximum mobilities achieved for Ph5 with PFBT and OTS for each channel length.

Fig. 4.30 shows the maximum mobilities recorded for Ph5 in different conditions. The maximum mobility out of them is $3.3*10^{-5}$ cm^2/Vs which is obtained in the saturation regime using PFBT at 2.5 µm channel length. As in the case of Ph3 the saturation mobilities are always higher than the linear mobilities. However, in this case, the differences are relatively small. Nonetheless, in the case of PFBT, the differences are smaller than in the case of OTS. This behavior can be understood thinking of deep traps which are dominating the transport and the low contact resistance effect. The low contact resistance effect sneaks into the results through the little difference between PFBT and OTS in terms of the difference between the saturation and linear mobilities.

Finally, it is important to notice that these mobility values were obtained under the assumption that each device is fully covered and all the area between the electrodes contribute to the current. However, the average

coverage of a device as was calculated is 30% with variations from 10% to 50% which means that the mobility values must be corrected on the bases of these values. Thus, an approximate corrected maximum value of mobility for Ph3 is $1*10^{-2}$ cm^2/Vs instead of $3*10^{-3}$ cm^2/Vs and the maximum mobility for Ph5 is $1.1*10^{-4}$ cm^2/Vs instead of $3.3*10^{-5}$ cm^2/Vs. The calculated average device coverage was done by image analysis assuming that the covered area fully contributes to the current which is a wrong assumption. However, this assumption was not relaxed due to the difficulty of calculating the real area contributing to the conduction process (in transistors the conduction occurs at the dielectric interface which requires a full contact between the semiconductor and the dielectric otherwise there will be no conduction).

4.3.6   Conclusions and discussion

The first conclusion is that field effect transistor with sp-carbon atomic chains-based molecules of the cumulenic type was measured, which is the first report of this kind, to the best of our knowledge. Starting from the realization of the field effect in both Ph3 and Ph5 molecules which are cumulenic type molecules and the absence of the effect in DPA and DPB molecules which are a polyynic type, one can conclude that, in this case, the cumulenic structure is needed for the field effect to be realized. In chapter one, I have reported the work of A. Milani et al. showing that polyynic molecules with phenyl groups show a decrease in their BLA when interacting with silver nanoparticles as a charge transfer process occur. On the other hand, in the work done on the polyynic molecules (see Fig. 2.16), it was demonstrated that electron donor groups are needed for the field effect to be realized in the investigated polyynic molecules. Putting things together one can realize that the electron donors might have caused a decrease in the BLA and induced conjugation this can be a possible explanation although it still to be demonstrated.

Another conclusion of the work is that Ph3 devices show higher mobility than Ph5 devices in the framework of the experimental configuration adapted. From the first sight, this result seems counterintuitive if only the energy gaps for the two molecules were considered. However, since FETs comprising a cumulenic type of molecules have never been measured, further measurements are needed to investigate the charge transport mechanisms of these molecules and establish intrinsic structure-property relationships. We can speculate here a few possible interpretations to describe the differences in the field effect transistors measured in this work for Ph3 and Ph5. However, it is worth mentioning that the measured mobilities are the devices' mobilities not the intrinsic mobilities of the molecular crystals used in the devices.

Starting from the XRD data, it seems that no big difference between Ph3 and Ph5 although Ph5 has a slight advantage in steric hindrance and intermolecular distances. Thus, if Ph3 has an advantage in conduction it is most likely will be not because of the transfer integral. Moving to the film morphology and crystals dimensions for both molecules, Ph3 has an advantage in terms of the average crystalline domain size, on the other hand, the difference in the film wettability of the surface cannot be identified for both molecules with the given data.

Moreover, it is important to recall the transport properties which were observed through the results. As was demonstrated Ph3 and Ph5 both have traps which significantly affect their transport behavior. These traps were classified into deep traps and shallow traps, each of which shows two different behaviors. On the other hand, it was shown that both Ph3 and Ph5 have contact resistances but Ph3 has higher contact resistance than Ph5. It seems from these observations that the deeper traps in Ph5 are responsible for its lower charge mobility.

The traps can be from an intrinsic origin as was demonstrated in chapter two or it can be due to the defects and impurities in the crystal itself, at the grain boundaries or at the interface with the dielectric. The crystal dimension and hence the lack of interconnection between source and drain could be one of the reasons behind the difference in current and hence in charge mobility between Ph3 and Ph5. It is well established for organic semiconductors that beside structural properties of the material, the interconnectivity between

crystallites plays a crucial role in the charge transport. Nonetheless, we can have an idea about the charge self-trapping in the molecules by looking at the effect of the charge on the vibrational frequencies of the molecules as was demonstrated in chapter two. Indeed, the effect of an excess charge added to the isolated molecule on its Raman spectrum was calculated by A. Milani. Although no experimental validation was done but insightful information can still be deduced.
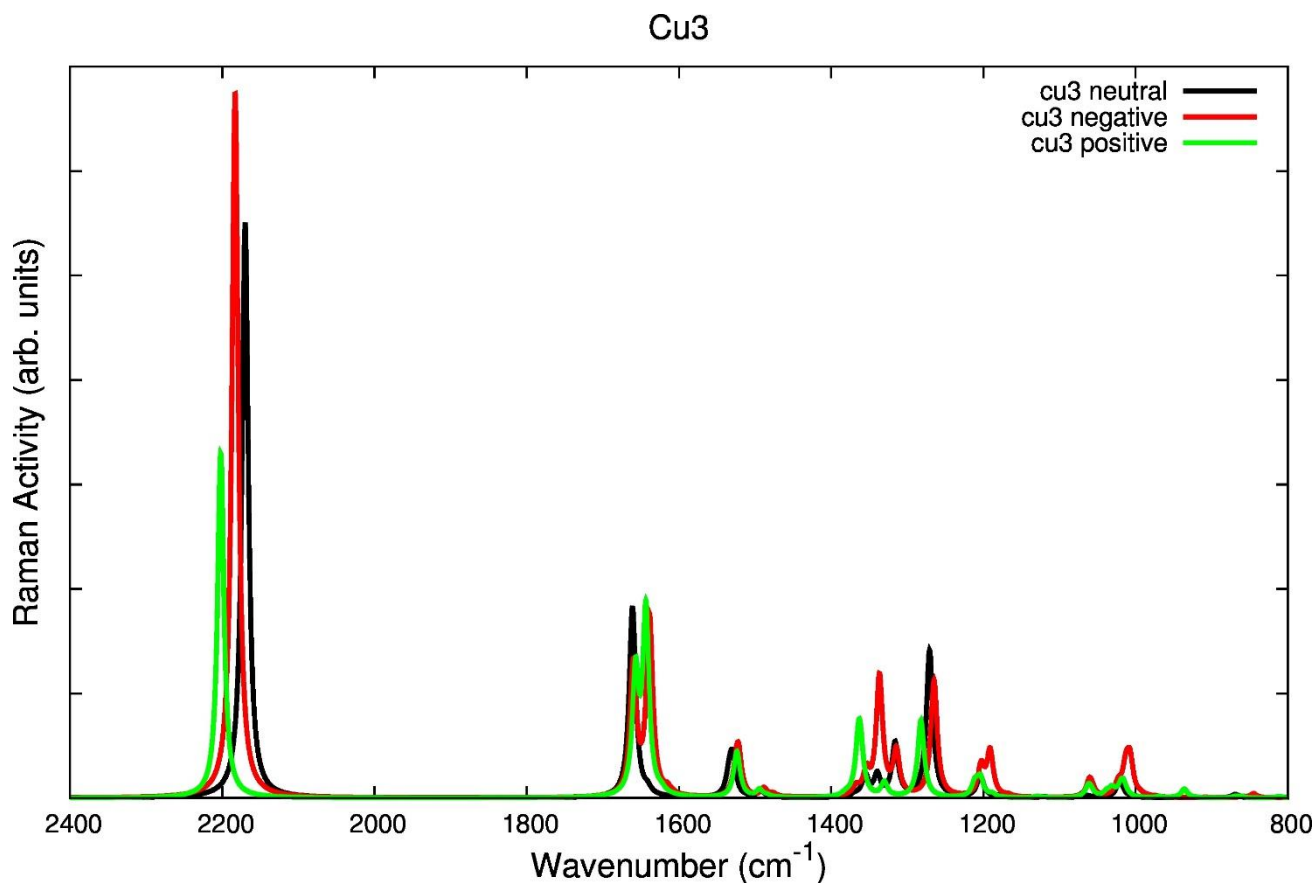
Fig. 4.31 DFT calculated Raman spectra for Ph3 isolated molecule in a neutral state, positively charged state and negatively charges state. (the calculations were done by A. Milani)

Fig. 4.31 shows the Raman spectra of Ph3 calculated for the neutral, positively charged and negatively charged isolated molecule. By looking at the spectra, one can immediately see that the charge is located on the sp^2-carbon region since all the peaks are blueshifted except the sp^2-carbon peak in the region 1600 to 1700 cm^{-1} which is redshifted (carrier induced softening effect). Moreover, the excess charge caused a split in the sp^2 peak which might be a sign that the charge is more oriented towards one phenyl group than the other.
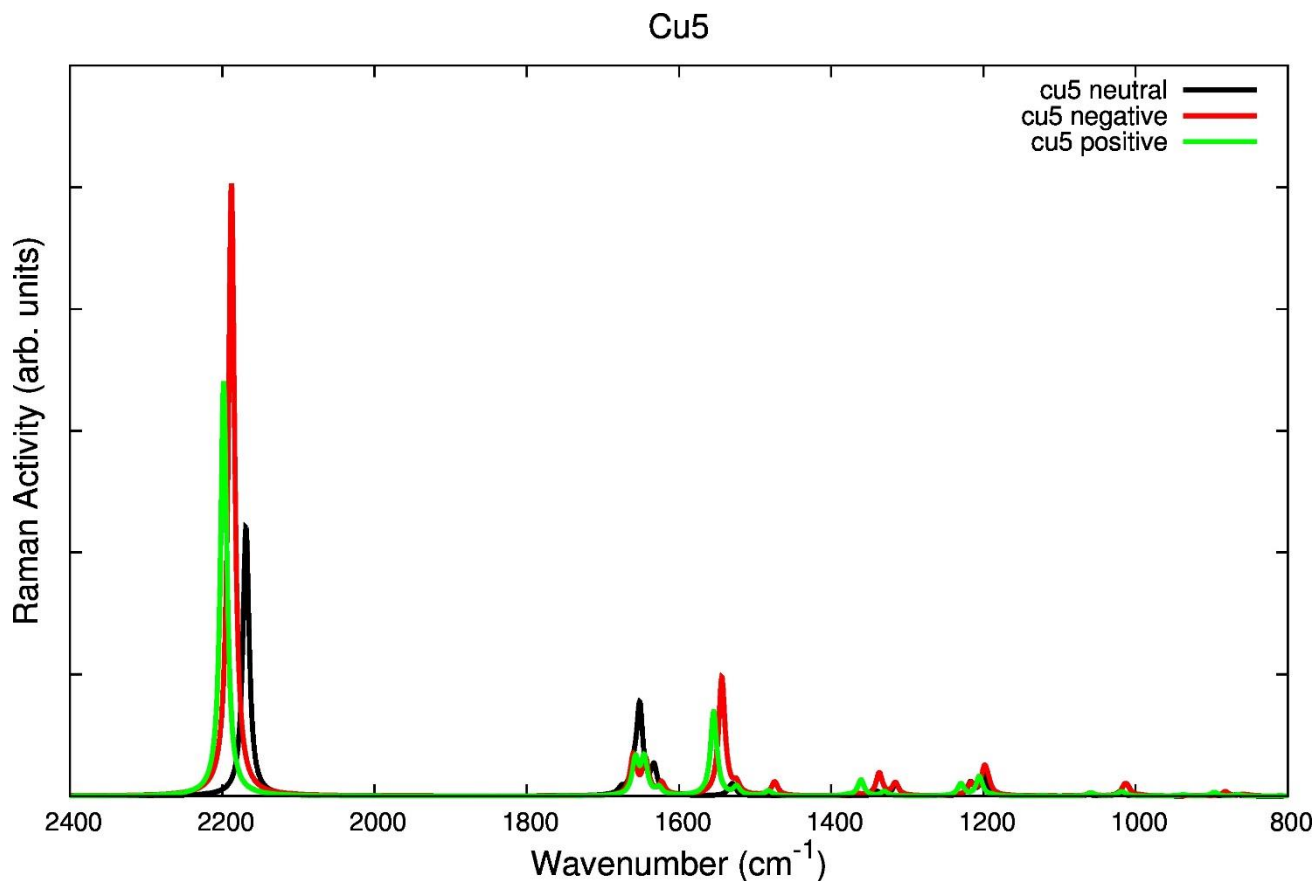
Fig. 4.32 DFT calculated Raman spectra for Ph5 isolated molecule in a neutral state, positively charged state and negatively charges state. (the calculations were done by A. Milani)

In Fig. 4.32 the same calculations for Ph5 is shown and again it is clear that the charge is in the sp^2 region. However, the charge this time shows a different effect on the sp^2 peak. As was previously shown that in neutral Ph5 molecule the sp^2 peak was already split indicating a different environment for both phenyl groups. However, the peak intensities were different for the two split peaks and here the presence of an excess charge equalized their intensities. This effect can be thought off as that the charge equalized the orientation of the phenyl groups with respect to the Raman laser so that they show the same Raman intensity.

On the bases of these calculations (which is not experimentally verified yet), I can assume that the excess charge on each molecule is located on the phenyl groups. By comparing the two graphs (of Ph3 and Ph5) I can suggest that the charge carrier is more confined on Ph5 than Ph3 molecule which is because of the higher Raman shift which is caused by the charge at Ph3 than Ph5 (this was explained in chapter two in the subsection "molecular polarons"). This localization might be the reason for the deeper traps in Ph5 than Ph3 which was reflected on their mobilities if the mobility of Ph3 was really higher than that of Ph5 and to confirm more investigations are needed.

The previous observation is a simple way to describe a complex transport process in Ph3 and Ph5 and most likely that it is more than one factor combined to give a collective behavior that was observed in the results. However, this simple model provides a good picture of what is happening in the material. Moreover, it provides a better rule of thumb to predict the performance of new material in the field of field effect transistors. The first thoughts when designing a new molecule for electronics is to increase the conjugation of the molecule. However, thinking of the behavior of the charged molecule instead of the neutral molecule can give more accurate predictions of the electronic properties. In this sense, Raman calculations are of great benefit in this area and the previous calculations is an excellent example for that. Information about the charge

carrier presence in the molecule and the effect of this charge carrier on the molecular vibrations and even the atomic equilibrium position shifts can be deduced from the Raman spectrum.

5 Conclusion and future work

The main objective of this work was to obtain information about the charge transport of the four investigated molecules in their crystalline form and conclude a comparative study which can reveille the difference in electrical transport properties in response to the little change in the molecular structure. Indeed, electrical conductivity measurements were done on the four molecules and their I-V currents were obtained. The cumulenic molecules showed higher current in general than the polyynic molecules which emphasizes the effect of the BLA on the conduction of the molecular crystals. However, for the polyynic type molecules, the longer chain molecule showed higher currents than the shorter one which shows that for polyynic type molecular crystals the conduction increases with increasing the chain length. On the other hand, for the cumulenic type molecules, the Ph3 (which is the shorter molecule) showed higher currents than Ph5 (the longer molecule). However, we cannot conclude that the length of the chain, in this case, was the reason for this difference in the conduction since both molecules showed different morphologies when deposited.

A step further was taken by using the molecules as a field effect transistor's active medium. The polyynic molecules failed to show any current modulation after several attempts were done. On the other hand, field effect transistors were successfully fabricated and characterized using the cumulenic type molecules. Pre-purchased Fraunhofer substrate was used for the measurements which is a substrate specifically designed for organic field effect transistors characterization. The substrate has gold electrodes and SiO_2 as a dielectric insulator layer. Self-assembled monolayers were used with the devices in order to improve the performance and decrease the extrinsic effects on them. OTS SAM on SiO_2 surface was used to eliminate the surface traps and to allow the n-type current measurements of the molecules as SiO_2 is known to create surface traps and block n-type conduction. PFBT SAM was used on the electrodes gold surface in order to decrease the contact resistance. The two SAMs where used on different devices and their results were compared. By comparing different devices with different conditions, these properties of the molecular crystals were found. Ph3 showed maximum field effect mobility of $1*10^{-2}$ cm^2/Vs while Ph3 showed a maximum field effect mobility of $1.1*10^{-4}$ cm^2/Vs. Ph3 was found to have some contact resistance and by using PFBT, the contact resistance was successfully reduced. Both molecules showed a hysteresis cycle in their devices and the application of OTS seemed to slightly improve the hysteresis only in the linear regime. Both molecules' devices appeared to be affected by the measurement process but this phenomenon was more pronounced in Ph5. The deeper traps in Ph5 than Ph3 seemed to be responsible for the difference in mobility between the two materials.

Furthermore, Raman spectroscopy was used to check the stability of the molecules with time, atmosphere exposure and after and before the measurement process. All four molecules showed stability in all conditions. Another use of Raman (with polarized light) was to identify the alignment of the molecules with respect to the crystal-growth direction which was found to be perpendicular (only Ph3 was investigated). Moreover, UV-Vis absorption and reflection spectra of Ph3 and Ph5 were obtained. Ph5 showed an absorption starts from 600 nm wavelength while Ph3 absorption starts from 500 nm wavelength showing a higher optical band gap for Ph3 than Ph5. However, these values are for solid state films obtained using drop casting which is redshifted with respect to the spectra obtained in solution form. Another observation was that the start of absorption of Ph5 gets redshifted with changing the deposition technique from spin coating to drop casting while Ph3 absorption did not show any shift. Finally, the deposited films were analyzed using an optical microscope and scanning electron microscope image analysis where average crystal dimensions were obtained for Ph3 and Ph5 molecular crystals. It is worth mentioning that it was realized that visible light increases the conductivity of both Ph3 and Ph5 crystals but no further investigations were done in this area.

To take this work a step further, one could investigate the effect of light which was reported in this work. Another important parameter to be investigated is the mobility dependence on the temperature where the activation energy can be calculated. Furthermore, theoretical simulations for Ph3 and Ph5 could be an insightful tool for understanding their charge transport mechanisms in order to have a complete picture. As I previously mentioned this work can be considered a milestone and introducing more sp-carbon chains-based molecules and structures to the field of field effect transistors is indeed a very promising topic. On the other hand, synthesis of new molecules, keeping in mind the electronic and vibrational properties of the molecule, when an excess charge is added or removed of the molecule can speed up the understanding of the overall behavior of organic semiconductors. Finally, theoretical calculations can be a crucial forecasting tool in this area

References

[1] Hirsch, Andreas, "The era of carbon allotropes," *Nature Materials,* vol. 9, pp. 868-871, 2010.

[2] C.S. Casari and A. Milani, "Carbyne: from the elusive allotrope to stable carbon atom wires," *MRS Communications,* vol. 8, pp. 207-219, 2018.

[3] H. W. Kroto, J. R. Heath, S. C. O'Brien, R. F. Curl & R. E. Smalley, "Smalley: C60: buckminsterfullerene.," *Nature,* vol. 318, p. 162–163, 1985.

[4] Pavel B. Sorokin, Hoonkyung Lee, Lyubov Yu. Antipina, Abhishek K. Singh, and Boris I. Yakobson, "Calcium-decorated carbyne networks as hydrogen storage media," *Nano Lett.,* vol. 11, p. 2660–2665, 2011.

[5] Mingjie Liu, Vasilii I. Artyukhov, Hoonkyung Lee, Fangbo Xu, and Boris I. Yakobson, "Carbyne from first principles: chain of C atoms, a nanorod or a nanorope," *ACS Nano,* vol. 7, p. 10075–10082, 2013.

[6] Lin, Mingchao Wang & Shangchao, "Ballistic Thermal Transport in Carbyne and Cumulene with Micron-Scale Spectral Acoustic Phonon Mean Free Path," *Scientific Reports,* vol. 5, p. 18122 , 2015.

[7] C. S. Casari, M. Tommasini, R. R. Tykwinskic and A. Milani, "Carbon-atom wires: 1-D systems with tunable properties," *Nanoscale,* vol. 8, pp. 4414-4435 , 2016.

[8] Alberto Milani, Matteo Tommasini, Mirella Del Zoppo, Chiara Castiglioni, and Giuseppe Zerbi, "Carbon nanowires: Phonon and π-electron confinement," *Phys. Rev. B,* vol. 74, p. 153418, 2006.

[9] Alberto Milania, Matteo Tommasini, and Giuseppe Zerbi, "Carbynes phonons: A tight binding force field," *J. Chem. Phys,* vol. 128, p. 064501, 2008.

[10] Shujiang Yang, and Miklos Kertesz, "Linear Cn Clusters: Are They Acetylenic or Cumulenic?," *J. Phys. Chem. A,* vol. 112, p. 146–151, 2008.

[11] Tykwinski, Johanna A. Januszewski Dominik Wendinger Christian D. Methfessel Dr. Frank Hampel Prof. Rik R., "Synthesis and Structure of Tetraarylcumulenes: Characterization of Bond-Length Alternation versus Molecule Length," *Angew. Chem.,* vol. 52, pp. 1817-1821, 2013.

[12] Tykwinski, Johanna A. Januszewskia and Rik R., "Synthesis and properties of long [n]cumulenes (n ≥ 5)," *Chemical Society Reviews,* vol. 43, pp. 3184-3203 , 2014.

[13] Alberto Milani, Matteo Tommasini, Valeria Russo, Andrea Li Bassi, Andrea Lucotti, Franco Cataldo and Carlo S. Casari, "Raman spectroscopy as a tool to investigate the structure and electronic properties of carbon-atom wires," *Beilstein J. Nanotechnol.,* vol. 6, p. 480–491, 2015.

[14] Zhao X, Ando Y, Liu Y, Jinno M, Suzuki T, "Carbon nanowire made of a long linear carbon chain inserted inside a multiwalled carbon nanotube.," *Phys Rev Lett.,* vol. 90, p. 187401, 2003.

[15] Bettini LG, Della Foglia F, Piseri P, Milani P., "Interfacial properties of a carbyne-rich nanostructured carbon thin film in ionic liquid.," *Nanotechnology,* vol. 27, p. 115403, 2016.

[16] C. S. Casari, V. Russo, A. Li Bassi, and C. E. Bottani, "Stabilization of linear carbon structures in a solid Ag nanoparticle assembly," *Appl. Phys. Lett.,* vol. 90, p. 10.1063/1.2430676, 2007.

[17] Tykwinski, Wesley A. Chalifoux & Rik R., "Synthesis of polyynes to model the sp-carbon allotrope carbyne," *Nature Chemistry,* vol. 2, p. 967–971, 2010.

[18] Franco Cataldo, Ornella Ursini, Alberto Milani, Carlo S.Casari, "One-pot synthesis and characterization of polyynes end-capped by biphenyl groups (α,ω-biphenylpolyynes)," *Carbon,* vol. 126, pp. 232-240, 2017.

[19] Francesco Innocenti, Alberto Milani, Chiara Castiglioni, "Can Raman spectroscopy detect cumulenic structures of linear carbon chains?," *Raman spectroscopy,* vol. 41, pp. 226-236, 2009.

[20] "photochemistry wordpress," [Online]. Available: https://photochemistry.wordpress.com/2009/08/24/light-absorption-and-fate-of-excited-state/.

[21] Johanna A. Januszewski, Dominik Wendinger, Christian D. Methfessel, Frank Hampel, and Rik R. Tykwinski, "Synthesis and Structure of Tetraarylcumulenes: Characterization of Bond-Length Alternation versus Molecule Length," *Angew. Chem.,* vol. 52, pp. 1817-1821, 2013.

[22] N. D. Lang and Ph. Avouris, "Oscillatory Conductance of Carbon-Atom Wires," *PHYSICAL REVIEW LETTERS,* vol. 81, pp. 3515-3518, 1998.

[23] N. D. Lang and Ph. Avouris, "Carbon-Atom Wires: Charge-Transfer Doping, Voltage Drop, and the Effect of Distortions," *Phys Rev Lett.,* vol. 84, pp. 358-61, 2000.

[24] A. Milani, V. Barbieri, A. Facibeni, V. Russo, A. Li Bassi, A. Lucotti, M. Tommasini, M. D. Tzirakis, F. Diederich & C. S. Casari, "Structure modulated charge transfer in carbon atomic wires," *Scientific Reports,* vol. 9, p. 1648 , 2019.

[25] Renato Batista dos Santos, Fernando de Brito Mota, Roberto Rivelino and Gueorgui K. Gueorguiev, "Electric-Field Control of Spin-Polarization and Semiconductor-to-Metal Transition in Carbon-Atom-Chain Devices," *J. Phys. Chem.,* vol. 121, p. 26125–26132, 2017.

[26] C. H. Wong, R. Lortz, E. A. Buntov, R. E. Kasimova & A. F. Zatsepin, "A theoretical quest for high temperature superconductivity on the example of low-dimensional carbon structures," *Scientific reports,* vol. 7, p. 15815, 2017.

[27] Ovidiu Cretu, Andrés R. Botello-Mendez, Izabela Janowska, Cuong Pham-Huu, Jean-Christophe Charlier, and Florian Banhart, "Electrical Transport Measured in Atomic Carbon Chains," *Nano Lett.,* vol. 13, p. 3487–3493, 2013.

[28] A. La Torre, A. Botello-Mendez, W. Baaziz, J. -C. Charlier & F. Banhart, "Strain-induced metal–semiconductor transition observed in atomic carbon chains," *Nature Communications,* vol. 6, p. 6636, 2015.

[29] Ferdaous Ben Romdhane, Jean-Joseph Adjizian, Jean-Christophe Charlier, "Electrical transport through atomic carbon chains: The role of contacts, Florian Banhart," *Carbon,* vol. 13, p. 3487–3493, 2017.

[30] L. T. Cai, H. Skulason, J. G. Kushmerick, S. K. Pollack, J. Naciri, R. Shashidhar, D. L. Allara, T. E. Mallouk, and T. S. Mayer, "Nanowire-Based Molecular Monolayer Junctions: Synthesis, Assembly, and Electrical Characterization," *J. Phys. Chem.,* vol. 108, p. 2827–2832, 2004.

[31] Fanghao Hu, Chen Zeng, Rong Long, Yupeng Miao, Lu Wei, Qizhi Xu & Wei Min, "Supermultiplexed optical imaging and barcoding with engineered polyynes," *Nature Methods,* vol. 15, p. pages 194–200, 2018.

[32] Prof. Michael M. Haley Stephen C. Brand Joshua J. Pak, "Carbon Networks Based on Dehydrobenzoannulenes: Synthesis of Graphdiyne Substructures," *Angew. Chem.,* vol. 36, pp. 836-838, 1997.

[33] Hisao Ishii, Kiyoshi Sugiyama, Eisuke Ito, Kazuhiko Seki, "Energy Level Alignment and Interfacial Electronic Structures at Organic/Metal and Organic/Organic Interfaces," *Advanced Materials,* vol. 11, p. 605, 1999.

[34] Y. Xu., "Characterization and modeling of static properties and low-frequency noise in organic field-effect transistors (OFETs).," Micro and nanotechnologies/Microelectronics. Université de Grenoble,, Grenoble, 2011.

[35] D. Emin, Polarons, New Mexico: Cambridge university press, 2012.

[36] D. Emin, "Formation and hopping motion of molecular polarons," *Phys. Rev. B,* vol. 14543, p. 61, 2000.

[37] Podzorov V1, Menard E, Rogers JA, Gershenson ME, "Hall effect in the accumulation layers on the surface of organic semiconductors," *Phys Rev Lett.,* 2005.

[38] Tomo Sakanoue, Henning Sirringhaus, "Band-like temperature dependence of mobility in a solution-processed organic semiconductor," *Nature Materials volume 9,* 2010.

[39] Chengliang Wang, Huanli Dong, Lang Jiang and Wenping Hu, "Organic semiconductor crystals," *Chem. Soc. Rev.,* vol. 47, p. 422, 2018.

[40] Yong Xu, Takeo Minari, Kazuhito Tsukagoshi, J. A. Chroboczek, and Gerard Ghibaudo, "Direct evaluation of low-field mobility and access resistance in pentacene field-effect transistors," *Journal of Applied Physics,* vol. 107, p. 114507, 2010.

[41] Kouji SuemoriMisuzu, Taniguchi Toshihide, Kamata, "Effect of Silicon Dioxide Surface on Bias Stress Effect for Organic Field-Effect Transistors," *Japanese Journal of Applied Physics,* vol. 48, p. 170, 2009.

[42] Chengliang Wang, Huanli Dong, Wenping Hu, Yunqi Liu, and Daoben Zhu, "Semiconducting π-Conjugated Systems in Field-Effect Transistors: A Material Odyssey of Organic Electronics," *Chem. Rev.,* vol. 112, p. 2208–2267, 2012.

[43] O. D. Jurchescu, M. Popinciuc, B. J. van Wees, T. T. M. Palstra, "Interface-Controlled, High-Mobility Organic Transistors," *Adv. Mater.,* vol. 19, p. 688–692, 2007.

[44] Motonori Watanabe, Yuan Jay Chang, Shun-Wei Liu, Ting-Han Chao, Kenta Goto, Md. Minarul Islam, Chih-Hsien Yuan, Yu-Tai Tao, Teruo Shinmyozu & Tahsin J. Chow, "The synthesis, crystal structure and charge-transport properties of hexacene," *Nature Chemistry,* vol. 4, p. 574–578, 2012.

[45] John E. Anthony, David L. Eaton, and Sean R. Parkin, "A Road Map to Stable, Soluble, Easily Crystallized Pentacene Derivatives," *Org. Lett.,* vol. 4, p. 15–18, 2002.

[46] V. A. L. Roy, Y.-G. Zhi, Z.-X. Xu, S.-C. Yu, P. W. H. Chan, C.-M. Che, "Functionalized Arylacetylene Oligomers for Organic Thin-FilmTransistors (OTFTs)," *Adv. Mater.,* vol. 17, pp. 1258-1261, 2005.

[47] Oliver Fenwick, Colin Van Dyck, Kathiresan Murugavel, David Cornil Federica Reinders, Sebastien Haar, Marcel Mayor, Jerome Cornil and Paolo Samorı, "Modulating the charge injection in organic field-effect transistors: fluorinated oligophenyl self-assembled monolayers for high work function electrodes," *J. Mater. Chem. C,* vol. 3, p. 2963–3226, 2015.

[48] Y. I. Pensotti, "Fabrication and characterization of films and crystals from powders containing cumulenes," Politecnico di Milano, Milan, 2017.

[49] Jin Yeong Na, Boseok Kang, Dong Hun Sin, Kilwon Cho & Yeong Don Park, "Understanding Solidification of Polythiophene Thin Films during Spin-Coating: Effects of Spin-Coating Time and Processing Additives," *Scientific Reports,* vol. 5, p. 13288, 2015.